UNIVERSITAT ROVIRA I VIRGILI

NUMERICAL MODELING OF HIGH ASPECT RATIO FIBERS IN FLUID FLOWS

MohammadJavad Norouzi

UNIVERSITAT
ROVIRA i VIRGILI

Numerical modeling of high aspect ratio fibers in fluid flows

DOCTORAL THESIS

Author:
MOHAMMADJAVAD NOROUZI

Supervisor:
Prof. JORDI PALLARES
Prof. ANTON VERNET

A thesis submitted in fulfillment of the requirements for the degree of Doctor of Philosophy

in the

Departament d'Enginyeria Mecànica

UNIVERSITAT ROVIRA I VIRGILI

November 2, 2023

Declaration of Authorship

We state that the present study, entitled: **"Numerical modeling of high aspect ratio fibers in fluid flows"** presented by MOHAMMADJAVAD NOROUZI for the award of Doctor of Philosophy, has been carried out under our supervision at the Department of Mechanical Engineering of Universitat Rovira i Virgili.

Tarragona, November 2, 2023

Supervised by:

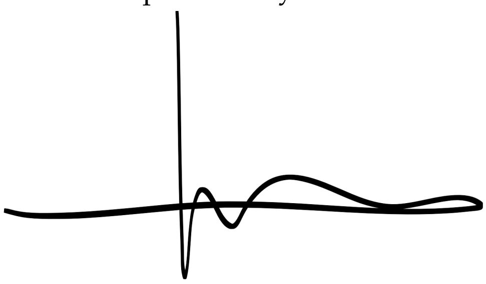

Prof. JORDI PALLARES

Prof. ANTON VERNET

UNIVERSITAT ROVIRA I VIRGILI

Abstract

Departament d'Enginyeria Mecànica

Doctor of Philosophy

Numerical modeling of high aspect ratio fibers in fluid flows

by MOHAMMADJAVAD NOROUZI

Fiber suspensions represent a complex two-phase system that holds significant importance in various industrial applications, including the paper, hygiene, and insulation industries. In these processes, the homogeneity of fiber distribution significantly impacts the final product's quality. Therefore, a thorough understanding of the complex interactions between fiber-fiber and fiber-flow is essential for accurately predicting, controlling, and optimizing fiber behavior and their spatial distribution in these applications.

This thesis employs a particle-level fiber model to numerically analyze fiber suspensions in fluid flows. In this model, each fiber is represented as a chain of fiber segments with a circular cross-section, connected to each other by ball and socket joints. Each fiber segment experiences hydrodynamic forces and torques from the surrounding fluid, as well as from its neighboring segments due to the connectivity constraint, which maintains the fiber's length and integrity. A one-way coupling between the fiber and the fluid is considered, although fibers may interact with each other, leading to the formation of flocs when fiber-fiber contacts occur. Two alternatives of the fiber model are employed: the flexible and rigid models. In the flexible fiber model, elastic bending and twisting torques are taken into account, while in the rigid fiber model, the relative angle between the orientation vectors of adjacent segments remains constant. In the case of flexible fibers, the equations of motion are formulated using Euler's laws of motion for each segment, while for rigid fibers, the equations are formulated for the fiber as a whole. The analysis of fiber behavior is conducted in well-defined flow fields expressed through analytical expressions, as well as in turbulent flow predicted via Large Eddy Simulation (LES) within a Computational Fluid Dynamics solver.

The implemented model is validated against available theoretical and experimental results for the behavior of both rigid and flexible fibers in creeping shear flow. The results of numerical simulations qualitatively replicate experimental observations, capturing various fiber deformation regimes. The fiber model is also used to analyze the dynamics of fibers in viscous cellular flows. The findings emphasize the significant influence of initial conditions ((*e.g.,* orientation, distance from the center of the cell) and mechanical properties of fibers ((*e.g.,* fiber's equilibrium shape, flexibility, and aspect ratio) on their dynamics, transport, and shape evolution.

Simulations are carried out to investigate fiber flocculation in flowing suspensions in a turbulent asymmetric diffuser. In particular, the influence of fiber inertia and reinjection approaches on fiber flocculation is analyzed. The results reveal the crucial role of ballistic deflection, a phenomenon driven by fiber inertia and flow gradients, in amplifying the rate of fiber flocculation within the diffuser region, establishing it as the primary governing mechanism affecting fiber flocculation. Moreover, fibers' initial kinematics and inertia are identified as factors affecting flocculation within the horizontal inflow channel. The findings demonstrate a higher degree of flocculation in the present fully resolved LES simulations than in Reynolds-averaged Navier-Stokes (RANS) modeling, highlighting the significance of different levels of fluid flow resolution in analyzing fiber flocculation.

Keywords: rigid fiber, flexible fiber, particle-level simulation, fiber flocculation, large eddy simulation

Acknowledgements

I would like to express my heartfelt gratitude to the following individuals and groups for their invaluable support, guidance, and encouragement throughout my doctoral journey:

- My esteemed advisors, Prof. Jordi Pallares and Prof. Anton Vernet, for their unwavering dedication, mentorship, and scholarly insights that have shaped this thesis.
- Prof. Håkan Nilsson and Prof. Jelena Andrić, my hosts at the Department of Mechanics and Maritime Sciences at Chalmers University of Technology, for their warm hospitality, collaborative spirit, and the exceptional research environment they provided during my research visit.
- The members of the jury committee for dedicating their time and offering invaluable feedback on my dissertation, which greatly enriched the quality of this work.
- The entire ECoMMFIT research group, with special mention to Prof. Youssef Stiriba, Dr. Alexandre Fabregat, and Dr. Sylvana Varela, for their insightful comments and unwavering encouragement that added depth and rigor to my research.
- Jordi Iglesias, whose significant contributions in the lab, particularly in equipment assistance, were indispensable.
- Mr. Lluís Vàzquez and Ms. Núria Juanpere for their indispensable technical and logistical support that facilitated my research endeavors.
- My dear fellow lab mates and friends, including Mojtaba GorakiFard, Mohsen GorakiFard, and Koorosh Kazemi, for their camaraderie, shared experiences, and countless discussions that enriched my academic journey.
- The European Union's Horizon 2020 research and innovation program, Marie Skłodowska-Curie grant agreement No. 713679, the Universitat Rovira i Virgili (URV), EC Research Innovation Action under the H2020 Programme (Project

HPC-EUROPA3, INFRAIA-2016-1-730897), the Department of Numerical Methods & Libraries of the High-Performance Computing Center Stuttgart (HLRS), and HLRS High-Performance Computing Center Stuttgart for their essential financial support and technical resources. I also acknowledge the Spanish Ministry of Economy, Industry, and Competitiveness Research National Agency (projects DPI2016-75791-C2-1-P and PID2020-113303GB-C21), FEDER funds, and Generalitat de Catalunya - AGAUR (project 2017 SGR 01234) for their contributions, which were indispensable to the successful completion of this research.

- Last but not least, I want to thank my mother, my wife, my brothers and sisters, whose inspiration continues to guide me, and my mother and my wife, whose enduring patience and unwavering support have been the pillars of strength throughout my scholarly pursuits.

Thank you all for being an integral part of my academic and personal life, and for contributing to the realization of this thesis.

Contents

List of Figures

List of Tables

I dedicate this thesis to the cherished memory of my father, and to my mother, and my wife.

Chapter 1

Introduction

The study of anisotropic particulate suspensions holds great interest for scientists and engineers due to its extensive applications across various industrial and environmental contexts. These contexts range from composite, pulp and papermaking (*1*–*3*) to modeling plankton dynamics in water (*4*), sedimentation (*5*, *6*), aerosols (*7*), and ice crystals within clouds (*5*). The work presented here primarily focuses on suspensions that contain non-Brownian fibers, similar to those found in wood pulp suspensions and fiber-reinforced composites. In these processes, the orientation and spatial distribution of fibers, whose development is intricately linked to fiber-flow interactions and fiber-fiber contacts, significantly affect the properties of the final products. Therefore, the analysis and prediction of fiber motion are of paramount importance in designing and optimizing these processes, ultimately enhancing product quality. Within the scope of this thesis, a particle-level simulation technique is employed to systematically investigate fiber dynamics, fiber shape evolution, and fiber flocculation in flowing fiber suspensions, depending on fiber characteristics and fluid flow properties.

1.1 Literature review

Fiber suspensions form a complex two-phase system, and they have been the subject of numerous theoretical, experimental, and numerical studies. The following sections provide a brief overview of the relevant studies.

1.1.1 Theoretical studies of fiber flows

There is a significant body of knowledge concerning the motion of isolated rigid fibers in flows characterized by low Reynolds numbers. Jeffery (*8*) made a seminal contribution by solving for the motion of force- and torque-free spheroids in simple shear flow. His work demonstrated that spheroids translate with the velocity of the surrounding flow at their centers while also undergoing periodic rotation, resulting in their ends tracing out an 'orbit' (*8*). In the context of cylindrical particles, Burgers (*9*) derived the hydrodynamic force and torque constants acting on such particles and postulated that the disturbance induced along the ellipsoid of revolution could be represented as a line force of magnitude acting along the particle's axis of symmetry. Bretherton (*10*) theoretically established that any axisymmetric body placed in a linear flow field would exhibit motion analogous to Jeffery's predictions. This motion entails the body undergoing a closed orbit without drifting across streamlines. Cox (*11*) employed the Matched Asymptotic Expansions (MAE) method to derive the transverse and axial force per unit length acting on high aspect ratio cylindrical particles, a concept known as slender body theory. Building upon Cox's work, Batchelor *et al.* (*12*) extended the formulation to account for slender bodies with non-circular cross-sections. Further advancements in slender body theory were made by Keller and Rubinow (*13*), and Johnson (*14*) who introduced a non-local drag formulation within this theoretical framework (*15*). It is shown that the straining motion within the flow field can generate axial forces of sufficient magnitude to induce buckling of the fiber during rotation. Burgers (*9*) determined the critical stress required to cause this phenomenon, expressed as $(\dot{\gamma}\eta_0)_{\text{crit}} \simeq E_b(\ln 2r_f - 1.75)/2{r_f}^4$, where $r_f = L/D$ is the fiber aspect ratio (*i.e*, the ratio of fiber length to the fiber diameter), and the bending modulus of the rod is defined as $E_b = 2E_Y$, with E_Y representing Young's modulus of the fiber.

Fiber suspensions can be classified into three distinct regimes: dilute, semi-dilute, and concentrated, based on the concentration of suspended fibers within the suspension. A suspension is considered dilute when, on average, fewer than one fiber is found within a spherical volume of diameter equal to the fiber length, as expressed by $nL^3 \ll 1$, where n denotes the number of fibers per unit volume, and L is the fiber length (16, 17). In such a dilute suspension, when subjected to a low Reynolds number simple shear flow, the behavior of the fibers adheres to Jeffery's predictions. Consequently, they rotate about their center of mass, tracing out Jeffery's orbits (18). For these dilute suspensions, Batchelor (18) suggested an expression for the stress originating from elongated rigid particles with a known orientation distribution.

Moving into the semi-dilute regime, characterized by conditions such as $nL^3 > 1$ and $nL^2D \ll 1$, the motion of fibers is significantly influenced by interactions with other fibers (16). This interaction causes deviations from Jeffery's orbits (8). When the concentration exceeds the threshold of $nL^2D > 1$, the suspension enters the concentrated regime. In this regime, it is assumed that every fiber interacts with other fibers, ultimately forming a network (19). Rahnama *et al.* (20) conducted research in this context and derived the steady-state fiber orientation. They employed a framework of perturbation analysis in conjunction with the theory of Leal and Hinch (21) to account for weak rotary Brownian motion. The results obtained for orbit distribution and fiber orientation distribution were found to be in reasonable agreement with the experimental findings of Stover *et al.* (22), particularly within the semi-dilute regime. Theoretical studies are, therefore, limited to scenarios involving straight fibers and relatively low fiber concentrations.

1.1.2 Experimental studies of fiber flows

Numerous experimental studies have been dedicated to investigating the behavior of both individual fibers and fiber suspensions. Anczurowski and Mason (23) conducted experiments that confirmed Jeffery's predictions concerning the motion of prolate spheroids in shear flow. Forgacs and Mason (24) conducted experiments utilizing a twin-cylinder Couette apparatus to generate creeping shear flow, allowing them to examine the behavior of threadlike particles. Their research identified five distinct regimes of motion: rigid orbits, springy orbits, snakelike orbits, coiled orbits without entanglement, and coiled orbits with entanglement. They made the noteworthy observation that rigid fibers exhibit the same orbital patterns as rigid cylinders. In contrast, the orbital periods of flexible fibers were found to be significantly shorter compared to those of straight, rigid fibers. Their findings underscored the influence of various factors related to the suspension system, including fiber geometry, fiber stiffness, and flow properties, on the shapes and motion behaviors observed in the experiments. Bibbo (25, 26) conducted a comprehensive study of the rheological behavior of non-colloidal rigid fiber suspensions. The investigation explored the influence of fiber concentration on the apparent viscosity within both dilute and semi-dilute regimes. The obtained results were then compared to Batchelor's theory (18), revealing good agreement in the dilute regime.

Stover *et al.* (22) conducted experimental research on the microstructural behavior of semi-dilute rigid fiber suspensions using optical methods in which they could perform direct observation of tracer fibers within a Couette rheometer. They analyzed the orientation statistics of the fibers from the microstructure images and used this data to characterize the orbit distribution of the fibers. By combining the orientation distribution with Batchelor's theory (12), they deduced the rheological properties of the fiber suspension. The measured orbit constants aligned well with the experimental findings of Anczurowski *et al.* (23) within the dilute regime. Furthermore, the rheological properties of the suspension reasonably matched the experimental results of Bibbo (25) and the theory proposed by Shaqfeh and Fredrickson (27). Notably, hydrodynamic interactions among fibers in the semi-dilute regime played a crucial role in determining the steady-state orientation of the suspension. Pettersson *et al.* (28) conducted an extensive investigation of the near-wall behavior in the pipe flow of fiber suspensions, showing that the width of the concentration profile increased as the concentration decreased, and the dilution region's thickness was larger for softwood fibers. Melander and Rasmuson (29) developed a particle image velocimetry (PIV) method to simultaneously measure the concentrations and velocities of fibers suspended in the air. This method proved feasible for studying air-fiber flows at low concentrations.

In experiments involving fiber-fluid interactions, a key challenge lies in achieving precise control over fibers in terms of their shapes, dimensions, and mechanical properties, as well as control of the flow geometry (30). Additionally, the phenomena related to fiber dynamics occur on scales with the length of an individual fiber. Experimental measurements of factors such as fiber shapes and deformations of flexible fibers, as well as the determination of rheological properties of suspensions (31, 32), can be inherently difficult to obtain. As a result, researchers have turned to various numerical techniques to effectively investigate and understand fiber dynamics.

1.1.3 Numerical modeling of fiber flows

Two primary numerical methodologies have been devised for modeling fiber suspensions: the Eulerian-Eulerian approach and the Lagrangian-Eulerian approach. In the Eulerian-Eulerian approach, both the particle phase and the fluid phase are considered as continuous medium (33). Several researchers have employed this technique as a valuable computational tool for investigating fiber dynamics on large scales. Ljus and Almstedt (34) used this approach to conduct two- and three-dimensional simulations of fiber suspensions within a channel, both with and without incorporating a turbulence model for the gas phase. The results for pressure and velocity showed good agreement with experimental findings within a comparable channel. When modeling various phenomena associated with fiber suspension behavior, it is often necessary to combine an Eulerian-Eulerian model with other modeling approaches, such as statistical methods (35). In this framework, the probability distribution of fiber positions and orientations is predicted using the convection-diffusion equation. The mean flow transports the fiber positions and orientations, while the fluctuating component of the flow disperses the fibers. Olson *et al.* (36) used this technique to simulate the turbulent fiber suspension flowing through a planar constriction. They demonstrated that fiber distributions correlated well with experimental measurements, and fiber orientation distribution depends on the dispersion coefficient and the contraction ratio. Krochak *et al.* (37) simulated the low-Reynolds flow of semi-dilute rigid fiber suspensions in a tapered channel, aiming to study fiber reorientation and the effect of the two-way coupling between fibers and flow. They found that the presence of fibers substantially changes the velocity profiles, regardless of the initial fiber distribution. They also observed that the particle phase redirects the flow away from the channel walls towards the central region of the channel, resulting in linearized and closer streamlines across the channel length. However, in most Eulerian-Eulerian models, the fibers are assumed to be rigid with uniform characteristics, and fiber-fiber interactions are neglected (32, 35, 37). These assumptions do not always align with the realities of industrial processes, which often involve fibers with different characteristics and concentrated fiber suspensions.

In the Lagrangian-Eulerian approach, each particle is tracked individually through the Lagrangian particle tracking (LPT) method. This approach facilitates detailed and highly accurate studies of particle-flow interactions. For instance, in direct numerical simulations (DNS), the particle geometries are resolved at a high level of detail (32). Tornberg and Shelley (38) developed a non-local formulation of the Slender Body Theory (SBT) (13, 14) coupled with the Euler-Bernoulli beam theory. This approach yielded integral expressions for the center-line velocity of high aspect ratio filaments, considering the hydrodynamic interactions between multiple fibers and the impact of fibers on the background fluid. Li *et al.* (39) employed a variation of the numerical method initially proposed by Tornberg and Shelley (38) to investigate the sedimentation of flexible filaments. A comprehensive review of SBT regarding its application to modeling fibers has been provided by Lindner and Shelley (40). Svenning *et al.* (41) employed the immersed boundary method (IBM) to investigate the flow of fiber suspensions in the papermaking process. Wu and Aidun (42) used the lattice-Boltzmann method (LBM) for the direct numerical simulation of flexible fibers in a Newtonian fluid. Aidun and colleagues (42–44) used an IBM within the LBM framework, known as the 'external boundary forcing' method, to study the effect of fiber stiffness and rotational diffusion of semi-dilute fiber suspensions. While these approaches fully resolve the flow field around a fiber and provide accurate predictions of fiber dynamics, they come at a high computational cost. In this regard, micro-hydrodynamics approaches (45, 46) have been developed to reduce the computational demands in investigating fiber suspensions.

1.1.4 Particle-Level simulation technique

A variety of particle-level simulation techniques that utilize the microhydrodynamics approach have been developed for the study of fiber suspension flows. In this framework, each fiber is represented by an array of spheres, prolate spheroids, or rods that are interconnected. These models account for bending and twisting deformations by allowing movement of the rigid parts relative to each other (32). Such models are adept at capturing realistic features of fibers, including different fiber equilibrium shapes and fiber stiffness (*47*). Fibers within these models can interact with each other through both short-range forces ((*e.g.,* repulsion, lubrication, friction) and long-range hydrodynamic interactions, although not all interactions may be included in a specific case (*30*). The equations of motion are individually solved for each particle, enabling the evolution of particle positions and orientations over time. Consequently, these techniques provide detailed information about the evolving structures of suspensions in both time and space. Particle-level methods are regularly employed to investigate a wide range of phenomena within fiber suspensions, such as fiber-flow and fiber-fiber interactions, the formation of fiber flocs, and the collective influence of these phenomena on the rheological properties of these suspensions (*32*).

In 1992, Yamamoto and Matsuoka (*48*) developed a bead-chain model to simulate the motion of a flexible fiber within a simple shear flow. In their mechanical model, they represented fibers as a series of spheres aligned and bonded to each other. The model was developed under specific conditions, including an infinitely dilute system, no hydrodynamic interactions, and low Reynolds fluid flow. To validate their model, they conducted simulations of the motion of a flexible fiber by solving translational and rotational equations for each individual sphere. The flexibility of the fiber was adjusted by varying the bending constant, with a higher bending constant corresponding to a more rigid fiber. To verify the model, they calculated the motion period for a rigid fiber, which aligned with the prediction derived from Jeffery's equation. For flexible fibers, they observed a significant decrease in the motion period as the bending deformation of the fiber became more pronounced. The motion orbit deviated from the one described by Jeffery's equation, similar to experimental results reported by Forgacs and Mason (*24*, *49*). While the simulation results from this model provided precise information about the movement of every point on the fiber, substantial computational effort is required as the fiber length increases, particularly in cases relevant to industrial applications (*48*). The lubrication approximation, a method used to account for fiber-fiber interactions, was also incorporated into a model proposed by Yamane *et al.* (*19*). This model was designed to simulate the behavior of semi-dilute suspensions comprising non-Brownian, rod-like particles under simple shear flow. While the focus of this model was not the motion of flexible fibers, it offered valuable insights into the potential effectiveness of considering short-range fiber interactions using the lubrication approximation. Yamane *et al.* observed that the impact of hydrodynamic interactions on both viscosity and the Folgar-Tucker constant is relatively small, which contradicts experimental observations (19). The authors attributed this discrepancy to the non-Brownian motion of the rigid rods featured in their model.

Ross and Klingenberg (50) developed a simulation model for the dynamics of flexible fiber suspensions, known as the needle-chain model. This model represents flexible fibers as a series of rigid spheroid bodies connected through ball and socket joints. It is designed to simulate the motion of both rigid and flexible fibers. The model accurately predicted the motion period of a single rigid fiber in a shear flow, consistent with Jeffery's equation. Furthermore, the motion of flexible fibers in this model closely resembled experimental observations made by Forgacs and Mason (24). One notable advantage of this model is that it eliminates the need for iterative constraints to maintain fiber connectivity. It can efficiently model flexible fibers with large aspect ratios using relatively few spheroids, thereby reducing computational time. However, it's important to note that the model's accuracy diminishes when dealing with longer needle lengths.

The model was also used to simulate the motion of fiber suspensions by considering only repulsive interactions and neglecting hydrodynamic interactions and particle inertia. These repulsive interactions encompass both intra- and inter-fiber interactions, including colloidal forces, short-range repulsion, and friction between fibers. The model was employed to investigate the transient behavior of the relative viscosity of the suspension under simple shear flow, revealing that fiber flexibility increases the hydrodynamic contribution to viscosity (51). Skjetnet, Ross, and Klingenberg published a follow-up article to provide additional insights into the needle chain model. Their simulation results for flexible fibers align with previous experimental observations, indicating that the direction and rate of deviation from the Jeffery orbit depend on factors such as fiber stiffness, initial fiber orientation, and the characteristics of the flow field. Building on the needle chain model, Schmid *et al.* (45) developed a particle-level model to simulate the motion of flexible fibers. In this model, flexible fibers are represented as chains of elongated bodies connected by hinges. It is primarily used to simulate flocculation in flowing fiber suspensions, considering fiber flexibility, irregular fiber equilibrium shapes, and frictional interactions between fibers. The simulations demonstrated that flocculation can occur due to inter-fiber friction and repulsive interactions even in the absence of attractive forces between fibers. Furthermore, the results showed that various fiber features, including stiffness and fiber shape, along with interaction forces, strongly influence flocculation behavior and the properties of flocs. Switzer and Klingenberg (*47*) further investigated the relationships between fiber properties, interactions, and the resulting rheological properties of suspensions under simple shear flow. Their model is based on the approach introduced by Schmid e*et al.*, where flexible suspensions are represented as chains of neutrally buoyant, linked rigid cylinders connected by ball and socket joints immersed in a Newtonian liquid. Their model did not consider particle inertia, hydrodynamic interactions, or the two-way coupling between the fibers and the flow. The fibers interact with each other through short-range repulsive forces and friction forces. The simulation results concur with those presented by Schmid *et al.*, demonstrating that fiber flexibility leads to shear-thinning behavior due to the competition between hydrodynamic forces and fiber elasticity (*51*). Lindström and Uesaka (*46*) made improvements to the numerical stability of the model proposed by Schmid *et al.* (*45*). They also implemented a two-way coupling scheme and introduced a hydrodynamic force model suitable for the inertial regime. Additionally, they derived an approximation for non-creeping interactions between fiber segments and the surrounding fluid when dealing with larger segment Reynolds numbers. This enhanced model was employed to study semi-dilute non-Brownian fiber suspensions, and it successfully replicated various regimes of motion for threadlike particles, spanning from rigid fiber motion to complex orbiting behavior, including coiling both with and without self-entanglement (*46*). Lindström and Uesaka (*52*) used this model to predict the rheological properties of fiber suspensions at various volume concentrations, taking into account both hydrodynamic and mechanical fiber interactions. They also investigated the impact of fiber aspect ratio, fiber concentration, and inter-particle friction on the stress tensor of the suspension and on fiber flocculation.

The same model developed by Lindström and Uesaka (*46*) was also employed by Andrić *et al.* (53–55) to study the behavior of dilute suspensions and the motion of fibers in inertial flows. Andrić *et al.* (53) investigated the motion of rod-like fibers in the decelerating flow of a wedge-shaped channel using analytical and numerical methods. They considered both infinite and finite hydrodynamic resistance to transverse flow and identified the phenomenon of ballistic deflection, where fiber trajectories significantly deviate from the streamlines of the carrying flow. They argued that ballistic deflection increases the relative motion of fibers, potentially affecting the collision rate and, consequently, the rate of aggregation. Later, Andrić *et al.* (55) examined the flocculation of suspensions of rigid fibers in the decelerating flow field of a diffuser. They modeled the fibers using a particle-level fiber model and described the fluid flow using the two-dimensional steady-state Navier-Stokes equation with the standard $k - \omega$ turbulence model to account for the effects of turbulence. They also incorporated a stochastic model to consider the dispersion of fibers due to turbulence. Their main finding was that the anisotropic hydrodynamic resistance of fibers and the flow velocity gradients induce ballistic deflection of fibers, leading to fiber flocculation in the diffuser. Additionally, they observed that the kinematics of reinjected fibers strongly affect the flocculation in the horizontal inflow channel and at the entrance of the diffuser.

1.2 Thesis objectives and structural outline

This work primarily investigates suspensions containing non-Brownian fibers, which are commonly found in processes like paper manufacturing and wood pulp suspensions. The present work is primarily concerned with the study of suspensions containing non-Brownian fibers, which are commonly found in processes like paper manufacturing and wood pulp suspensions. The main goal of this research is to get a deeper understanding of how fluid flow and microscopic fiber features, such as flexibility, irregular shapes, and aspect ratio, impact the behavior of both flexible and rigid fibers in flowing fluids. To achieve this, a particle-level simulation technique, which builds on previous work by Schmid *et al.* (45), Switzer III and Klingenberg (47), and further improved by Lindstrom and Uesaka (46), is used to systematically study fiber behavior in different flow conditions and geometries.

The main objectives of this thesis may be summarized as follows: (i) the validation of the adapted particle-level model employed in this study, conducted through theoretical and experimental assessments of isolated fiber motion within a simple shear flow, (ii) the application of the fiber model to study the dynamics of flexible and rigid fibers in different flow scenarios, with a particular emphasis on the examination of fiber transport and shape evolution based on fiber properties, and (iii) the examination of fiber flocculation phenomena in flowing suspensions, with a specific focus on understanding the mechanisms governing the flocculation of fibers within turbulent suspension flows.

The remaining parts of this thesis are structured into 5 chapters. Chapter 2 provides the theoretical background of this research, presenting the geometry of the fiber model and the governing equations for both rigid and flexible fibers as well as the fluid flow. Chapters 3 and 4 present the outcomes of simulations of the fiber suspensions. Each of these two chapters is self-contained, encompassing a discussion of the background material, a description of the models and simulation techniques, and a detailed analysis of simulation results.

In Chapter 3, we begin with the presentation of simulation results exploring how individual fibers move in a simple viscous shear flow of an incompressible Newtonian fluid. Validation of the fiber model is conducted by comparing simulation results for both rigid and flexible fibers with established theoretical findings of Jeffery *et al.* (*8*) and experimental data by Foragacs and Mason *et al.* (*24*). Subsequently, the motion of isolated fibers in viscous cellular flow is explored to study fiber transport for different initial conditions (position and orientation) and various degrees of fiber stiffness. Furthermore, the dynamics and deformation of long flexible fibers are examined, based on fiber flexibility, aspect ratio, and equilibrium shape. Additionally, an analysis of fiber trajectories is conducted to acquire a comprehensive understanding of the effects of fiber flexibility, initial positions, and orientations on fiber transport.

Chapter 4 offers a detailed analysis of flowing fiber suspensions in an axisymmetric diffuser using Large Eddy Simulation (LES). It includes a comprehensive study of the evolution of fiber floc mass fraction, fiber trajectories, fiber slip velocities, and fiber alignment in the fluid flow. We particularly investigate a phenomenon called “flow-induced ballistic flocculation”, which originates from the ballistic deflection of fibers. We analyze this phenomenon for fibers with different inertial properties and various approaches of fiber reinjection into the flow. Additionally, we compare the outcomes of fully resolved LES simulations with those from Reynolds-averaged Navier-Stokes (RANS) simulations using a particle dispersion model, as previously studied by Andrić *et al.* (55).

In Chapter **??**, we summarize the research findings and provide suggestions for future research works.

1.3 Related Contributions

Throughout the course of this research, the following significant contributions were made:

- **Journal articles**
  - MohammadJavad Norouzi, Jelena Andric, Anton Vernet, and Jordi Pallares. "Shape evolution of long flexible fibers in viscous flows." Acta Mechanica 233, no. 5 (2022): 2077-2091.
  - Norouzi, MohammadJavad, Jelena Andric, Anton Vernet, Jordi Pallares, and Hakan Nilsson. "Large eddy simulation of fiber flocculation in a diffuser", Submitted.
- **Conference contributions**
  - MohammadJavad Norouzi, Anton Vernet, and Jordi Pallares. (2021) “Shape development of long flexible fibers in viscous cellular flow: effects of fiber properties”, 18th Multiphase Flow Conference, Dresden, Germany.
  - MohammadJavad Norouzi, Anton Vernet, and Jordi Pallares. (2019) “Deformation, orientation and spatial distribution of long flexible fibers in viscous flows”, 17th Conference and Short Course on Multiphase Flows, Dresden, Germany.
  - MohammadJavad Norouzi, Anton Vernet, and Jordi Pallares. (2019) “Long flexible fibers in viscous shear flows”, CISM-AIMETA Advanced School on anisotropic particles in viscous and turbulent flows, Udine, Italy.

Chapter 2

Simulation method

2.1 Fiber model

In this thesis, a particle-level simulation technique is employed to model fiber suspensions. The fiber is conceptualized as a chain of rigid cylindrical segments that are lined up and connected to each other through ball and socket joints while immersed in a Newtonian liquid. The model accommodates bending and twisting deformations by allowing for movement of the rigid cylinders relative to each other. The model demonstrates proficiency in capturing realistic characteristics of fibers, including non-straight equilibrium fiber shapes and variations in fiber stiffness. This fiber model provides two alternatives: the flexible and rigid fiber model. In the flexible fiber model, the segments may rotate and twist around the joints, thus accurately the bending and twisting deformations of the fiber. On the other hand, in the rigid fiber model, the relative orientation between adjacent segments remains fixed, effectively constituting a rigid body. In the forthcoming sections, the description of the fiber geometry and the governing equations for both the flexible and rigid fiber models are presented.

2.1.1 Fiber geometry

Each fiber is modeled as a series of N_{seg} linked rigid cylinders connected by ball and socket joints with hemispherical end-caps. Figure 2.1 shows the fiber geometry, where the position of the center of mass of each segment i is represented by the vector $\vec{r}_i$, and the unit orientation vector is $\hat{p}_i$. Fiber joints are numbered starting with a virtual joint at the free end of the first segment. Each segment has a diameter

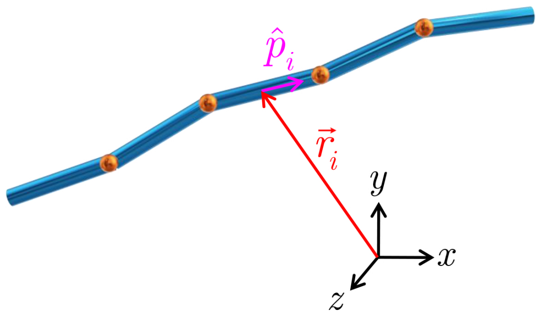

FIGURE 2.1: Illustration of a general non-straight fiber

D and length l, representing the fibers with an aspect ratio represented as $r_f = L/D = N_{seg} l/D$.

2.1.2 Equations of motion for a flexible fiber

The motion of fibers is governed by force and torque balances on each fiber segment i in the chain, and the constraint that the fiber contour length remains constant.

The forces that act on a fiber segment i with mass m_i include hydrodynamic forces ($\vec{F}_i^h$), the sum of body force ($\vec{F}_i^b$), and the connectivity forces that act among the adjacent fiber segments to ensure fiber integrity and keep the fiber at a constant length ($\vec{X}_i$),

$$m_i \ddot{\vec{r}}_i = \vec{F}_i^h + \vec{F}_i^b + \vec{X}_{i+1} - \vec{X}_i, \tag{2.1}$$

The torque balance on fiber segment i includes similar contributions with the addition of a restoring torque at each joint ($\vec{Y}_i$),

$$\frac{\partial}{\partial t}\left(\bar{\bar{I}}_i \cdot \vec{\omega}\right) = \vec{T}_i^h + \vec{Y}_{i+1} - \vec{Y}_i + \left(\frac{l}{2}\vec{p}_i\right) \times \left(\vec{X}_{i+1}\right) + \left(\frac{-l}{2}\vec{p}_i\right) \times \left(-\vec{X}_i\right) \tag{2.2}$$

where $\bar{\bar{I}}_i$ is the tensor of inertia of segment i with respect to the global coordinate system, $\vec{\omega}_i$ is the angular velocity, $\vec{T}_i^h$ is the hydrodynamic torque, and $\vec{Y}_i$ is the sum of the bending and twisting torques exerted on segment $i-1$ by segment i. In Equations (2.1) and (2.2), for the end segments, $\vec{X}_1 = \vec{X}_{N_{seg}+1} = \vec{0}$, as well as $\vec{Y}_1 = \vec{Y}_{N_{seg}+1} = \vec{0}$.

The constraint that keeps a fiber at a constant length requires that the endpoints of adjacent fiber segments coincide, (*i.e.*,

$$\vec{r}_i + \frac{l}{2}\vec{p}_i - \left(\vec{r}_{i+1} - \frac{l}{2}\vec{p}_{i+1}\right) = \vec{0} \tag{2.3}$$

Taking the time derivative leads to the following constraint:

$$\dot{\vec{r}}_i - \dot{\vec{r}}_{i+1} = \frac{l}{2}\vec{\omega}_i \times \vec{p}_i + \frac{l}{2}\vec{\omega}_{i+1} \times (-\vec{p}_{i+1}) \tag{2.4}$$

Combining Equations (2.1) and (2.2) into Equation (2.4) forms a system of equations that can be solved for the unknown segment velocities and angular velocities. Once the velocities have been calculated, the new positions and orientations for all segments can be determined. A detailed discussion of hydrodynamic forces and torques exerted by the fluid on the fiber segments and the numerical algorithms to solve these equations is provided in Chapter 3 and references (*45*–*47*, *56*), and in detail in Appendix A.1

2.1.3 Equations of motion for a rigid fiber

In the case of a rigid fiber, the linear and angular equations of motion are formulated for the fiber center of mass $\vec{r}_G$, while the hydrodynamic contributions are summed up over the fiber segments. Considering all segments have identical characteristics ((*i.e.*, mass m_i, length l_i, diameter d_i and unit vector $\vec{p}_i$), the center of mass of the fiber is $\vec{r}_G = \frac{1}{N_{seg}} \sum_{i=1}^{N_{seg}} \vec{r}_i$. Moreover, since the fiber is rigid, each segment i has the same angular velocity as the center of mass of the fiber ($\vec{\omega}_i = \vec{\omega}_G$). The linear and angular equations of motion are formulated as (*56*)

$$m\ddot{\vec{r}}_G = \sum_{i=1}^{N} \vec{F}_i^h \tag{2.5}$$

$$\frac{\partial}{\partial t}\left(\bar{\bar{I}}_G \cdot \vec{\omega}\right) = \bar{\bar{I}}_G \cdot \dot{\vec{\omega}} + \vec{\omega} \times \left(\bar{\bar{I}}_G \cdot \vec{\omega}\right) = \sum_{i=1}^{N_{seg}} \vec{T}_i^h + \sum_{i=1}^{N_{seg}} (\vec{r}_i - \vec{r}_G) \times \vec{F}_i^h \tag{2.6}$$

Here $m = \sum_{i=1}^{N_{seg}} m_i$ is the fiber mass, $\bar{\bar{I}}_G$ is the inertia tensor of the fiber with respect to its center of mass, $\vec{F}_i^h$ and $\vec{T}_i^h$ are the hydrodynamic drag force and torque exerted by the fluid on segment i. Equations (2.5) and (2.6) together form the system of equations that can be solved for the linear and angular velocities of the fiber. Once the linear and angular velocities of the fiber segments are calculated, the positions and orientations of the fiber are updated accordingly. A detailed discussion of hydrodynamic forces and torques imposed by the fluid on the fiber segments as well as the numerical algorithms to solve the equations is provided in Chapter 4, reference (53), and in detail in Appendix A.2.

2.2 Flow field

The representation of the flow field depends on the nature of the study being conducted. In Chapter 3, a simple shear flow is used for the purpose of validating the implemented fiber model. An analytical expression to describe this flow field is given by:

$$\vec{v} = \left(\dot{\gamma}y, 0, 0\right), \tag{2.7}$$

where $\vec{v}$ represents the fluid velocity, and $\dot{\gamma}$ is the shear rate.

In Chapter 3, the behavior of flexible fibers flowing in a lattice of counter-rotating vortices is also studied. The two-dimensional steady velocity field of the cellular flows is described by (57):

$$v_x = U_0 \left(\sin(\tilde{x}) cos\left(\tilde{y}\right)\right) \tag{2.8}$$

$$v_y = U_0 \left(-cos\left(\tilde{x}\right) \sin\left(\tilde{y}\right)\right) \tag{2.9}$$

Where $\tilde{x}$ (resp. $\tilde{y}$) is the dimensionless coordinate $\pi x/2W$ (resp. $\pi y/2W$)), in which $2W$ is the cell size, and U_0 is considered to be 1.

In Chapter 4, the dynamics of fibers are analyzed in turbulent flow in an axisymmetric diffuser. The flow is modeled using highly resolved Large Eddy Simulation (LES) as predicted by the OpenFOAM CFD solver, which provides an accurate representation of the flow field. This involves the utilization of the three-dimensional, incompressible Navier–Stokes equations to describe the motion of the fluid.

The selected simulation methods are capable of accurately capturing the system's physics while maintaining reasonable computational costs.

Chapter 3

Shape Evolution of Long Flexible Fibers in Viscous Flows

3.1 Introduction

The motion of long flexible fibers in fluid flows is central to many industrial applications, including pulp and paper making, textile, insulation and food industries, as well as microfluidic engineering and biotechnologies (*54*, *58*–*60*). In addition to these applications, suspensions of long filaments are also a matter of interest in nature and some biological systems, such as in cell division (*61*) and swimming of microorganisms (*62*). The flow-induced deformation of fibers is essential for fiber transport (*63*), affecting the isotropy and spatial dispersion of fibers. These impacts on the microstructure of the fibers suspension strongly affect the macroscopic properties (*e.g.*, mechanical, thermal, electrical) of the final product (*53*, *64*, *65*). Hence, unveiling the fundamental mechanisms and governing parameters behind these phenomena remains crucial to improving the design and optimization of products and processes.

There have been numerous experimental, theoretical and numerical research to investigate the behavior of rigid spherical or non-spherical particles in various flow conditions. When objects have multiple degrees of freedom, which is the case for flexible fibers, the problem becomes increasingly challenging due to the formation of complex fiber structures created through flow-induced bending, buckling, twisting, and flocculation. Early experiments by Forgacs and Mason (*24*, *49*) with elastic fibers in simple shear flow demonstrated different shapes and motion behaviors depending on the characteristics of the suspension system, including fiber geometry, fiber stiffness, and flow properties. They identified various regimes of fiber motion, including the rigid motion in which the fiber follows Jeffery orbits (*8*), periodic orbits with springy and snake-like deformations, complex coiled orbits, and coiled motion with entanglement. With technological advances in microfluidic technology, the periodic shape deformations were studied experimentally for DNA strands and actin filaments (*66*, *67*), and complex coiling and entanglement of long actin fibers in shear flows (*68*). Wandersman *et al.* (*57*) studied the deformation and transport of flexible fibers in a viscous cellular flow, created by a planar array of electromagnetically driven counter-rotating vortices. They observed both fiber trapping in vortices, and fiber transport and buckling through hyperbolic stagnation points for the sufficiently high fluid strain-rate. They also reported on the effect of fiber deformation on its translational motion, and identified the buckling threshold in a reasonable agreement with the predictions of linear analysis in a purely hyperbolic flow (*57*).

The Slender Body Theory (SBT) (*38*), Immersed Boundary Methods (IBM) (*69*, *70*), and bead and rod models (*48*, *54*, *55*) have been the three main methods used to study numerically the dynamic of suspended flexible fibers in a fluid flow (*71*). Reviews (*30*, *35*, *40*, *72*) have presented the basics and algorithmic advances of these computational modeling approaches. Much progress has been made in employing SBT to describe the orbits and buckling of fibers in fluid flows (*38*, *63*, *68*, *73*). In particular, Quennouz *et al.* (*63*) studied the dynamics, transport, and buckling of elastic fibers in a two-dimensional cellular flow experimentally and numerically using SBT. They investigated the probability of fiber buckling by varying the parameter so-called "elasto-viscous number", which represents the relative intensity of viscous forces to fiber elastic forces. The typical shape evolution of fibers in shear flow was studied by Nguyen & Fauci (*74*), Słowicka *et al.* (*75*) and LaGrone *et al.* (*76*). They observed that elastic fiber often tends to the flow–gradient plane, and its shape development in the shear flow depends on the fiber slenderness and the elasto-viscous number. The fiber rotates rigid and nearly-rigid in the shear for small elasto-viscous number; it buckles once the elasto-viscous number reaches the threshold value; and a transition to a "snaking behavior" occurs for larger elasto-viscous numbers (*76*). By modeling a fiber as a chain of spherical particles, Kuei *et al.* (*77*) studied the complex coiling and formation of knots in shear flow. Kondora and Asendrych (*78*) employed a one-way coupled particle-level fiber method, where the fibers were modeled as a chain of spheres connected by ball and socket joints, to obtain the probability distribution function of fiber orientation in a converging channel of a papermachine headbox. The influence of fiber stiffness and the compressional flow field on the shape of deformed fiber has been studied by Chakrabarti *et al.* (79). In particular, they reported that flexible filament could buckle into a helical shape in a purely compressional flow when end moments and compressive forces are applied, standing out from classical helical buckling where filament may obtain a chiral helicoidal morphology in the absence of any intrinsic twist or external moments.

Understanding how non-spherical structures interact with a turbulent flow is quite complicated. Beyond the complexity of turbulence of flows with spherical particles, the forces and torques that depend on the particle shape and orientation should also be considered (80, 81). The majority of the studies dealing with non-spherical particles in turbulence focus on rigid spheroids (59, 82, 83), reporting the tendency of the particles to align with the direction of the strongest Lagrangian fluid stretching (82, 84). It has been shown that the particle shape and size affect the inertia-driven phenomena such as preferential concentration and near-wall accumulation (81, 83, 85). Flexibility is another parameter that can affect the behavior of high aspect ratio particles suspended in a turbulent flow since the particle may experience severe flow-induced velocity gradients over its length (86).

Few studies are available on the suspension of flexible particles in turbulent flows due to the complexities addressed earlier. Brouzet *et al.* (87) and Gay *et al.* (88) examined the spatial conformation of a flexible fiber in a homogeneous isotropic turbulence flow experimentally. They proposed a model for the transition from rigid to flexible regimes as the turbulence intensity increases or the fiber elastic energy decreases. They found that the straightening of the fibers, which becomes more evident as the length of the fiber increases, is due to the spatial and temporal correlations of the turbulent forcing. Niskanen *et al.* (89) performed both experiments and numerical simulations of a dilute suspension of flexible wood fibers in a contracting turbulent channel flow to identify the mechanisms affecting the development of fiber orientation. They observed that the orientation anisotropy obeys approximately a linear relation to the contraction ratio, meaning that the streamwise flow acceleration is the main mechanism affecting the development of the fiber orientation. From a numerical point of view, Andrić *et al.* (56) studied the translation and re-orientation of the fibers in a turbulent channel flow. They found that the fiber motion is primarily governed by velocity correlations of the flow fluctuations. They also highlighted the tendency of the fibers to evolve into complex geometrical configurations. Dotto *et al.* (86) performed a statistical characterization of the bending dynamics of inertial flexible fibers dispersed in a turbulent channel flow, finding that fibers retain a more deformed conformation in the center of the channel while they stretch near the wall region by the effect of the mean shear. Moreover, they found that the fiber end-to-end distance reaches a steady-state regardless of fiber location with respect to the wall. Rosti *et al.* (90, 91) studied the interaction between fiber elasticity and turbulent flow. They identified the flapping regime in which the fiber, despite its elasticity, is effectively slaved to turbulent fluctuations and, therefore, they can be used as a proxy to measure various two-point statistics of turbulence.

To the best of the authors' knowledge, there is no study available analyzing the behavior of flexible fibers in the cellular flow that employs a particle-level fiber model where a fiber is represented as a chain of cylindrical rods. To contribute to fulfilling this limitation, the present study is built on the model proposed by Schmid *et al.* (45) and Switzer III & Klingenberg (47) to investigate the dynamics of long flexible fibers suspended in a Newtonian viscous cellular fluid flow. Such a flow setup has been proposed to capture some of the dynamics of biological polymers in motility assays (92). Additionally, understanding the fiber configurational transitions has been proven to provide useful information for biological and fluid dynamics communities, for instance, in emerging nanotechnology for directed transport, assembling, sorting, and sensing of molecules (93–96), and nanometer-sized cargo in cellular-sized synthetic devices, as well as in sorting pulp fibers in the paper-making process (70). In the model used, each fiber is treated as a chain of massless rigid cylindrical segments connected by ball and socket joints. The model includes realistic features of fibers, such as flexibility and irregularly deformed equilibrium shapes and, in comparison to the previous studies, it can particularly provide additional information on the behavior of the fibers with respect to their equilibrium shape. Moreover, the mode considers one-way interaction between the fibers and the fluid flow while fiber-fiber interactions and Brownian motion are neglected. On each segment, the hydrodynamic forces and torques, the bending and twisting torques between each neighboring pair of segments, as well as the internal constraint forces and moments are applied. The purpose of this work is to study the dynamics and the deformation of fibers in a steady cellular flow, depending on the fiber stiffness, aspect ratio, and equilibrium shape. To this end, the shape evolution of fibers initially aligned with the flow direction is evaluated using the curvature of the fiber and the curvature of fluid flow at different distances from the center of vortices. Moreover, to gain a general understanding of the effects of fiber flexibility and initial positions and orientations on fiber transport, the analysis of fiber trajectories is performed.

3.2 Simulation Method

The fiber model used in this work is based on the model proposed by Schmid *et al.* (45) and Switzer III & Klingenberg (47). Thus, for the purpose of completeness, this section describes the main features of the model and highlights the modifications applied in the present work.

As illustrated in Figure 4.1, a flexible fiber is modeled as a chain of N_{seg} rigid inextensible cylindrical segments connected through $N_{seg} - 1$ hinges. All fiber segments have the same diameter D and length l, representing the fibers with aspect ratio $r_f = L/D = N_{seg} l/D$. The position vector $\vec{r}_i$ points to the center of mass of the segment i, and the unit vector $\vec{p}_i$ describes the segment orientation with respect to the non-inertial coordinate system. Fiber and fluid inertia are neglected because of the small Reynolds numbers under creeping flow conditions (here $\mathrm{Re} = \rho\dot{\gamma}LD/\mu \ll 1$ where ρ, $\dot{\gamma}$, and μ are the density of the fluid, shear rate, and fluid viscosity, respectively) (45). Moreover, given the behavior of the fibers studied for dilute flow conditions, the hydrodynamic interactions between the fibers are neglected.

The motion of each fiber segment i is governed by Euler's first (Equation (3.1)) and second law (Equation (3.2)) together with the connectivity constraint (Equation (3.3)) as follows:

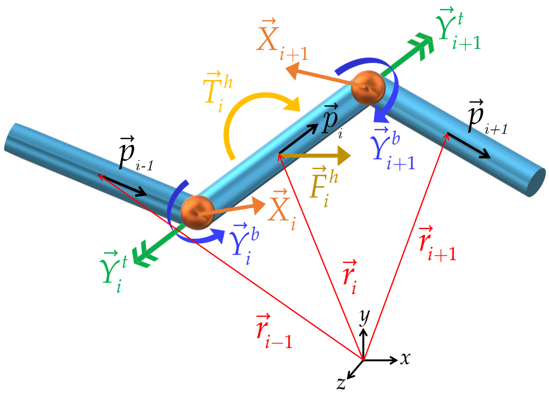

FIGURE 3.1: Fiber geometry, forces and torques applied

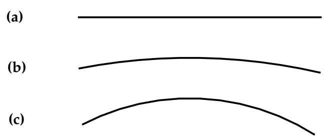

FIGURE 3.2: Equilibrium shape for a fiber with $N = 11$, $\phi^{eq} = 0$ and (a) $\theta^{eq} = 0$; (b) $\theta^{eq} = 0.1$; and (c) $\theta^{eq} = 0.2$

$$\vec{F}^h_i + \vec{F}^b_i + \vec{X}_{i+1} - \vec{X}_i = \vec{0} \tag{3.1}$$

$$\vec{T}^h_i + \vec{Y}_{i+1} - \vec{Y}_i + \left(\frac{l}{2}\vec{p}_i\right) \times \left(\vec{X}_{i+1}\right) + \left(\frac{-l}{2}\vec{p}_{i+1}\right) \times \left(-\vec{X}_i\right) = \vec{0} \tag{3.2}$$

$$\vec{r}_i + \frac{l}{2}\vec{p}_i - \left(\vec{r}_{i+1} - \frac{l}{2}\vec{p}_{i+1}\right) = \vec{0} \tag{3.3}$$

In Equation (3.1), $\vec{F}^h_i$ is the hydrodynamic drag, $\vec{F}^b_i$ is the body force, $\vec{X}_i$ and $\vec{X}_{i+1}$ are the connectivity forces in the hinges at the two ends of the segment i. In Equation (3.2), $\vec{T}^h_i$ is the hydrodynamic torque, $\vec{Y}_i = \vec{Y}^b_i + \vec{Y}^t_i$ is the sum of the bending torque ($\vec{Y}^b_i$) and twisting torque ($\vec{Y}^t_i$) in the joint i, and $\vec{Y}_{i+1}$ is the analogous for the joint $i+1$. For the end segments $\vec{X}_1 = \vec{X}_{N+1} = \vec{0}$ as well as $\vec{Y}_1 = \vec{Y}_{N+1} = \vec{0}$.

The hydrodynamic force and torque on the segment are $\vec{F}^h_i = \bar{\bar{A}}_i \cdot \left(\vec{v}^\infty_i - \dot{\vec{r}}_i\right)$ and $\vec{T}^h_i = \bar{\bar{C}}_i \cdot \left(\vec{\Omega}^\infty_i - \vec{w}_i\right) + \bar{\bar{H}}_i : \overline{\overline{E}}^\infty$, respectively, where $\bar{\bar{A}}_i$, $\bar{\bar{C}}_i$, and $\bar{\bar{H}}_i$ are the resistance tensors that are approximated by the corresponding resistance tensors of a prolate spheroid with an equivalent aspect ratio proposed by Kim & Karrila (97); $\vec{v}^\infty_i$, $\vec{\Omega}^\infty_i = \frac{1}{2}\left(\nabla \times \vec{v}^\infty_i\right)$, $\bar{\bar{E}}^\infty = \frac{1}{2}\left(\nabla\vec{v}^\infty_i + \left(\nabla\vec{v}^\infty_i\right)^t\right)$ are the translational fluid velocity, the angular fluid velocity and the rate of strain tensor, respectively, all evaluated at the center of mass of the segment i. $\dot{\vec{r}}_i$ and $\vec{\Omega}_i^{\infty}$ are the translational and angular velocities of the center of mass of segment i. The bending and twisting torques ($\vec{Y}_i^b$ and $\vec{Y}_i^t$), represent the fiber resistance to the flow acting to restore its equilibrium shape. These torques are assumed to be proportional to the difference between the angle at the joint i formed by connected segments:

$$\vec{Y}_i^b = -k_b \left(\theta_i - \theta_i^{eq}\right) \vec{e}_i^b \,, \vec{Y}_i^t = -k_t \left(\phi_i - \phi_i^{eq}\right) \vec{e}_i^t \tag{3.4}$$

here k_b and k_t are the bending and twisting stiffness constants, $\vec{e}_i^b$ and $\vec{e}_i^t$ are the unit vectors in the bending and twisting torque directions. θ and ϕ are the bending and twisting angles of the segment whereas θ_i^{eq} and ϕ_i^{eq} are the equilibrium angles describing fiber equilibrium shapes when no forces or torques are acting on it (see Figure 4.2). For an intrinsically straight fiber, θ_i^{eq} and ϕ_i^{eq} are zero, for a permanently deformed U-shaped fiber with an intrinsic radius of curvature R_u, $\theta^{eq} = 2\tan^{-1}\left(L/(2R_u)\right)$ is constant at every joint and $\phi_i^{eq} = 0$, and in the case both θ_i^{eq} and ϕ_i^{eq} are non-zero constants at every joint, the fiber has an intrinsic helical shape (45).

The reader is referred to Reference (45) for details of the discretization of the motion equations and the numerical algorithm to solve them.

Assuming the fluid flow velocity vector $\vec{U}(t) = \left(u_x, u_y, u_z\right)$, the curvature of the flow streamlines can be calculated (98):

$$\kappa_{flow}(t) = \frac{\left\|\vec{U}(t) \times \vec{a}(t)\right\|}{\left\|\vec{U}(t)\right\|^3} \tag{3.5}$$

Here $\times$ is the cross product, and $\vec{a}(t)$ is the acceleration field that for a steady flow can be computed as:

$$\vec{a}^t(t) = \nabla\vec{U}(t) \cdot \vec{U}^t(t) \tag{3.6}$$

To analyze the evolution of the fiber shape, the curvature of each fiber segment κ_i is evaluated as

$$\kappa_i = \frac{1}{R_i} \tag{3.7}$$

where R_i is the radius of the circle that is determined by the center of mass of the three consecutive segments. For the end segments, $\kappa_1 = \kappa_{N+1} = 0$.

3.3 Validation

The fiber model validation is performed by comparing the simulation results for both rigid and flexible fibers to well-known theoretical and experimental results. Jeffery (8) studied the motion of an isolated rigid ellipsoidal particle in a simple shear flow $\vec{U} = (\dot{\gamma}y, 0, 0)$, where $\dot{\gamma}$ is the shear rate of the flow (see Figure 4.3). The periodic trajectories of the particle ending points, known as Jeffery orbits, can be described in spherical coordinates by

$$\tan\theta = \frac{C\, r_s}{\left[r_s^2 \cos^2\phi + \sin^2\phi\right]^{1/2}} \tag{3.8}$$

$$\tan\phi = r_s \tan\left(\frac{2\pi t}{T} + k\right) \tag{3.9}$$

where C is the orbit constant, k is the phase angle, $T = 2\pi\left(r_s + r_s^{-1}\right)/\dot{\gamma}$ is the orbit period, θ is the angle between the unit vector along the cylinder ($\vec{p}$) and the vorticity axis (z-axis), and ϕ is the angle between the projection of the unit vector $\vec{p}$ on the flow-gradient plane and the x-axis (see Figure 4.3). Bretherton (10) expanded Jeffery's solution to any axisymmetric particle when r_s is replaced with an effective aspect ratio r_e. Cox (11) found the semi-empirical correlation $r_e = 1.24 r_f \big/ \sqrt{\ln r_f}$ for a circular cylinder with an aspect ratio of r_f.

Figure 4.4 illustrates the trajectories of one end point of an isolated rigid fiber centered at the origin for different orbit constants C, obtained by varying the initial Euler angles (θ and ϕ). The solid lines are the path predicted from Jeffery's solution (Equation (3.8) and (3.9)), and the markers are from the simulations of a rigid fiber with $N = 11$, $r_f = 110$, and $BR = 2$ (the parameter BR describes the fiber flexibility and can be calculated as $BR = E_Y\left(\ln(2r_e) - 1.5\right) \big/ 2\mu\dot{\gamma}r_f^4$ where E_Y is Young modulus and r_f is the fiber aspect ratio). It is seen that there is an excellent agreement between the numerical results and the Jeffery's theory for the rigid fiber.

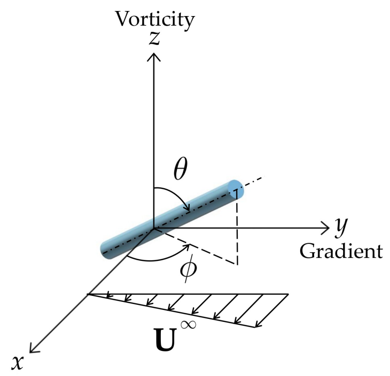

FIGURE 3.3: Euler angles for a cylindrical rigid fiber exposed to a shear flow

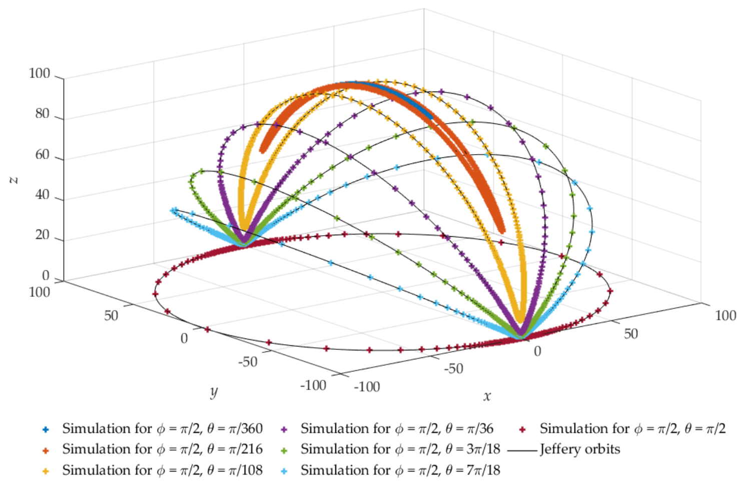

FIGURE 3.4: The orbits of a rigid fiber with $N = 11$, $r_f = 110$ for different Euler angles (θ, ϕ); "+" are simulated results, and solid lines are Jeffery orbits.

Figure 4.5 shows the non-dimensional Jeffery orbit period $T\dot{\gamma}$ as a function of fiber aspect ratio r_f for both predictions from Cox's semi-empirical correlation and the one computed from the numerical model employed. The simulation results reported are from isolated straight fiber (*i.e.*, $\theta^{eq} = \phi^{eq} = 0$) with $BR = 2$ (corresponding to an essentially rigid fiber) and various fiber aspect ratios. The fiber was initially placed aligned with the direction of a simple shear flow and, thus, it rotates in the gradient plane of the flow. As it can be seen in Figure 4.5, a good agreement between the computed periods and the theoretical prediction is found for the range of fiber aspect ratios analyzed.

The implemented method was also used to reproduce the motion of an isolated

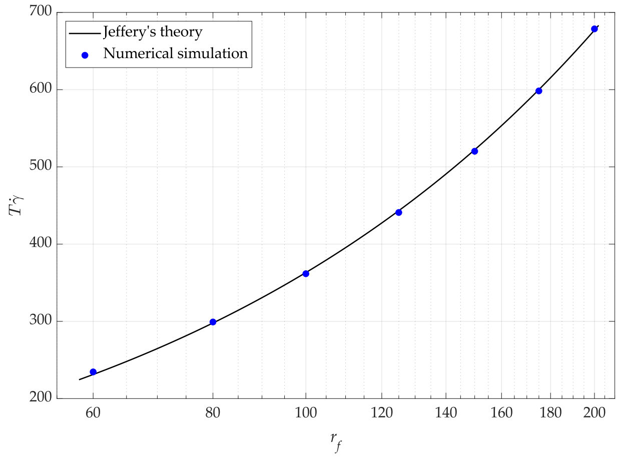

FIGURE 3.5: The dimensionless orbit period of Jeffery orbit $T\dot{\gamma}$ plotted as a function of the aspect ratio r_f. The solid line represents the prediction from Cox's semi-empirical correlation, and the filled circles are from the numerical simulations

flexible fiber in shear flow for different fiber stiffnesses. Forgacs and Mason (49) experimentally studied the motion of threadlike particles in shear flows. By varying shear rate, fiber stiffness and fiber length, they observed different rotation regimes such as rigid, springy, snake-like, helix and coiled motion with self-entanglement. Figure 4.6 shows the orbiting behavior of a fiber with $r_f = 250$, $N = 25$ (to ensure sufficient discretization for capturing fiber deformation) and three different values of the bending ratio $BR = 2, 1, 0.1$. It is predicted that a cylindrical fiber bends when $BR < 1$ (45), however, in agreement with Schmid *et al.* (45), the modeled intrinsically straight fiber behaves stiffer than actual fibers, and it bends at $BR < 0.1$. Additionally, an intrinsically straight fiber exhibits a snake-like S-shaped deformation (Figure 4.6d). However, implementing a small permanent deformation to mimic the geometrical imperfection of physical fibers (here, $R_u = 100L$ (45)), leads to a Snake-like C-shaped fiber deformation (Figure 4.6c), as reported in the experimental studies (49, 99). In conclusion, the numerical results are qualitatively in agreement with experimental observations of Forgacs and Mason (49).

Figure 4.7 depicts the surface plots of the evolving (absolute value of) curvature along the arclength of the fiber as a function of time, corresponding to the simulation runs depicted in Figure 4.6. A rigid fiber (Figure 4.7a) maintains its initially straight shape, and therefore there is no deformation in its curvature surface plot. For the S-shaped motion (Figure 4.7c), the fiber buckles and two bends occur during

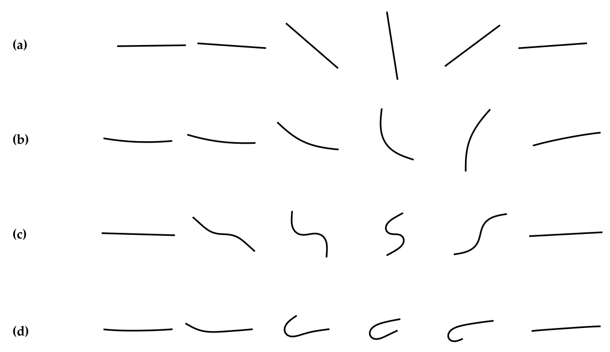

FIGURE 3.6: The time series of images from simulations showing shape evolution of fibers in simple shear flow. Three types of orbits can be seen for a fiber with $r_f = 250$, $N = 25$: (a) "Rigid", for fiber with the intrinsic radius of curvature $R_u = 100L$ (*i.e.*, $\theta^{eq} \approx 0.01$) with $BR = 2$; (b) "Springy", for fiber with the intrinsic radius of curvature $R_u = 100L$ (*i.e.*, $\theta^{eq} \approx 0.01$) with $BR = 1$; (c) "Snake-like S-shaped", for intrinsically straight fiber with $BR = 0.1$; (d) "Snake-like C-shaped", for fiber with the intrinsic radius of curvature $R_u = 100L$ (*i.e.*, $\theta^{eq} \approx 0.01$) with $BR = 0.1$. For the sake of visualization, the fiber diameters are exaggerated.

rotation. In this case, the positions of the maximal curvature do not travel along the arclength of the fiber while they occur as standing waves appear periodically in each orbit. In the case of snake-like C-shaped deformation (Figure 4.7d), in any orbit, fiber bends from one endpoint and the point of maximal curvature travels along the fiber arclength toward another fiber endpoint until it regains its straight shape. In all simulations shown in Figure 4.7, the fiber exhibits periodic motion; it remains most of the time in the straight configuration and aligned with the flow direction.

3.4 Results and Discussion

In this work, the behavior of flexible fibers flowing in one cell of a lattice of counter-rotating vortices (57) is studied. Since the flow streamlines are closed, inertialess point-like particles became trapped in the vortices. Moreover, this vortical flow contains stagnation points generating compression-elongation rates, and the fiber may deform, which makes this flow an interesting choice for analyzing the shape evolution and transport of flexible fibers.

The two-dimensional steady velocity field of the cellular flows, is described by (57)

$$u_x = U_0 \left(\sin(\tilde{x}) cos\left(\tilde{y}\right)\right) \tag{3.10}$$

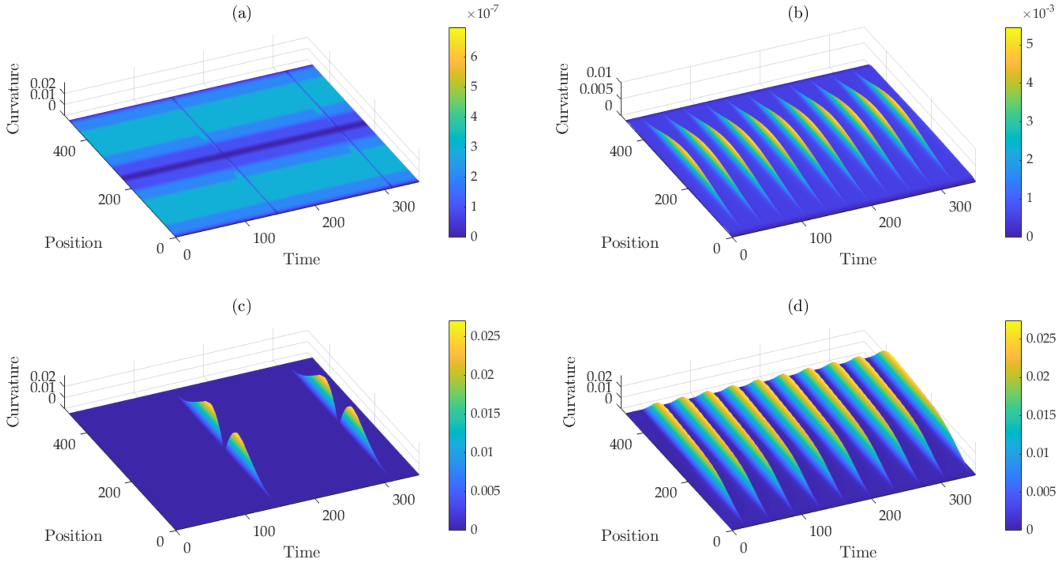

FIGURE 3.7: Surface plots of the (absolute value of) curvature as a function of time and fiber arclength; panels (a)-(d) correspond to the cases depicted in Figure 4.6a-d, respectively.

$$u_y = U_0 \left(-cos\left(\tilde{x}\right)\sin\left(\tilde{y}\right)\right) \tag{3.11}$$

Here $\tilde{x}$ (resp. $\tilde{y}$) is the dimensionless coordinate $\pi x/2W$ (resp. $\pi y/2W$) in which $2W$ is the cell size. In this study, $U_0 = 1$ and $W = 600\pi$, to have the simulation box with side lengths of at least four times bigger than the longest fiber considered in this study ($2W \geq 4L_{max}$) (45).

Figure 4.8a depicts the velocity field, while Figure 4.8b shows the vorticity field of one cell of the background cellular fluid flow in a square box computational domain of size 1200π. Figure 4.9a illustrates the streamline curvature field and Figure 4.9b shows, as an example, the time-averaged fiber curvature field computed from a total of 400 fibers initially aligned with flow direction over 25×10^3 dimensionless time period that was sufficient time for the fibers to reach their steady-state shapes. In order to compute the fiber curvature field, the computational domain was divided into 80×80 identical square cells and the fiber curvature was calculated by averaging the curvatures of the segments in which their center of masses lie within the cell. By comparing Figure 4.9a and Figure 4.9b, it is seen that, for the conditions considered $\left(N, r_f, DS, \theta^{eq}, \phi^{eq}\right) = (11, 220, 0.1, 0.01, 0)$, the fiber curvature field is is in qualitative agreement with the streamline curvature field.

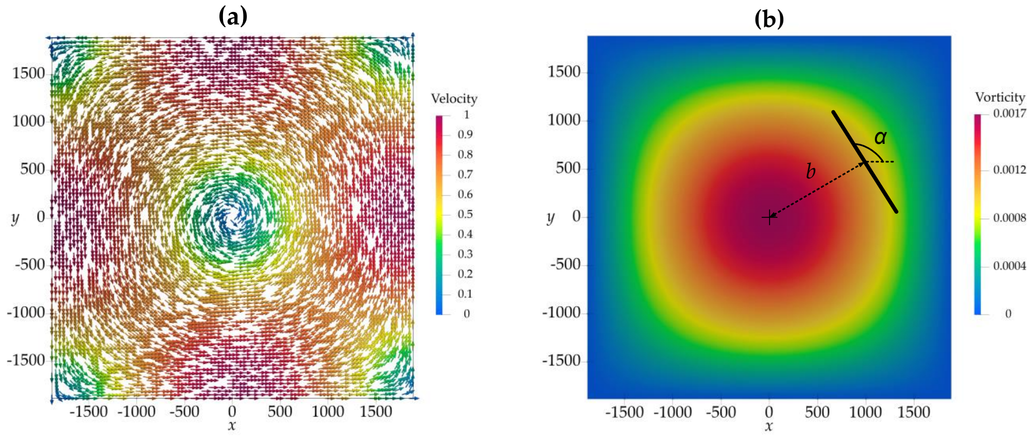

FIGURE 3.8: (a) Velocity field, and (b) Vorticity field

Several numerical experiments were performed to gain a general understanding of the effects of initial fiber positions and orientations, as well as fiber stiffness on the transport and shape evolution of flexible fibers in a viscous cellular flow. The motion of fibers initially placed at various distances from the center of vortices $b = 1000, 1200, 1500, 1700, 1800, 1850, 1870, 1880$, and oriented at two different angles measured from the x-axis of $\alpha = 0°$ (*i.e.*, along x-axis) and $\alpha = 90°$ (*i.e.*, along y-axis) was tracked (see figure 4.8b for the definitions of α and b). Figure 4.10 shows the trajectories of the center of mass of the fibers. In addition, the observations of the selected cases with $(b, \alpha) = (1700, 0°), (1800, 0°)$, and $(1850, 0°)$ are provided as the Supplemental Material Movie S1. In agreement with the study of Wandersman *et al.* (*57*), two main types of fiber dynamics were observed. In one dynamical state, the fiber is trapped within the vortex (Figure 4.10a,b) and follows roughly the flow streamlines. The trapped fibers demonstrate oscillations about the mean trajectory, which can span the trajectory of the fiber toward the cell compression regions. Another dynamical state occurs for the fibers that are initially located either very close to or inside the compression region (Figure 4.10c,d). In this state, the fibers meander across the vortical arrays and show transition from orbiting about one vortex to another one (*63*). Similar to the observation of Wandersman *et al.* (*57*), fibers also show a staircase-like motion across the lattice of vortices (see the case in cyan in Figure 4.10d).

Figure 4.11 depicts successive snapshots taken from the instantaneous shape of

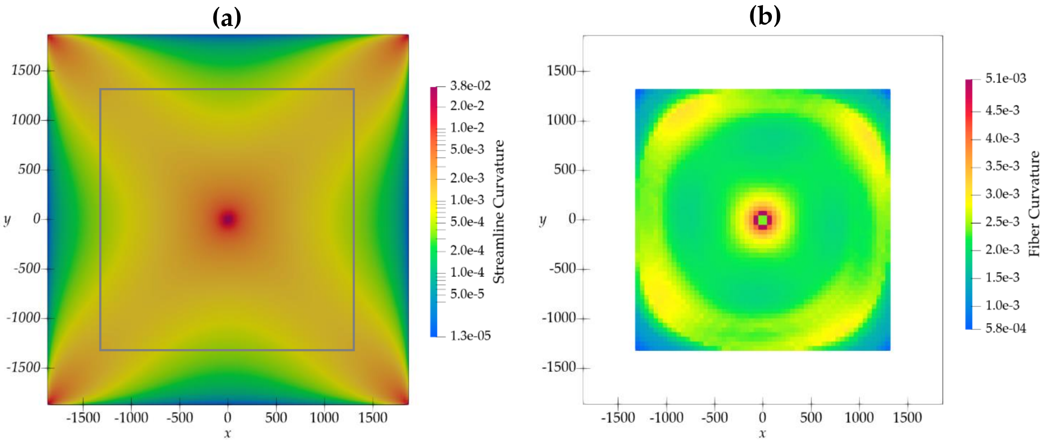

FIGURE 3.9: (a) Flow streamline curvature field in logarithmic scale, and (b) Fiber curvature field $\left(N, r_f, DS, \theta^{eq}, \phi^{eq}\right) = (11, 220, 0.1, 0.01, 0)$. Note that the area with no presence of fibers is removed from the fiber curvature field; the square box highlighted in the streamline curvature field is the corresponding area to the selected area shown in the fiber curvature field.

two isolated fibers with different dimensionless stiffness $DS = \pi BR/[32(\ln 2r_e - 1.5)]$ (11, 45). Both fibers are placed at $b = 1850$ and aligned with y-axis (*i.e.*, $\alpha = 90°$). The rigid fiber with $DS = 1$ (on the left) does not buckle and maintains its straight shape, while the flexible fiber with $DS = 1 \times 10^{-2}$ (on the right) buckles and shows different modes of deformation. Since the flow streamlines are closed and the fibers are without inertia, they remain trapped in the vortices of the cell.

As illustrated in Figure 4.11 and in Supplemental Material Movie S1, depending on the fiber initial conditions and stiffness, fiber undergoes different deformation modes, including straight, nearly straight, "J", "C", and "U" shapes.

The effects of fiber stiffness, fiber equilibrium shape and fiber aspect ratio on the shape deformation of flexible fibers in cellular flow are analyzed as well. To perform such a parametric study, the fibers were considered to be made from vinylpolysiloxane, as reported in (63), with a density of $1.1 \times 10^3 kg.m^{-3}$, a fixed radius of 41 μm, and different lengths ranging from 5.8 mm to 23 mm. The fibers considered in Reference (63) have Young's modulus ranging from 20 kPa to 570 kPa ; however, this study analyses a wider range $[0.2 - 2000]$ kPa] to elucidate the effect of the fiber stiffness using a more inclusive series of stiffnesses. The fibers equilibrium shape can vary

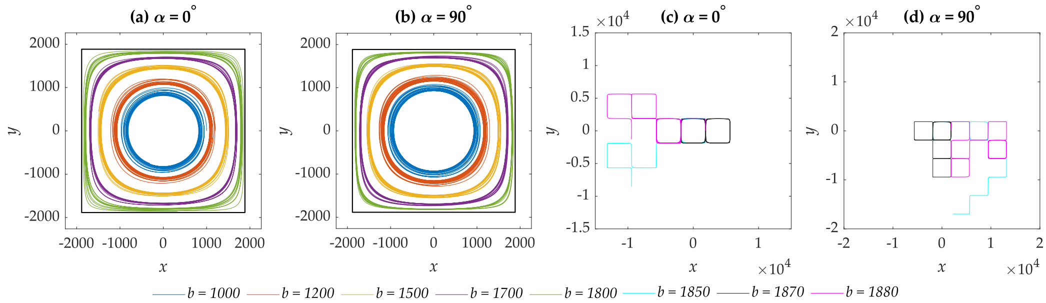

FIGURE 3.10: Trajectories of the center of mass of fibers located at different distances from the center of vortices, $b = 1000, 1200, 1500, 1700, 1800, 1850, 1870$, aligned either along x-axis ($\alpha = 0°$) or y-axis ($\alpha = 90°$); the fibers with trajectories shown in panels (a) and (b) have stayed trapped within the vortex and the ones with trajectories shown in panels (c) and (d) have escaped from the cell.

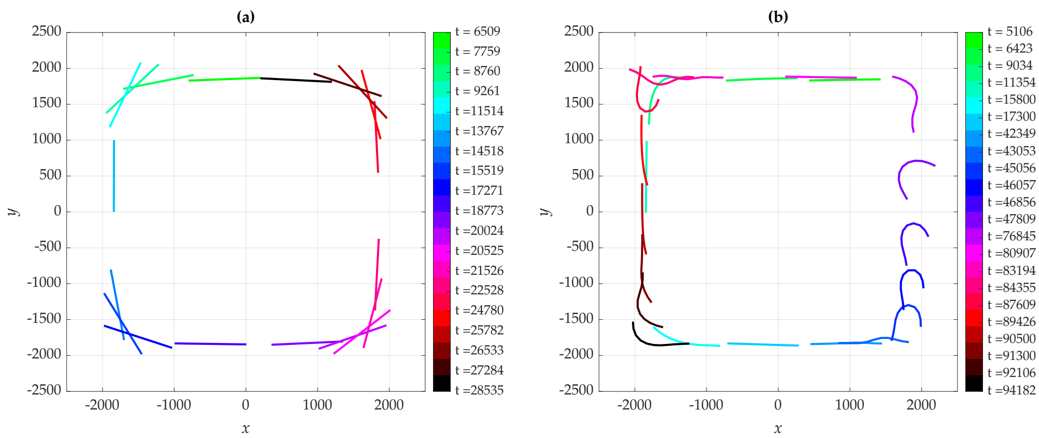

FIGURE 3.11: Successive snapshots of the instantaneous shape of (a) an isolated rigid fiber and (b) a flexible fiber. The fiber diameters are exaggerated for the purpose of visualization.

from straight fiber ($\theta^{eq} = \phi^{eq} = 0$) to a relatively U-shaped one by taking equilibrium bending angles of $\theta^{eq} = 0.1$ and 0.2 (see Figure 4.2). The fluid medium was considered to be a mixture of polyethylene glycol 1000 (Fluka) and purified water, exhibiting a viscosity of 82 $mPa.s$ and density $1.25 \times 10^3 kg.m^{-3}$ (63). In all the following simulations, 64 fibers each consisting of 11 segments are tracked for different combinations of values (DS, θ^{eq}, r_f). In each case reported, the fibers are initially distributed uniformly in the computational domain, aligned with the flow direction and the velocity of the fluid. The dimensionless time step used is 10^{-3} and the motion of the fibers are tracked over a time span of 50×10^3 dimensionless time.

3.4.1 Effects of fiber stiffness

Simulations were performed for various values of the dimensionless stiffness $DS = \pi BR/[32(\ln 2r_e - 1.5)]$: $DS1 = 4.2 \times 10^{-6}$, $DS2 = 4.2 \times 10^{-5}$, $DS3 = 4.2 \times 10^{-4}$, $DS4 = 4.2 \times 10^{-3}$, $DS5 = 4.2 \times 10^{-2}$, corresponding respectively to the fibers with Young's modulus of $E_{y1} = 0.2\,kPa$, $E_{y2} = 2\,kPa$, $E_{y3} = 20\,kPa$, $E_{y4} = 200\,kPa$, $E_{y5} = 2000\,kPa$, while other parameters were kept fixed at $\left(N, r_f, \theta^{eq}, \phi^{eq}\right) = (11, 143, 0.01, 0)$ (here, fiber length and diameter are $L = 11.72\,mm$ and $D = 8.2\,\mu m$, respectively). Figure 3.12 shows the time evolution of the ratio between fiber curvature to the curvature of flow streamline $\xi = \kappa_{fiber}/\kappa_{flow}$ (Equation (3.5) and (3.7)) as a function of time and the distance from the center of vortices (b). The standard deviations of the curvature data are indicated by error bars. As shown at the top of the left column of Figure 3.12, at dimensionless time of 1000, the value of ξ is very close to one for various distances from the center of vortices. The fibers are initially placed aligned with the flow direction and, therefore, at the early stages of the simulations, the fibers still have almost the same curvature as the flow streamline curvature (*i.e.*, $\xi \approx 1$).

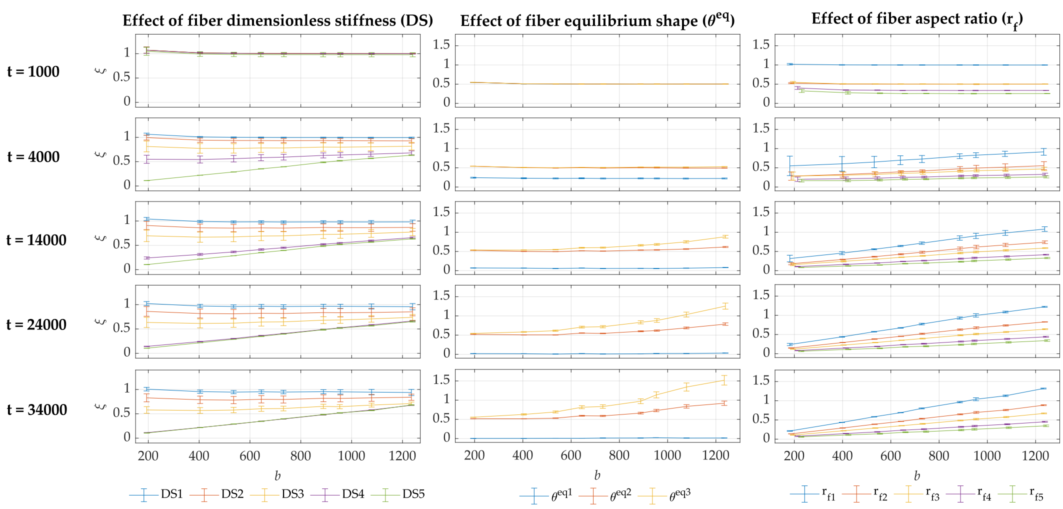

FIGURE 3.12: The value of $\xi = \kappa_{fiber}/\kappa_{flow}$ as a function of time and the distance from the center of vortices b. The plots in left column, with time advances from top to bottom, showing the effect of fiber stiffness ($DS1 = 4.2 \times 10^{-6}$, $DS2 = 4.2 \times 10^{-5}$, $DS3 = 4.2 \times 10^{-4}$, $DS4 = 4.2 \times 10^{-3}$, $DS5 = 4.2 \times 10^{-2}$); the middle column, showing the effect of fiber equilibrium shape ($\theta^{eq1} = 0$, $\theta^{eq2} = 0.1$, $\theta^{eq3} = 0.2$); the right column, showing the effect of fiber aspect ratio ($r_{f1} = 286$, $r_{f2} = 214.5$, $r_{f3} = 143$, $r_{f4} = 107.2$, $r_{f5} = 71.5$)

As time evolves, the restoring bending torques between each pair of neighboring segments (Equation (3.4)) push the fiber to regain its equilibrium shape. In this regard, the fibers having higher dimensionless stiffness behave more rigid and restore their equilibrium shapes ($\theta^{eq} = 0.01$) to a greater extent, therefore, they exhibit lower κ_{fiber} and ξ accordingly. In contrast, in the case of very flexible fibers (*e.g.*, $DS = 4.2 \times 10^{-6}$), the elastic forces cannot overcome viscous forces, and the fibers do not regain their equilibrium shape. Therefore, they remain almost aligned with the flow direction, with ξ ranging from 0.95 to 1 at any time.

As time progresses, the fiber relaxation phase occurs gradually, and the fiber deforms to regain its equilibrium shape. Figure 3.12 illustrates that, as time advances, the fiber straightens and eventually reaches its "*steady-state shape*" that is a slightly U-shaped fiber with $\theta^{eq} = 0.01$. The fibers, therefore, form smaller curvatures and the value of $\xi = \kappa_{fiber}/\kappa_{flow}$ decreases over time at any specific position (b). The simulation results presented in Figure 3.12 suggest that the stiffer fibers exhibit a quicker relaxation phase. For instance, after 4×10^3 dimensionless time, the fibers with $DS = 4.2 \times 10^{-2}$ reach to their steady-state shape, while the fibers with $DS = 4.2 \times 10^{-3}$, reach their steady-state shapes just after 24×10^3 dimensionless time. Here, the steady-state shapes is determined as the time that the values of ξ became stable over time and their corresponding standard deviations are very small.

As it can be seen in Figure 3.13, for the case with $DS = 4.2 \times 10^{-3}$ at long times (*e.g.* 34×10^3 dimensionless time), the ξ is less than 0.1 for the fibers close to the center of vortices ($b < 200$), and it increases up to $\xi = 0.7$ for the fibers further from the center. This outcome is as to be expected since all the fibers have reached their steady-state shapes, with a constant curvature across the computational domain while the curvatures of the streamlines decrease from $\kappa_{flow} = 5 \times 10^{-3}$ at $b \approx 200$ to $\kappa_{flow} = 1 \times 10^{-3}$ at $b \approx 1200$ (see Figure 3.13).

3.4.2 Effects of fiber shape

Simulations were performed for the systems containing U-shaped fibers for several different equilibrium bending angles. The results are presented for numerical experiments of flexible fibers with $\theta^{eq} = 0, 0.1, 0.2$ (see Figure 4.2), while other parameters are kept fixed at $(DS, r_f, N) = (4.2 \times 10^{-3}, 143, 11)$, corresponding to fibers with $E_y = 20\,kPa$, $L = 11.72\,mm$ and $D = 8.2\,\mu m$. The effects of the fiber equilibrium

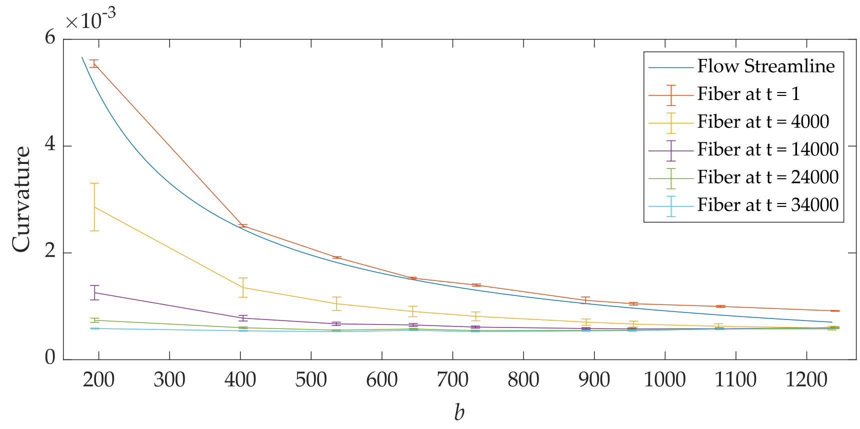

FIGURE 3.13: The values of the streamline curvature and fiber curvature (for the fibers with $(DS, r_f, \theta^{eq}, N) = (4.2 \times 10^{-3}, 143, 0.01, 11)$) as a function of distance from the center of vortices b, shown for five different times

shape on the value of ξ as a function of time and the distance from the center of vortices b are illustrated in the middle column of Figure 3.12. Although the fibers were initially placed aligned with the flow direction, even at the very beginning of the simulation (*e.g.*, $t = 1000$), the value of ξ for all cases is between 0.5 and 0.55. This is due to the strong impact of the fiber equilibrium shape on the bending behavior of fibers. This effect can be observed in the Supplemental Material Movie S2, where the motion of the fibers with $\theta^{eq} = 0.1$ is displayed for the total dimensionless time of 50×10^3. For the sake of visualization, the fiber diameters are exaggerated in the movie. There is a quick transition from the initial condition, where the fibers inherently represent $\xi = 1$, to $\xi \approx 0.5$ after 2.5×10^3 dimensionless time.

In the system containing fibers with $\theta^{eq} = 0$, as time evolves, the fibers deform to regain their steady-state shapes, resulting to a gradual decrease in ξ. Figure 3.12 demonstrates that after 24×10^3 dimensionless time the fibers are relaxed and almost perfectly straightened (*i.e.*, $\kappa_{fiber} \approx 0$, hence $\xi \approx 0$). However, as shown Figure 3.12, the fibers with $\theta^{eq} = 0.1$ experience values of ξ ranging from 0.5 (at $b \approx 200$) to 0.8 (at $b \approx 1200$). Thus, a small amount of intrinsic curvature can have a significant effect on the bending behavior of the fibers.

3.4.3 Effects of fiber aspect ratio

The plots in the right column of Figure 3.12 demonstrate the results of the simulations performed for fibers with five different aspect ratios $r_f = 71.5, 107.2, 143, 214.5, 286,$

corresponding to fibers with diameter $D = 8.2\,\mu m$ and lengths of $L_1 = 23.45\,mm$, $L_2 = 23.45\,mm$, $L_3 = 23.45\,mm$, $L_4 = 23.45\,mm$, $L_5 = 23.45\,mm$, with $(N, DS, \theta^{eq}, \phi^{eq}) = (11, 4.2 \times 10^{-3}, 0.01, 0)$ (here, the Young's modulus of the fibers was considered to be $E_y = 20\,kPa$). As it can be seen in Figure 3.12, at a given distance from the center of vortices, the fibers with a lower aspect ratio exhibit lower ξ. For the studied cases, this is to be expected; as the aspect ratio increases, the fiber behaves more flexible. Therefore the fibers adapt more to the flow streamlines and represent a bigger curvature compared to rigid fibers with a smaller aspect ratio. A similar discussion as the one made for the effect of fiber shape on the early-stage shape evolution of the fibers is valid here too for the early-stage values of ξ obtained (see Section 3.4.2).

After 24×10^3 dimensionless time, the value of ξ increases almost linearly with the distance from the center of vortices. As discussed in Section 3.4.1, once the fibers reach their steady-state shapes, they exhibit a fixed curvature across the computational domain, and since the streamline curvature decrease as b increases, the values of ξ increase accordingly.

3.5 Conclusions

In this chapter, simulations were performed to study the dynamics and shape evolution of flexible fibers in cellular flows. The particle-level rod-chain fiber model of Schmid *et al.* (*45*) and Switzer III & Klingenberg (*47*) was used to realistically capture the behavior of flexible fibers in a steady flow, while incorporating the realistic fiber features, including the fiber flexibility and non-straight fiber equilibrium shape. In all simulations, a total of 64 fibers, distributed uniformly in the computational domain, were tracked. The fibers were initially aligned with the flow direction with the velocity of the fluid, and their behavior was analyzed for different combinations of fibers stiffness, aspect ratio, and equilibrium shape. In addition, the motion of isolated fibers was carried out to study the fiber transport for several initial conditions (position and orientation) and different fiber stiffness.

It was observed that depending on the fiber stiffness, and initial condition, the fibers either became trapped in a vortex of a cell or were freely transported through an array of counter-rotating vortices while exhibiting different modes of fiber deformations, including straight, nearly straight, J-shaped, U-shaped, and C-shaped geometry. These findings indicate the significant impact of initial conditions and mechanical properties of the fiber on the fiber buckling and transportation. The results are in agreement with the numerical and experimental results of Wandersman *et al.* (57).

The typical fiber relaxation times were long, for example, about 34×10^3 dimensionless time for the fiber with (number of segments N, dimensionless stiffness DS, aspect ratio r_f, equilibrium bending angle θ^{eq}, equilibrium twisting angle ϕ^{eq}) $= (11, 4.2 \times 10^{-3}, 143, 0.01, 0)$. As expected, increasing the dimensionless stiffness led to a higher restoring bending torque and a more "rigid" behavior, which resulted in a quicker relaxation phase accordingly. Additionally, the findings showed that fibers with higher DS represent a lower ratio of fiber curvature to the flow streamline curvature ($\xi = \kappa_{fiber}/\kappa_{flow}$) than the more flexible fibers, meaning that they have regained their nearly straight equilibrium shapes to a greater extent.

The results obtained showed a strong influence of fiber equilibrium shape on the bending behavior of the fibers. For relatively flexible fibers with $\theta^{eq} = 0$ demonstrated a quick early-stage straightening from their initially flow-aligned configuration toward their straight equilibrium shape, and exhibit $\kappa_{fiber} = 0$ across the computational domain after 24×10^3 dimensionless time. However, even a small deviation in fiber equilibrium shape from a perfectly straight shape causes a significant change in the values of ξ. For example, system containing fibers with the intrinsic radius of curvature $R_u = 10L$ (*i.e.*, $\theta^{eq} \approx 0.1$) exhibits ξ ranging from approximately 0.5 (at the distance from the center of vortices $b \approx 200$) to $\xi \approx 0.8$ (at $b \approx 1200$) when the fibers reach their steady-state shapes.

The simulations performed for fibers with $(N, DS, \theta^{eq}, \phi^{eq}) = (11, 4.2 \times 10^{-3}, 0.01, 0)$ and various aspect ratio showed that fibers with higher r_f experience higher ξ. This is to be expected, since for a fixed diameter, longer fibers are more flexible than the shorter ones, and consequently, as they move along the flow direction, they deform to a greater extent to assume the shape of streamlines.

The work presented herein showed that the shape development of the fiber leads to complex fiber transport dynamics. In further studies, it would be worthwhile to conduct a detailed study on the origins of these dynamics, particularly the coupling between the fiber shape deformation and transport. It is recommended to perform further simulations with a wider range of fiber stiffnesses, equilibrium shape angles, and aspect ratios to gain a more detailed understanding of the fiber shape evolution in the studied flow field.

Chapter 4

Large eddy simulation of fiber flocculation in a diffuser

4.1 Introduction

Understanding the dynamics of inertial anisotropic particles in turbulent flows is a fundamental issue in multiphase flows, with significant relevance across various fields, from papermaking (*3*) to cloud ice-crystal formation (*100*) to the locomotion of microorganisms (*101*–*103*). Industries such as pulp and paper processing and composites production rely on achieving a uniform spatial distribution of fibers to ensure the quality of their end products (*65*, *104*). Consequently, the formation of fiber flocs is highly undesirable in these contexts, highlighting the need to disrupt or prevent their formation. Conversely, in drinking and wastewater treatment and physical filtration, the aggregation of suspended solids is a desired process. Therefore, a thorough understanding of the complex interactions between fibers and flows is necessary to accurately predict and control flocculation in flowing suspensions (*53*).

The interaction between non-spherical structures and turbulent flow is highly complex. In addition to the complexities introduced by turbulence in flows with spherical particles, forces and torques dependent on particle shape and orientation must also be considered (*80*, *81*). A comprehensive review of numerical models available for characterizing the translation and rotation of non-spherical particles in fluid flows was presented by Voth and Soldati (*80*). To examine the interaction between particles and turbulence at a particle scale, the Eulerian description of turbulence and the Lagrangian description of particles are commonly employed (105). When the particle Reynolds number is significantly smaller than unity, particles can be assumed to act as perfect flow tracers (59). Exact equations governing the evolution of particle orientation exist for both axisymmetric (8) and non-axisymmetric particles (106), providing valuable insight into the motion of elongated micro-swimmers and non-motile plankton cells in turbulent environments (6, 107, 108). However, when translational and rotational slip between the particle and the fluid cannot be disregarded, rigid body motion equations should be employed (59, 109), as previously has been done to investigate the motion of rigid ellipsoids in both viscous and turbulent flows (81, 85, 110–112). As the particle Reynolds number reaches unity or higher, the combined impact of fluid and particle inertia must be considered (113). Most studies concerned with the motion of rigid non-spherical particles in turbulence (83, 114, 115) highlight the particles' tendency to align with the direction of the strongest Lagrangian fluid stretching (84, 114). Furthermore, particle shape and size have been shown to affect inertia-driven phenomena such as preferential concentration and near-wall accumulation (81, 83, 85, 116).

Numerous studies have examined the impact of fiber and flow properties, as well as fiber concentration on the phenomenon of fiber flocculation. Schmid *et al.* (45) analyzed the effect of attractive and frictional forces on fiber aggregation and reported that fiber flocculation can be induced solely by inter-fiber friction, even in the absence of attractive forces. Switzer & Klingenberg (47) demonstrated the importance of fiber shape and deformability on their flocculation. Kerekes and Carolyn (117) studied fiber flocculation in dilute suspensions and showed that increased contact area and entanglement between longer fibers promote the formation of larger and more stable flocs. Fiber rotation not only directly impacts the behavior of individual particles by influencing drag forces (118) but also determines whether two particles in close proximity will collide or avoid each other (119). The frequency of fiber-fiber collision is affected by fiber motion relative to each other, and therefore, fiber suspensions with higher concentration experience a higher fiber collision frequency and demonstrate a higher degree of flocculation (45, 47). Moreover, when fiber trajectories significantly deviate from the flow streamlines, the fibers have an increased probability of crossing each other and forming flocs (53, 55, 56). Jafari *et al.* (120)

investigated the influence of contact and lubrication forces on floc formation and breakup of fibers in turbulent channel flow, observing the fibers' tendency to accumulate in high-speed streaks in the near-wall regions. Njobuenwu *et al.* (*116*) observed similar phenomena and reported that the translational dynamics of fibers, in terms of preferential concentration, are strongly dependent on their inertia and less dependent on their aspect ratio. Fiber-level simulations have demonstrated their efficacy in analyzing small-scale geometries containing up to 10^4 particles (*35*). However, to tackle larger geometries, Hämäläinen *et al.* (*35*) employed a Fiber Floc Evolution Model (FFEM) based on the integration of the population balance method and an Eulerian two-fluid approach, which elucidated that the size distribution of flocs is strongly influenced by local flow conditions.

Andrić *et al.* (*53*) studied the motion of rod-like fibers in the decelerating flow of a wedge-shaped channel using analytical and numerical methods, considering both infinite and finite hydrodynamic resistance to transverse flow. They identified the phenomenon of ballistic deflection, where fiber trajectories deviate significantly from the streamlines of the carrying flow. This phenomenon occurs when the direction of fiber inertia is aligned with converging/diverging or curved streamlines. A velocity difference between the fibers and the fluid develops due to fiber inertia and the gradients of the flow. For elongated fibers with an anisotropic hydrodynamic resistance tensor, this velocity difference is predominantly oriented in the longitudinal direction of the fiber. Andrić *et al.* (*53*) argued that ballistic deflection increases the relative motion of fibers, which may increase the collision rate and thus affect the rate of aggregation. Later, Andrić *et al.* (*55*) examined the flocculation of suspensions of rigid fibers in the decelerating flow field of a diffuser. They modeled the fibers using a particle-level fiber model and described the fluid flow using the two-dimensional steady-state Navier-Stokes equation with the standard $k-\omega$ turbulence model to account for the effects of turbulence, as well as a stochastic model to include the dispersion of fibers due to turbulence. The main finding of their study was that the anisotropic hydrodynamic resistance of fibers and the flow velocity gradients induce ballistic deflection of fibers, consequently causing fiber flocculation in the diffuser. Moreover, they observed that the kinematics of reinjected fibers in the computational domain strongly affect the flocculation in the horizontal inflow channel and at the entrance of the diffuser.

To the best of the our knowledge, no study has analyzed fiber suspensions in an asymmetric diffuser using Large Eddy Simulation (LES) to directly resolve the flow and the fiber-flow interaction in detail. In an effort to address this limitation, the present study builds upon the work of Andrić *et al.* (55) and provides a comprehensive investigation of the evolution of floc mass fraction, fiber trajectories, fiber slip velocities, alignment of fibers with respect to slip velocity and inertial coordinate, as well as fiber preferential concentration, to examine the development of fiber flocculation along the length of the diffuser. Specifically, the phenomenon of flow-induced ballistic flocculation, triggered by ballistic deflection of fibers, is analyzed for fibers with different inertias (controlled by varying the fiber density) and various fiber reinjection approaches (adjusting the orientation, linear, and angular velocity of the fibers upon their reinjection into the computational domain). Furthermore, to gain a general understanding of the effect of different levels of fluid flow resolution on the flocculation behavior, the results obtained from the present fully unsteady LES simulations of Newtonian fluids with constant properties are compared to the results of Reynolds-Averaged Navier-Stokes (RANS) simulations with a particle dispersion model, as previously studied by Andrić *et al.* (55).

4.2 Physical problem and numerical methods

In this chapter, a Lagrangian fiber model is employed to represent the fiber, alongside the Large Eddy Simulation (LES) equations to describe the behavior of the fluid flow. Within this model, a one-way coupling approach considers the effect of the fluid flow on the fibers, and a contact model is incorporated to capture interactions among fibers. Below, a summary of the fluid flow model, the fiber model, as well as the fluid-fiber and fiber-fiber interactions is presented.

4.2.1 Fluid flow model

For Large Eddy Simulation (LES) of incompressible flows, the filtered continuity and momentum equations are obtained by applying a filter with scale Δ to the

Navier–Stokes equations, yielding

$$\frac{\partial \bar{u}_i}{\partial x_i} = 0, \tag{4.1}$$

$$\frac{\partial \bar{u}_i}{\partial t} + \frac{\partial (\bar{u}_i \bar{u}_j)}{\partial x_j} = -\frac{1}{\rho}\frac{\partial \bar{p}}{\partial x_i} + \nu \frac{\partial^2 \bar{u}_i}{\partial x_j \partial x_j} - \frac{\partial \tau_{ij}}{\partial x_j}. \tag{4.2}$$

Here t is time, x_j is the spatial coordinate directions, u_j is the velocity vector, p is the pressure, ν is the fluid kinematic viscosity, and $\tau_{ij} = \overline{u_i u_j} - \bar{u}_i \bar{u}_j$ is the Sub-Grid Scale (SGS) tensor which represents the effect of the SGS motions on the resolved motions. Following the same approach as the Boussinesq hypothesis, the SGS stress can be modeled as

$$-\frac{\partial \tau^a_{ij}}{\partial x_i} \equiv \frac{\partial}{\partial x_i}(2\nu_{sgs}\bar{S}_{ij}). \tag{4.3}$$

Here τ^a_{ij} is the anisotropic part of the SGS tensor, $\bar{S}_{ij} = \frac{1}{2}\left(\frac{\partial \bar{u}_i}{\partial x_j} + \frac{\partial \bar{u}_j}{\partial x_i}\right)$ is the filtered strain rate tensor, and the coefficient of proportionality ν_{sgs} represents the SGS viscosity that should be determined using a SGS model.

Among the existing SGS models, the dynamic one-equation eddy viscosity model is used in the present work. This model represents a modified version of the standard one-equation model in which the SGS kinetic energy production term is solved by utilizing an SGS model based on resolved scales (*121*), while the eddy viscosity in the filtered equation of motion is computed using information derived from the unresolved scales in the transport equation of the SGS kinetic energy. In the standard one-equation model, the SGS eddy viscosity is given by $\nu_{sgs} = C_\nu \bar{\Delta}_\nu \sqrt{k_{sgs}}$, where $k_{sgs} = \left(\overline{u_i u_i} - \bar{u}_i \bar{u}_j\right)/2$ is determined by solving its transport equation (*122*–*124*)

$$\frac{\partial k_{sgs}}{\partial t} + \bar{u}_j \frac{\partial k_{sgs}}{\partial x_j} = -\tau_{ij}\bar{S}_{ij} - C_\epsilon k_{sgs}^{3/2}\bar{\Delta}^{-1} - \epsilon_w + \frac{\partial}{\partial x_j}\left[\left(C_d \Delta_\nu \sqrt{k_{sgs}} + \nu\right)\frac{\partial k_{sgs}}{\partial x_j}\right]. \tag{4.4}$$

Here, as suggested by Okamoto and Shima (*124*), the characteristic length Δ_ν and additional dissipation term ϵ_ω can be found from

$$\Delta_\nu = \bar{\Delta}(1 + C_k \bar{\Delta}^2 \bar{S}^2 / k_{sgs})^{-1}, \tag{4.5}$$

$$\epsilon_w = 2\nu \left(\frac{\partial \sqrt{k_{sgs}}}{\partial x_j}\right)^2, \tag{4.6}$$

where the non-dimensional constants for the one-equation model are $C_\nu = 0.05$, $C_\epsilon = 0.835$, $C_d = 0.10$ and $C_k = 0.08$. In the case of the dynamic one-equation SGS model, the first term on the right-hand side of Equation 4.4 can be calculated as

$$-\tau_{ij}\bar{S}_{ij} = C_s\bar{\Delta}^2|\bar{S}|^3, \tag{4.7}$$

in which C_s is evaluated from $C = -\frac{1}{2\bar{\Delta}^2}\frac{\langle L_{ij}M_{ij}\rangle}{\langle M_{ij}M_{ij}\rangle}$ that includes minimization of the error of $L_{ij} - \frac{1}{3}\delta_{ij}L_{kk} = -2C\bar{\Delta}^2 M_{ij}$ over all independent tensor components (125), as well as over some averaging region of statistical homogeneity (126). Here $M_{ij} = \frac{\tilde{\bar{\Delta}}^2}{\bar{\Delta}^2}\left|\tilde{\bar{S}}\right|\tilde{\bar{S}}_{ij} - \widetilde{\left|\bar{S}\right|\bar{S}_{ij}}$, the Germano identity $L_{ij} = T_{ij} - \tilde{\tau}_{ij} = \widetilde{\bar{u}_i\bar{u}_j} - \tilde{\bar{u}}_i\tilde{\bar{u}}_j$, $\bar{\Delta}$ and $\widetilde{\Delta}$ are the grid and test-filter scales, respectively (126, 127).

4.2.2 Fiber model

The particle-level fiber model used in this work is based on the model proposed by Lindström and Uesaka (46) and Andrić *et al.* (56), specifically developed for rigid straight fibers as done by Andrić *et al.* (55). For a comprehensive understanding of the model, readers are encouraged to refer to these references for a detailed description. In the interest of completeness, only the key characteristics of the model will be highlighted here.

To accommodate the variations in the flow field along the length of the fiber, the suspended fiber is treated as a chain of N_{seg} cylindrical segments, as illustrated in Figure 4.1 (only shown non-straight to highlight the segments). The segments have identical mass m_i, length l_i, diameter D_i and their unit vector is denoted as $\vec{p}_i$, where subscript i indicates the individual segments. The position vector of the center of mass (CM) of each segment is represented by $\vec{r}_i$. The center of mass of the fiber is $\vec{r}_G = \frac{1}{N_{seg}}\sum_{i=1}^{N_{seg}}\vec{r}_i$. Moreover, since the fiber is rigid, each segment has the same angular velocity as the fiber center of mass ($\vec{\omega}_i = \vec{\omega}_G$). The motion of each fiber segment is governed by Euler's first and second law, formulated as (56)

$$m\ddot{\vec{r}}_G = \sum_{i=1}^{N}\vec{F}_i^h, \tag{4.8}$$

$$\frac{\partial}{\partial t}\left(\bar{\bar{I}}_G\cdot\vec{\omega}\right) = \bar{\bar{I}}_G\cdot\dot{\vec{\omega}} + \vec{\omega}\times\left(\bar{\bar{I}}_G\cdot\vec{\omega}\right) = \sum_{i=1}^{N_{seg}}\vec{T}_i^h + \sum_{i=1}^{N_{seg}}(\vec{r}_i - \vec{r}_G)\times\vec{F}_i^h. \tag{4.9}$$

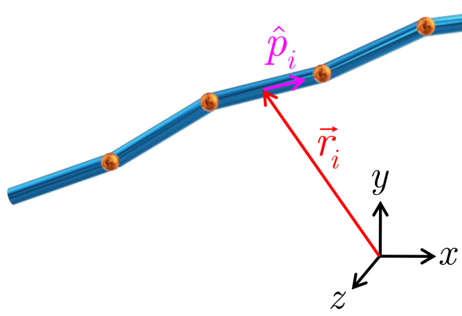

FIGURE 4.1: Illustration of a general non-straight fiber to highlight the segments. This study focuses solely on straight rigid fibers.

Here $m = \sum_{i=1}^{n} m_i$ is the fiber mass, and $\overline{\overline{I}}_G$ is the inertia tensor of the fiber with respect to its center of mass, $\vec{F}_i^h$ and $\vec{T}_i^h$ are the hydrodynamic drag force and torque exerted by the fluid on segment i.

4.2.3 Fluid-fiber interactions

The fiber Reynolds number is defined as

$$Re = \frac{\rho d |\dot{\vec{r}}_G - \vec{u}_G|}{\eta}, \tag{4.10}$$

where ρ is the fluid density, η is the fluid dynamic viscosity, and $|\dot{\vec{r}}_G - \vec{u}_G|$ is the magnitude of the relative velocity between the fiber and the flow at the center of mass of the fiber. According to Lindström and Uesaka (46), the hydrodynamic force ($\vec{F}_i^h$) and hydrodynamic torque ($\vec{T}_i^h$) can be approximated as a sum of the viscous ($Re \ll 1$) and the dynamic drag ($Re \gg 1$) contributions, *i.e.*

$$\vec{F}_i = \vec{F}_i^V + \vec{F}_i^I, \tag{4.11}$$

$$\vec{T}_i = \vec{T}_i^V + \vec{T}_i^I. \tag{4.12}$$

Here the viscous drag force $\vec{F}_i^V$ and torque $\vec{T}_i^V$ on each cylindrical segment are approximated as those acting on an isolated equivalent prolate spheroid of aspect ratio $r_e = 1.24 r_f \big/ \sqrt{\ln r_f}$ through

$$\vec{F}_i^V = \overline{\overline{A}}_i^V \cdot \left(\vec{v}_i^\infty - \dot{\vec{r}}_i\right), \tag{4.13}$$

$$\vec{T}_i^V = \bar{\bar{C}}_i^V \cdot \left(\vec{\Omega}_i^\infty - \vec{\omega}_i\right) + \bar{\bar{H}}_i^V : \bar{\bar{E}}^\infty. \tag{4.14}$$

Here $\bar{\bar{A}}_i^V$, $\bar{\bar{C}}_i^V$, and $\bar{\bar{H}}_i^V$ are the resistance tensors that are approximated by the corresponding resistance tensors of a prolate spheroid with an equivalent aspect ratio proposed by Kim and Karrila (*128*) and are not reported here for sake of brevity. $\vec{v}_i^\infty$, $\vec{\Omega}_i^\infty = \frac{1}{2}\left(\nabla \times \vec{v}_i^\infty\right)$, $\bar{\bar{E}}^\infty = \frac{1}{2}\left(\nabla \vec{v}_i^\infty + \left(\nabla \vec{v}_i^\infty\right)^t\right)$ are the translational fluid velocity, the angular fluid velocity and the rate of the strain tensor, respectively, all evaluated at the center of mass of segment i.

The dynamic drag force and torque on each fiber segment can be computed as (*46*)

$$\vec{F}_i^I = \bar{\bar{A}}_i^I \cdot \left(\vec{v}_i^\infty - \dot{\vec{r}}_i\right), \tag{4.15}$$

$$\vec{T}_i^I = \bar{\bar{C}}_i^I \cdot \left(\vec{\Omega}_i^\infty - \vec{\omega}_i\right) + \bar{\bar{H}}_i^I : \bar{\bar{E}}^\infty, \tag{4.16}$$

where the dynamic resistance tensors $\bar{\bar{A}}_i^I$, $\bar{\bar{C}}_i^I$, and $\bar{\bar{H}}_i^I$ are derived and validated by Lindström and Uesaka (*46*) and Andrić *et al.* (*56*).

4.2.4 Fiber-fiber interactions

The detection of fiber contacts involves implementing the shortest distance algorithm as described by Schmid *et al.* (*45*), Lindström and Uesaka (*46*) and Vega and Lago (*129*), not repeated here for brevity. Fibers can exist either in isolation or as part of a floc, where all fiber segments maintain fixed positions and orientations relative to each other. When two segments from different fibers or flocs come into contact, they immediately merge to form a single floc, with fixed relative positions of the fiber segments. Consequently, the floc behaves as a rigid body system, following Equation 4.8 and A.17 formulated for the center of mass of the floc to govern its motion. The equations of motion for fibers and flocs are discretized in time and solved to determine the linear and angular velocities of the fibers and flocs, which are subsequently used to calculate their updated positions and orientations. For a more comprehensive understanding of the numerical techniques and the limitations of the time step employed, please refer to the previous study conducted by Andrić *et al.* (*56*).

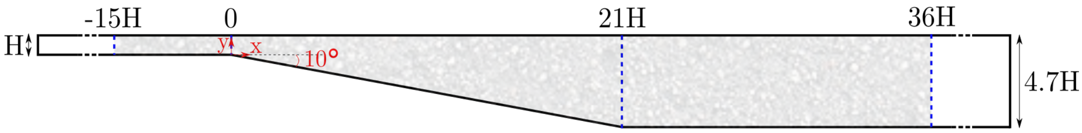

FIGURE 4.2: Schematic of Buice and Eaton asymmetric diffuser (131). The highlighted region denotes where the fibers are present. The inlet and outlet regions of the fluid flow are truncated for a better view.

4.3 Summary of simulations and definitions

4.3.1 Geometry and fluid flow modeling

Large eddy simulation (LES) of fiber suspension flow is conducted in an asymmetric planar diffuser, as illustrated in Figure 4.2. The highlighted region denotes where the fibers are present and the inlet and outlet regions make sure that the fiber interactions are not affected by the inlet and outlet effects of the flow simulation. The presence of an adverse pressure gradient causes flow separation, leading to the formation of a large recirculation bubble. This specific configuration has been chosen as it provides a good representation of the flow conditions encountered in the actual dry-forming process (55), and a highly reliable experimental database is available for validating the simulated flow (130, 131). A Cartesian coordinate system is employed, with the origin located on the upper wall where the inlet channel wall and the deflected wall intersect at a corner. The x-axis corresponds to the streamwise direction, the y-axis represents the upward direction, and the z-axis denotes the spanwise direction.

The diffuser is divided into three sections. The flow enters through an inlet channel with a height of H, a length of $70H$, and a width of $2H$ (where $H = 0.01\ m$). The asymmetric diffuser opens at an angle of 10° during $21H$, corresponding to an expansion ratio of $h_{out}/h_{in} = 4.7$. The outflow channel has a height of $4.7H$ and a length of approximately $15H$. To ensure a fully developed turbulent channel flow at the diffuser inlet, the upstream inlet section is sufficiently long. The governing equations are solved numerically using the OpenFOAM open-source CFD code (132). The inlet boundary specifies a constant bulk velocity of $U_b = 28\ m/s$. The flow reaches fully develop flow conditions during $55H$ before entering into the region of the fibers. The subgrid-scale (SGS) model employed is the Dynamic One-Equation

Eddy Viscosity Model, and the length scale is proportional to the cube root of the cell volume (*132*). For the incompressible continuity and Navier-Stokes equations in the LES, a second-order accurate upwind discretization scheme is utilized. The coupling between the continuity equation and the pressure field is accomplished using the pressure-implicit with the splitting of operators (PISO) algorithm (*133*). The convective and viscous terms are discretized using a second-order upwind scheme, while the pressure term is discretized using the corrected Laplacian scheme (*134*). Additionally, the transport equation for the subgrid-scale SGS kinetic energy is solved using the PBiCG solver with DILU preconditioner (*134*). Periodic boundary conditions are imposed in the x and z directions, while a no-slip boundary condition is applied to the top and bottom walls of the channel. Note that the system of coordinates, with origin located at the beginning of diffuser, is shown in Figure 4.2. The computational mesh comprises 840×120 cells and is appropriately refined to capture the gradients near the wall. The measured skin friction coefficient, C_f, in the fully developed entrance region is 0.0061 .The first cell centers are typically located at $y^+ \approx 42$.

A precursor fiber simulation was initiated when a fully developed fluid flow was established. The fibers were initially distributed randomly within the range $\{[-15H, 36H], [0, H], [-2H, 2H]\}$ in the x, y, and z directions, respectively, as in the work by Andrić *et al.* (*55*). The initial translational and angular velocities of the fibers were set equal to those of the fluid flow at the center of mass of each fiber. Fibers that are advected through $x = 36H$ are reinjected at $x = -15H$ to preserve the number of fibers in the computational domain. Fibers that hit the walls are assumed to stick to the wall, without affecting the properties of the wall, and are thus reinjected at $x = -15H$. Fibers that are advected through $z = H$ or $z = -H$ are moved to the other periodic side, as a periodic condition. A fully developed fiber flow was established after seven complete reinjections of all the fibers. The configuration of fiber segments and their kinematics from the precursor fiber simulation were saved and later used as the reference time zero for the parametric studies, to make sure that all simulations had the same initial conditions. Each fiber was assumed to consist of five segments with a diameter of 20 μm and a length of 0.2 mm, exceeding the Kolmogorov length scale of the carrier flow. These fiber properties were utilized in all simulations unless explicitly specified. The carrier fluid for the suspension was considered to be air, characterized by a density of $\rho = 1.2\,kg/m^3$ and a kinematic viscosity of $\nu = 1.4 \times 10^{-5}\,m^2/s$, representing Reynolds number of $\mathrm{Re} = \frac{U_b H}{\nu} = 18000$ at the inlet boundary.

4.3.2 Fiber reinjection approaches

The reinjection of fibers occurs through a random spatial distribution at the fiber reinjection plane $x = -15H$. The linear velocity, angular velocity, and orientation of the reinjected fibers have an influence on the initial trajectories of the fibers, and thus also on the initial flocculation rate. The effects of those properties on the flocculation rate are therefore parametrically studied as part of the present work. The rather long distance between the fiber reinjection plane and the entry of the diffuser is chosen to avoid the influence of the injection properties on the flocculation rate in the diffuser.

While the orientation can be chosen specifically or randomly, the linear velocity and angular velocity should be related to the background flow. In order to determine the linear velocity of each segment upon reinjection, it can first be assumed that the entire fiber is at mechanical equilibrium with either the instantaneous or time-averaged background flow, *i.e.,* the net forces acting on the particle is zero ($\sum_{i=1}^{N_{seg}} \vec{F}_i = \vec{0}$). Based on this assumption and considering only the viscous part of the drag force in Equation 4.8, the linear velocity of the fiber center of mass can be determined by averaging the fluid velocity (instantaneous or time-averaged) at the positions of the fiber segments as

$$\dot{\vec{r}}_G = \frac{\sum_{i=1}^{N_{seg}} \vec{v}_i^{\infty}}{N_{seg}}. \tag{4.17}$$

As the fiber is a rigid body, the reinjection velocity of each segment is given by

$$\dot{\vec{r}}_i = \dot{\vec{r}}_G + \vec{\omega}_{G_{SBR}} \times (\vec{r}_i - \vec{r}_G)\,. \tag{4.18}$$

Here the angular velocity due to the solid body rotation ($\vec{\omega}_{G_{SBR}}$) is determined from the relative velocity between each segment and the fluid flow at the position of its center of mass $\vec{v}_i^{\infty} - \dot{\vec{r}}_i = \vec{\omega}_{i_{SBR}} \times (\vec{r}_i - \vec{r}_G)$, and can be approximated as

$$\vec{\omega}_{G_{SBR}} = \frac{\sum_{i=1}^{N_{seg}} \vec{\omega}_{i_{SBR}}}{N_{seg}}. \tag{4.19}$$

As mentioned, the background flow velocity can be either the instantaneous ($\vec{U}^{\infty}_{\text{inst.}}$) or time-averaged ($\vec{U}^{\infty}_{\text{mean}}$) velocity. A general background velocity is here defined as

$$\vec{v}_i^{\infty} = (1-k)\vec{U}^{\infty}_{\text{mean}} + k\vec{U}^{\infty}_{\text{inst.}}, \tag{4.20}$$

introducing a factor k that for $k = 1$ represents the instantaneous flow field and for $k = 0$ represents the time-averaged velocity field.

The angular velocity of a fiber upon reinjection is set under the assumption of rotational equilibrium with the flow so that the fiber is not experiencing a net momentum (*i.e.*, $\sum_{i=1}^{N_{seg}} \vec{T}_i = \vec{0}$). By applying this assumption to Equation A.17, an equation to calculate $\vec{\omega}_{reinj}$ can be derived:

$$\vec{\omega}_{reinj} = \frac{\sum_{i=1}^{N_{seg}} \vec{\Omega}_i^{\infty} - \sum_{i=1}^{N_{seg}} \left(\bar{\bar{H}}_i^{V} : \bar{\bar{E}}^{\infty}\right) \cdot \left(\bar{\bar{C}}_i^{V}\right)^{-1}}{N_{seg}}. \tag{4.21}$$

Table 4.1 provides a summary of the simulation parameters used to characterize each case of fiber suspension. In Case 1, the reference fiber density of $\rho_{ref} = 1380\, kg/m^3$ is employed, and the computational domain for fiber flocculation simulations is restricted to the longitudinal diffuser direction within $[-15H, 36H]$. The linear velocity of each fiber segment is calculated using Equation 4.18 in which the instantaneous fluid velocity field ($k = 0$ in Equation 4.20) is considered. The fiber's angular velocity is initialized using Equation 4.21 to obtain $\vec{\omega}_{reinj}$, and the fiber orientation is assigned randomly. For Case 2, the reinjection approach is similar to Case 1, except for the linear velocity of the fibers. In Case 2, the longitudinal linear velocity component of each segment is set to the value obtained from Equation 4.18 for $k = 1$, *i.e.*, taking into account the time-averaged fluid velocity field $\vec{U}^{\infty}_{\text{mean}}$, while the other two velocity components are set to zero. Cases 3 and 4 share the same properties as Case 2, except for the orientation of the reinjected fibers. Specifically,

TABLE 4.1: Summary of cases and simulation parameters

Case	ρ (kg/m^3)	$\vec{u}_{\text{reinj.}}$	$\vec{\omega}_{\text{reinj.}}$	$\vec{p}_{\text{reinj.}}$	Fiber region (x-dimension)
C1	1380	(u_x, u_y, u_z)	(w_x, w_y, w_z)	Random	$[-15h, 36h]$
C2	1380	$(u_x, 0, 0)$	(w_x, w_y, w_z)	Random	$[-15h, 36h]$
C3	1380	$(u_x, 0, 0)$	(w_x, w_y, w_z)	$(1, 0, 0)$	$[-15h, 36h]$
C4	1380	$(u_x, 0, 0)$	(w_x, w_y, w_z)	$(0, 1, 0)$	$[-15h, 36h]$
C5	1380	$(u_x, 0, 0)$	$(0, 0, 0)$	Random	$[-15h, 36h]$
C6	460	(u_x, u_y, u_z)	(w_x, w_y, w_z)	Random	$[-15h, 36h]$
C7	460	$(u_x, 0, 0)$	(w_x, w_y, w_z)	$(1, 0, 0)$	$[-15h, 36h]$
C8	460	$(u_x, 0, 0)$	(w_x, w_y, w_z)	$(0, 1, 0)$	$[-15h, 36h]$
C9	1.38	(u_x, u_y, u_z)	(w_x, w_y, w_z)	Random	$[-15h, 36h]$
C10	1.38	$(u_x, 0, 0)$	(w_x, w_y, w_z)	$(1, 0, 0)$	$[-15h, 36h]$
C11	1.38	$(u_x, 0, 0)$	(w_x, w_y, w_z)	$(0, 1, 0)$	$[-15h, 36h]$
C12	2760	(u_x, u_y, u_z)	(w_x, w_y, w_z)	$(1, 0, 0)$	$[-5h, 36h]$
C13	1380	(u_x, u_y, u_z)	(w_x, w_y, w_z)	$(1, 0, 0)$	$[-5h, 36h]$
C14	690	(u_x, u_y, u_z)	(w_x, w_y, w_z)	$(1, 0, 0)$	$[-5h, 36h]$
C15	460	(u_x, u_y, u_z)	(w_x, w_y, w_z)	$(1, 0, 0)$	$[-5h, 36h]$

in Case 3, the fibers are reinjected with an orientation aligned with the streamwise direction (x), while in Case 4, the fibers are oriented in the upward direction (y). Case 5 follows the same reinjection approach as Case 2, but the fiber angular velocity upon reinjection is set to zero. In Cases 6 and 9, the same reinjection approach as Case 2 is used, but the fiber densities are $\rho_{\text{ref}}/3$ and $\rho_{\text{ref}}/1000 = 1.38\, kg/m^3 \approx \rho_{\text{air}}$, respectively. Similarly, Cases 7 and 10 use the same reinjection approach as Case 3, but with different fiber densities. Also Cases 8 and 11 employ the same reinjection approach as Case 4, but with different fiber densities.

Cases 12-15 are designed and analyzed to facilitate a comparative assessment between the flocculation of fibers simulated using the current fully resolved LES with the results obtained from Reynolds-averaged Navier-Stokes (RANS) with a particle dispersion model, as studied by Andrić *et al.* (55). In these simulations, the fiber region is restricted to $-5H$ to $36H$ in the x-direction. The fibers are reinjected with a direction that is aligned with the main flow direction, and their linear and angular velocities are determined from Equation 4.18 and Equation 4.21 for $k = 0$. The fiber densities in Cases 12-15 are set as $2\rho_{ref}$, ρ_{ref}, $\rho_{ref}/2$, and $\rho_{ref}/3$, respectively.

4.3.3 Fiber flocculation modelling

The phenomenon investigated in this chapter is the flow-induced ballistic flocculation considering different fiber reinjection approaches (involving variations in fiber linear velocity, angular velocity, and initial orientation) and fiber inertia, as outlined in Table 4.1. At each time step, the interactions between individual fibers and between fibers and flocs are identified, and the contacting fibers are merged to form larger flocs, as previously described. These resulting flocs are categorized as distinct species denoted by F_j, where j ranges from 1 to n reflecting the number of fibers present in each floc (F_1 is a "floc" with a single fiber). To analyze the distribution of floc species along the diffuser's length, the fiber region is divided into 320 bins (control volumes) of uniform thickness along the streamwise direction for Cases 1-11, and 128 control volumes for Cases 12-15. The mass fraction of each F_j species in a specific control volume is defined as (55)

$$\phi_i = \frac{iN_i}{\sum_{k=1}^{n} kN_k}. \tag{4.22}$$

Here, N_j represents the time-averaged number of flocs belonging to the F_j species in a particular control volume. The numerator indicates the time-averaged number of fibers present in flocs consisting of j fibers, while the denominator represents the time-averaged total number of fibers within the control volume, irrespective of floc size. The study primarily focuses on the development of the F_2 floc species along the length of the diffuser, due to the limited number of fibers involved and therefore also the limited formation of larger flocs. Additionally, the dimensionless flocculation rate of F_j can be defined as (55)

$$\phi_j{}' = \frac{d\phi_j}{dx} H, \tag{4.23}$$

where $\phi_j{}'$ represents the dimensionless rate of change of the mass fraction of F_j species with respect to the streamwise coordinate x, normalized by the diffuser height H.

4.3.4 Fiber/floc translational motion and alignment

To further explore the impact of flow parameters and fiber inertia on fiber flocculation, additional analysis of fiber trajectories, fibers slip velocity, the alignment of fibers with the longitudinal axis of the diffuser and with slip velocity direction, as well as the non-uniformity of the time-averaged fiber concentration is conducted.

The alignment of the fibers is characterized by the orientation of the fiber's orientation direction ($\vec{p}$) with respect to the streamwise direction (x), and the fiber slip velocity direction. The alignment of the fiber can be quantified using the cosine function, $\cos\psi$, assuming ψ to be the angle between the fiber principal axis and the direction of interest. For example, a value of $|\cos\psi_i| \approx 1$ indicates perfect alignment (parallel) while $\cos(\psi_i) = 0$ indicates perfect non-alignment (perpendicular) to the direction of interest. Moreover, to analyze the alignment trends of fibers, the probability density function (PDF) of the cosine function $\cos\psi$ is used. The PDF is computed using $f(\phi) = N_\phi/N$, where $\phi = \xi_i$ is the ith variable of interest, N_ϕ is the number of fibers that fall within a given bin $[\phi, \phi + \Delta\phi]$ with a bin size of $\Delta\phi = (\phi_{max} - \phi_{min})/N_B$ and N_B the number of bins (116). In the present study, the straight inflow channel is divided into $N_B = 200$ control volumes. The PDF satisfies the normalization condition $\sum_{i=1}^{N_B} f(\phi_i) = 1$.

In particular, to analyze fiber alignment with the particle slip velocity direction, $\vec{u}_{slip}$, the probability density function of $\cos\theta = \vec{p} \cdot \hat{e}_{\vec{u}_{slip}}$, where θ is the so-called incidence angle, the angle between the particle principal axis ($\vec{p}$) and the slip velocity direction, is monitored. Here, the slip velocity is the relative velocity between the fluid flow and the fiber ($\vec{u}_{slip} = \vec{v}_i^{\infty} - \vec{\dot{r}}_i$) and $\hat{e}_{\vec{u}_{slip}} = \vec{u}_{slip}/|\vec{u}_{slip}|$.

Moreover, the trajectories of the centers of mass of the fibers are tracked to analyze qualitatively how the fibers are transported in the diffuser and the deviation of the fiber motion paths from the main flow direction.

4.3.5 Fiber concentration

To gain an insight into how the fibers are distributed in the diffuser, the time-averaged fiber concentration of each bin (control volume), denoted as $\bar{C}$, can be used. In order to compute the local fiber concentration, the fiber region is divided into 320 bins along the flow direction, and the local concentration is calculated by dividing the number fiber segments (represented by their centers of mass) within that bin by the total number of segments in the computational domain. The non-uniformity of the time-averaged concentration can be quantified using the Preferential Concentration

Index (PCI) as defined by (65)

$$PCI = \frac{\bar{C} - \bar{C}_u}{\bar{C}_u} \tag{4.24}$$

Where $\bar{C}_u$ is the time-averaged concentration in each bin corresponding to a completely uniform distribution of fibers throughout the domain.

4.4 Results and discussion

4.4.1 Validation of fluid flow

To validate the fluid flow model utilized in this study, the axial mean velocity and axial Reynolds stress profiles obtained from fully developed simulations are compared to experimental measurements from Buice and Eaton (131) and Obi *et al.* (130). The axial and vertical positions are normalized by the upstream channel height, H, while the velocity profiles are normalized by the bulk velocity, U_b, and the axial Reynolds stresses are normalized by U_b^2. Figure 4.3 shows that the time-averaged streamwise velocity (u_x) profiles of the present LES result accurately agree with the experimental results at all axial locations. Figure 4.3 also compares the numerical and experimental evolutions of the Reynolds stress $\langle u'u' \rangle$ throughout the diffuser. In general, the LES result tends to slightly underestimate $\langle u'u' \rangle$ at most locations, but the profiles are similarly shaped as the experimental data. As proposed by Kaltenbach *et al.* (135), these discrepancies could be attributed to higher experimental errors in turbulent stresses compared to mean flow velocities, especially in regions where measurement volumes are relatively large relative to the local gradients of turbulent stresses. Nevertheless, the authors are confident that the current highly resolved LES and dynamic modeling of the SGS term provide a sufficiently accurate representation of the flow field for investigating fiber motion and floc development in the present study.

4.4.2 Particle phase

Figure 4.4 illustrates the evolution of the mass fraction ϕ_2 of floc species F_2 along the length of the diffuser for different reinjection approaches of reference fibers with a density of $\rho = 1380\, kg/m^3$. It should be recalled that the fibers are reinjected at $x =$

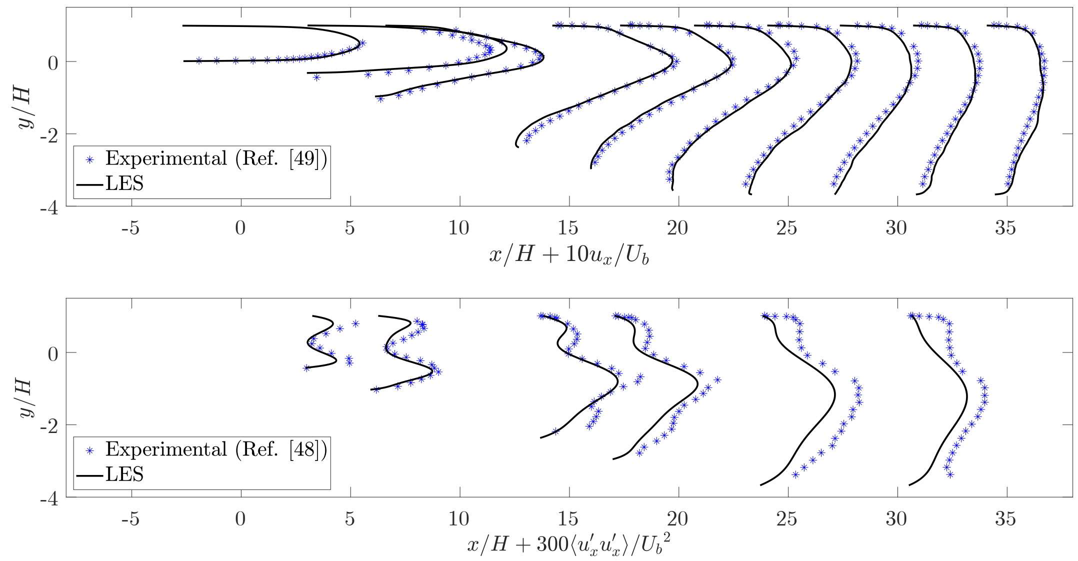

FIGURE 4.3: Development of a) axial velocity profile and b) Reynolds stress $\langle u'u' \rangle$ through the diffuser for the present LES study compared with experimental results of Obi *et al.* (130) and Buice & Eaton (131)

$-15H$ and that the fully developed flow in the straight inlet channel section ($-15 < x/H < 0$) fluctuates about a mean flow that is aligned with the channel. Under these conditions, the initial flocculation rate should be approximately constant. However, Figure 4.4 shows that there is a significant difference in flocculation rate between the different cases just after they are injected. Case 1, where the reintroduced fibers are given the same linear and angular velocities as the local instantaneous flow field, and a random orientation, exhibits the highest initial flocculation rate. For the rest of the cases (*i.e.,* Case 2-5), where the time-averaged fluid velocity field is used to calculate the linear reinjection velocity and only the streamwise component is taken into account, a lower flocculation rate is observed. By comparing Case 2 with Case 3, where the fibers are reinjected aligned with the flow direction, it can be concluded that the fiber orientation upon reinjection impacts the formation of flocs along the inlet horizontal channel up to the end of the diffuser section.

With regard to the development of mass fraction ϕ_2 of Cases 2-5, four regimes can be identified (see Figure 4.4). The first begins at the fiber reinjection plane $x/H = -15$ and ends at $x/H \approx -7$ in the straight inlet channel, in which the mass fraction ϕ_2 increases approximately linearly, *i.e.,* the fibers flocculate at a nearly constant rate. The second flocculation regime can be identified in the region $-7 < x/H < 5$ where it seems that fiber flocculation has reached somewhat a "*saturation*" level and the rate

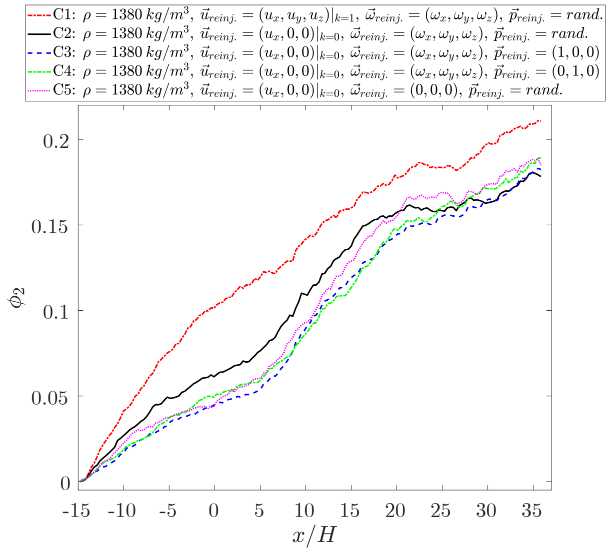

FIGURE 4.4: Development of the mass fraction ϕ_2 of floc species F_2 along the diffuser length for different fiber reinjection approaches

of flocculation has decreased. A sharp increase in the flocculation rate can be seen in the diffuser section from $x/H \approx 5$ to $x/H \approx 19$. This is due to the ballistic deflection of the fibers as reported in (53). As the mean flow velocity decreases through the diffuser section, the velocity gradient in the flow direction and the inertia of the fibers contribute to a velocity difference between the fibers and the flow, in which this relative velocity combined with the oriented hydrodynamic resistance tensor leads to a significant deviation of fiber trajectories from the streamlines of the flow (55). This phenomenon substantially increases fiber-fiber collisions and thus elevates the flocculation rate. The fiber flocculation downstream $x/H = 5$ indicates another regime in which the flocculation rate has relatively stabilized and is in a steady state. An interesting observation is that downstream of $x/H = 5$, a similar flocculation rate can be seen for Cases 2-5 (in Figure 4.4, they represent roughly the same flocculation rate in the two distinct regions of $7 < x/H < 19$, and $19 < x/H < 36$). This observation implies that the main mechanism driving the flocculation process is the ballistic deflection of fibers, regardless of the kinematics of the reinjected fibers at the inlet plane.

Figure 4.5 extends the parametric study with two additional fiber densities of $\rho_{ref}/3$ and $\rho_{ref}/1000$ (approximately equal to the density of the carrier fluid, air), and different reinjection approaches for those fibers. Case 2 is included in the graph to facilitate comparisons with the cases shown in Figure 4.4. The results show that

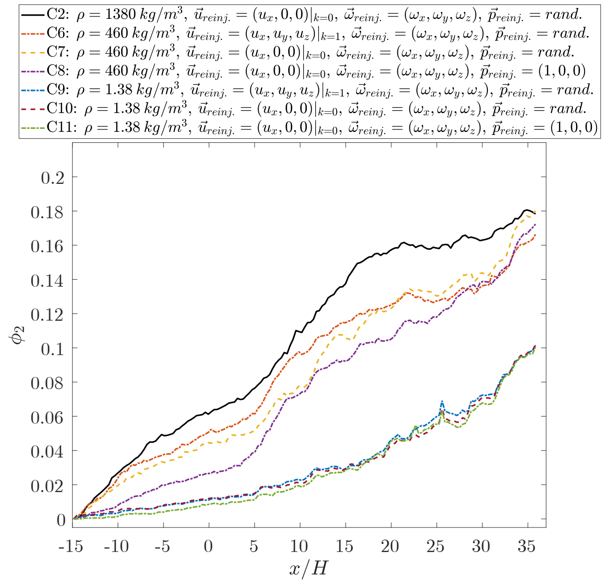

FIGURE 4.5: Development of the mass fraction ϕ_2 of floc species F_2 along the diffuser length for different fiber reinjection approaches and fiber inertia

the floc formation is more pronounced for heavier fibers. Lighter fibers, which have shorter response times, tend to align more with the flow, resulting in less deviation of fiber trajectories from the flow streamlines and lower fiber slip velocity. Consequently, they exhibit lower floc formation. This observation is particularly evident for fibers located within the straight inlet duct and at the beginning of the diffuser region. As can be seen in Figure 4.5, fiber suspensions containing lighter fibers (Case 9-11) show a significantly lower flocculation rate and mass fraction ϕ_2 compared to the heavier fibers with a density of $\rho = 460\,kg/m^3$. While random fiber reinjection orientation promotes floc formation for both cases of fiber inertia (as also observed for the reference inertia in Figure 4.4), comparisons between Cases 6 and 8 versus Cases 9 and 11 respectively suggest that the impact of reinjection approach is more noticeable for the heavier fibers. A similar trend as for Cases 2-5 regarding the development of floc formation along the diffuser is also applicable to fibers with a density of $\rho = 460\,kg/m^3$ except at the far downstream location $x/H \geq 30$, where the flocculation rate is higher for fibers with a density of $\rho_{ref}/3$. Moreover, comparing Case 11 with Case 3 reveals that the diffuser has a more significant effect on the flocculation rate for fibers with lower inertia.

Figure 4.6 shows the *relative* trajectories of the centers of mass of 200 fibers from Cases 1-3, and 10. All trajectories are moved to start at $x = -15H$ and $y = 0$,

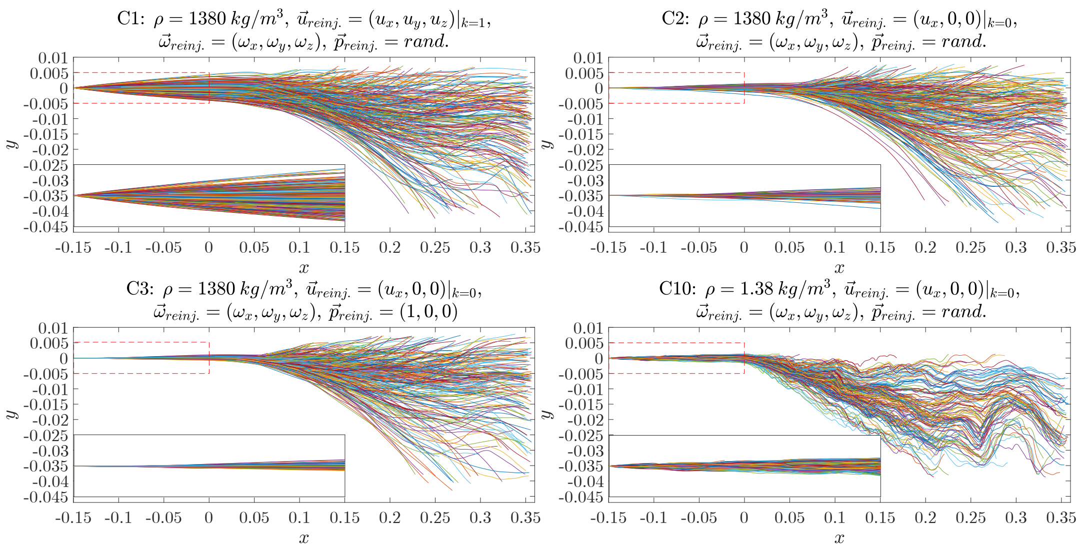

FIGURE 4.6: Relative trajectories of fibers of Cases 1-3 and 10. Each line represents the trajectory of a single fiber throughout one cycle. Colors are only used to distinguish different trajectories.

to visualize their relative deviation from the x-direction. Different colors are used for visualization purposes without carrying any specific information. A zoomed-in view, magnified by a factor of 2, is included at the bottom left corner of each plot, focusing on the straight inlet channel ($-15 < x/H < 0$). Some trajectories are truncated as the fibers hit the upper or lower wall. Those fibers and the fibers that reach the outlet are reinjected at the inlet according to the respective reinjection approach.

The zoomed-in views of Figure 4.6 show that the fibers with high inertia (Cases 1-3) follow straight trajectories, while the short response time of the light fibers of Case 10 causes the fibers to follow the resolved fluctuations of the flow. Comparing Cases 1-3, it can be seen that the choise of reinjection approach significantly affects the initial trajectories. The difference between Case 1 and Case 2 is the reinjection velocity. Case 1 gives the fibers the same velocity as the *resolved* flow at the fiber center of gravity. Case 2 gives the fibers a velocity only in the x-direction, with the value given by the *time-averaged* flow at the fiber center of gravity. Fibers with high inertia tends to keep its velocity. Thus, Case 1 yields an immediate dispersion of the fibers at reinjection, while the fibers of Case 2 start to deviate from the x-direction later. If the random orientation happens to align with the reinjection velocity vector, the fibers may dart a far distance based on only the injection approach. This can be seen when comparing Cases 2 and 3. The dispersion in Case 3 is lower since the orientation is aligned with the reinjection velocity. None of the presently used reinjection approaches are exact, which is why the reinjection plane is located far upstream to reach a fully developed flocculation rate before the inlet of the diffuser.

Considering that the flow within the straight inflow channel is predominantly aligned with the x-direction, any deviation of fiber trajectories from this direction could potentially elevate the fiber-fiber collisions. Therefore, Case 1, which demonstrates the highest deviation from the x-direction, also exhibits the highest flocculation rate and mass fraction ϕ_2 within the inlet channel. With a spatial lag from the diffuser entrance plane, the fibers perceive the influence of the decelerating flow and start to diffuse notably. This phenomenon coincides with a sharp increase in the flocculation rate around $x/H \approx 5$ (see Figure 4.4).

Figure 4.7 shows the magnitude of the average fiber slip velocity normalized by the fluid bulk velocity (U_b) along the length of the diffuser. The findings reveal a strong correlation between the fiber slip velocity and their inertia. The lightest fibers investigated ($\rho = 1.38\, kg/m^3$) exhibit a consistently very low ratio of $|\vec{u}_{slip}|/U_b$ throughout the diffuser, regardless of their reinjection kinematics. The other curves are grouped according to the fiber density.

As depicted in Figure 4.7, the fibers in Cases 1-9 demonstrate a similar evolution trend, again dependent on their inertia with no significant influence from their inlet kinematics. Upon reinjection, the fibers quickly develop a relative velocity with respect to the carrying fluid. A sharp increase in the magnitude of the relative velocity between the fibers and fluid is observed at $x/H = 2$. In Case 2, this magnitude rises rapidly from $0.06U_b$ at $x/H = 2$ to a maximum of $0.56U_b$ at $x/H = 6$, while in Case 1, it increases from $0.08U_b$ at $x/H = 6$ to a peak of $0.79U_b$ at $x/H = 6$. As explained earlier, this substantial increase in relative velocity, combined with the oriented hydrodynamic resistance tensor, constitutes the primary mechanism contributing to fiber flocculation in the diffuser (53). For cases containing fibers with moderate inertia ($\rho = 460\, kg/m^3$) in Cases 6-8, the magnitude of the fiber slip velocity generally decreases from $x/H = 6$ to the end of the diffuser section at $x/H = 21$, except a peak that appears at $x/H = 11$, after which downstream the slip velocity remains constant at $0.6U_b$. This can be attributed to the fact that fibers, after undergoing a

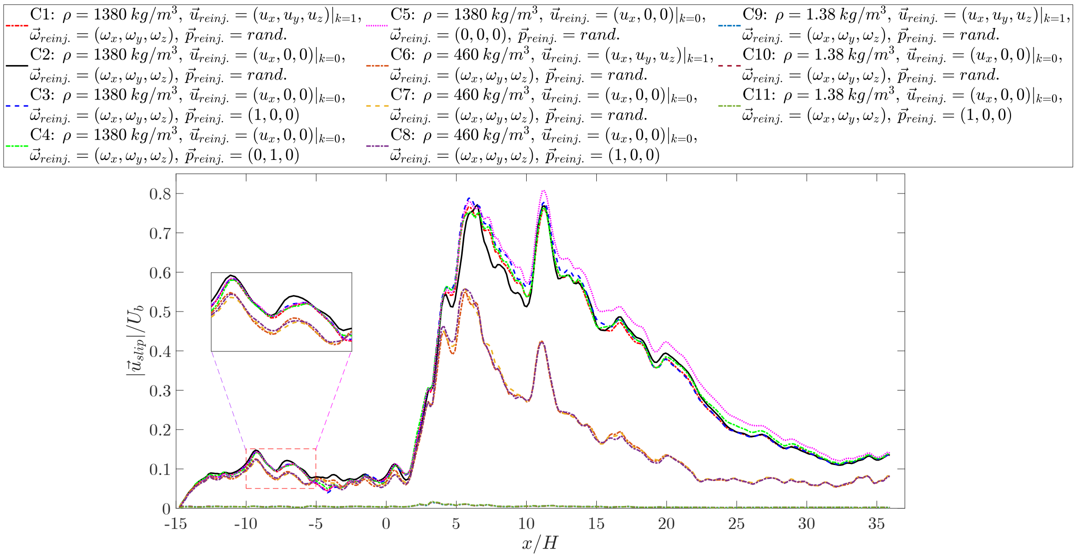

FIGURE 4.7: Magnitude of average fiber slip velocity normalized by the fluid bulk velocity (U_b) along the length of the diffuser

ballistic deflection, make a transition into the viscosity-dominated regime of motion where their velocity approaches that of the flow. A similar phenomenon is observed for fibers with higher inertia, but the stabilization of fiber slip velocity occurs further downstream.

The alignment of the fibers with the x-axis is studied in Figure 4.8. Panel A illustrates the development of fiber orientation, here formulated as the absolute value of the $\cos\alpha$ where α represents the angle between the axis of the fiber and the streamwise direction (x). Panel B presents the probability density function (PDF) of the direction cosine. It is crucial to highlight that the statistics presented in panel B are sampled exclusively from fibers traveling within the inlet channel ($-15 < x/H < 0$) with the aim of gaining deeper insights into the influence of the reinjection orientation on the floc formation.

Examining panel A of Figure 4.8, it can be seen that regardless of fiber inertia and reinjection kinematics, the ensemble averaged orientation of fibers relative to the diffuser's streamwise direction converges to approximately $|\cos\alpha| = 0.6$ at the end of the diffuser. This value could be indicative of an average orientation resulting from a random distribution of fiber orientations induced by turbulence, which tends to randomize the orientation of the fibers. Furthermore, it is evident that heavier fibers undergo less orientation change, as indicated by the smoother curves, compared to lighter fibers. This suggests that the inertia of the fibers influences the time scales of

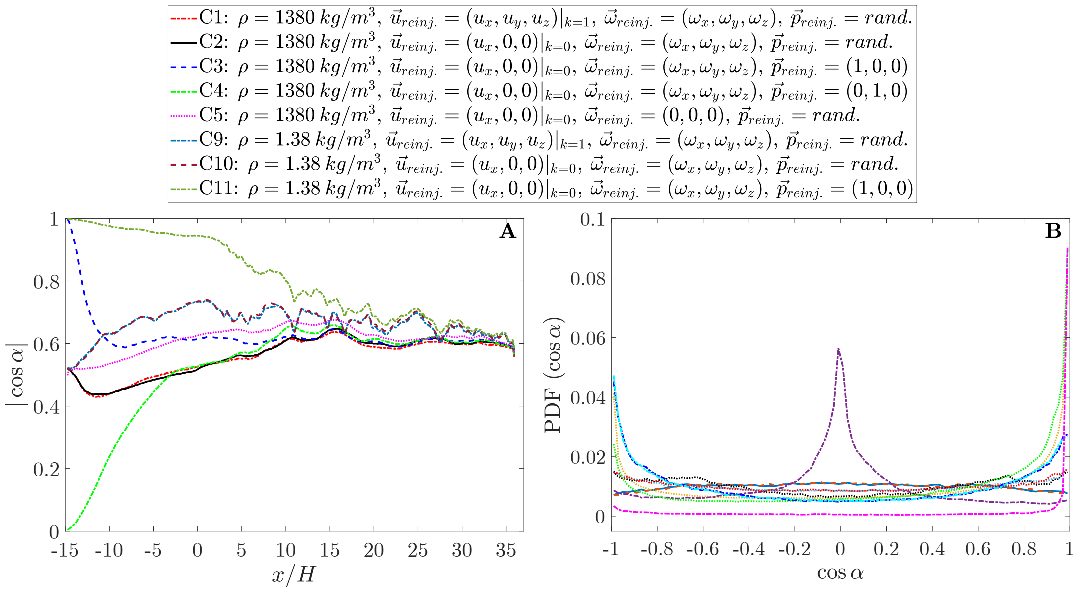

FIGURE 4.8: a) Development of the average direction cosine of the angle α between the fiber principal axis ($\vec{p}$) and the global x-axis along the diffuser length, b) Probability density function of the direction cosine, PDF($\cos\alpha$) of the angle α between the fiber principal axis and the x-axis for fibers traveling within the inlet channel $-15 < x/H < 0$

fiber reorientation. Comparing Case 1 with Case 2 for light fibers with a density of $\rho = 1.38\,kg/m^3$, as well as Case 9 with Case 10 for reference fibers ($\rho = 1380\,kg/m^3$), it can be observed that the linear velocity has a negligible impact on the alignment of fibers with respect to the x-axis while varying reinjection angular velocity affects the evolution of fiber orientation (see Case 5). Moving to panel A of Figure 4.8, it can be found that fibers with low inertia reinjected to the diffuser while initially aligned along the x-axis and are only given linear velocity in the streamwise direction (*i.e.*, Case 11), maintain their orientation relatively well until the beginning of the diffuser region at $x/H \approx 4$. In contrast, heavier fibers ($\rho = 1380\,kg/m^3$) subjected to a similar reinjection approach (Case 3) experience a rapid change in their orientation.

In panel B of Figure 4.8, the probability density function (PDF) of the direction cosine ($\cos\alpha$) in the straight inlet channel reveals distinct patterns for different cases. In Case 11, where low-inertia fibers are reinjected with an initial alignment along the streamwise direction, the PDF exhibits a peak at $\cos\alpha \approx 1$, indicating a strong alignment of the fibers with the streamwise direction. Similarly, Case 3, which involves reference fibers reintroduced using the same approach as Case 11, shows two peaks at $\cos\alpha \approx -1$ and $\cos\alpha \approx 1$, representing a highly parallel alignment with the main flow direction. In Case 4, where the assigned fiber orientation at the inlet plane is

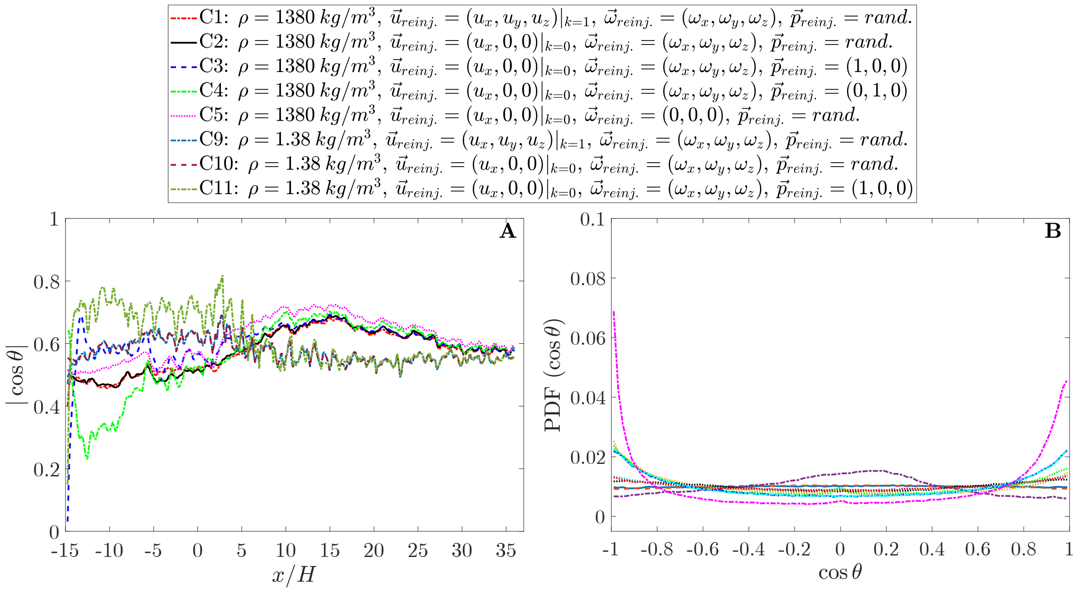

FIGURE 4.9: a) Development of the average direction cosine of the angle θ between the fiber principal axis ($\vec{p}$) and the fiber slip velocity direction along the diffuser length, b) Probability density function of the direction cosine, PDF($\cos\theta$) of the angle θ between the fiber principal axis and fiber slip velocity direction for fibers traveling within the inlet channel $-15 < x/H < 0$

perpendicular to the streamwise direction, the PDF shows a peak at $\cos\alpha \approx 0$, indicating a strong preferential alignment perpendicular to the streamwise direction. For the cases involving reference fibers where the fiber orientation is randomly set upon reinjection (Cases 1, 2, and 5), the PDF of $\cos\alpha$ displays a flat profile with a relatively constant value, varying by approximately 3% This suggests that the orientation remains random, and no clear preferential alignment with respect to the streamwise direction is observed in the inflow channel. However, in the case of light fibers that are reinjected with random orientations (*i.e.*, Case 10 and 11), the PDF of $\cos\alpha$ exhibits three extrema: a minimum at $\cos\alpha = 0$ and two maxima at $\cos\alpha = -1$ and $\cos\alpha = 1$. This indicates that fast-responsive fibers with lower inertia tend to align with the flow direction as they travel through the horizontal inlet channel. These observations are in line with the findings from Figures 4.4 and Figure 4.6, where the trajectories and floc formations of the fibers were suggested to be influenced by the development of fiber orientation.

In panel A of Figure 4.9, the development of the absolute value of $\cos\theta$ is shown, where θ is the angle between the fiber principal axis ($\vec{p}$) and the slip velocity direction $\hat{e}_{\vec{u}_{slip}} = (\vec{v}_i^{\infty} - \dot{\vec{r}}_i)/|\vec{v}_i^{\infty} - \dot{\vec{r}}_i|$. A comparison between Cases 2, 3, and 4, as well as Cases 10 and 11, reveals that the initial orientation of the fibers upon reinjection significantly affects the evolution of $|\cos\theta|$ up to the beginning of the diffuser section at $x/H \approx 5$. However, as the fibers move forward it becomes apparent that their orientation is mainly influenced by their inertia and the decelerating flow field within the diffuser. Downstream $x/H = 26$, all fibers exhibit a similar value of $|\cos\theta| \approx 0.6$, regardless of their inertia and reinjection kinematics. Furthermore, it is observed that heavier fibers undergo less orientation change compared to lighter particles, indicating the significant role of fiber inertia in governing the time scales of fiber reorientation.

Panel B of Figure 4.9 presents the probability density function (PDF) of the cosine of the incidence angle. It is important to note that the reported results are obtained only from fibers flowing in the inflow region ($15 < x/H < 0$). Since the flow in this region is approximately uniform and aligned with the main flow direction, panel B of Figure 4.9 exhibits similar characteristics and conveys nearly identical information as panel B of Figure 4.8. Notably, for Case 4 in panel B of Figure 4.9, a strong peak is observed in the PDF at $\cos\theta = 0$, indicating a strong alignment to the direction perpendicular to the flow. In contrast, the peaks in panel B of Figure 4.9 are flattened and shifted to $\cos\theta = 0.15$, indicating a lesser degree of alignment between $\vec{p}$ and $\vec{u}_{slip}/|\vec{u}_{slip}|$.

The non-uniformity of fiber concentration along the length of the diffuser is investigated using the Preferential Concentration Index (PCI), as defined by Equation 4.24). Figure 4.10 reveals three distinct regimes that align with the different sections of the diffuser. Region $-15 < x/H < 0$ corresponds to the straight inflow channel. Region $0 < x/H < 21$ is associated with the diffuser. The region downstream $x/H = 21$ represents the outflow channel. A main cause of the variation is that the data is influenced by the varying areas of the bins within each section of the diffuser. For a constant flow of fibers, the inlet channel exhibits a higher PCI due to the smaller bins, while the outlet channel section demonstrates lower PCI values due to the larger bins. Figure 4.10 particularly shows that slower-responsive fibers with larger inertia exhibit higher values of PCI than lighter fast-responsive fibers in the inlet region, which is slightly affected by the fiber reinjection approaches. However, the effect of fiber inertia gradually diminishes as fibers travel through the diffuser

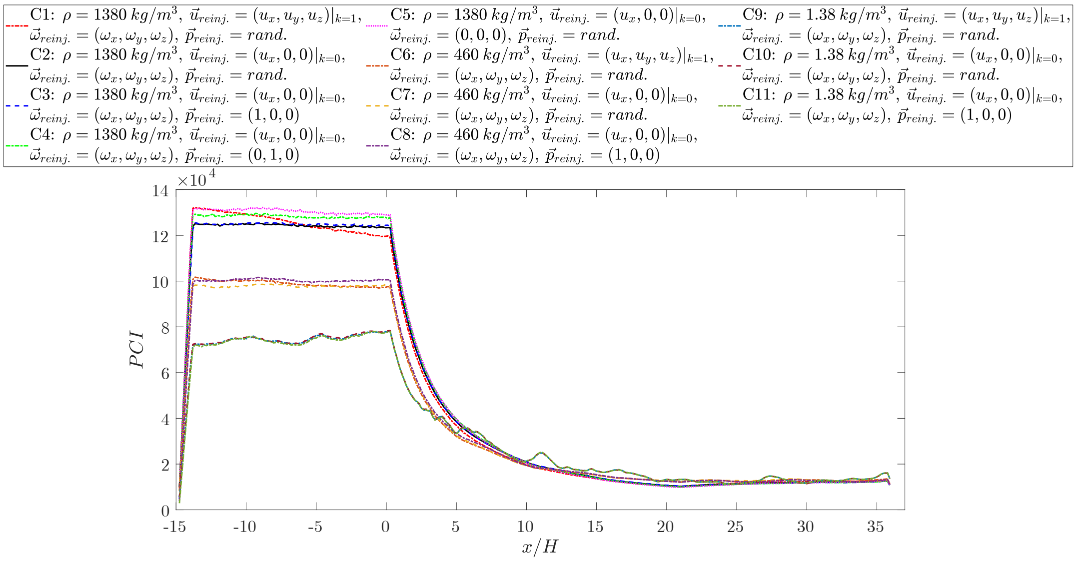

FIGURE 4.10: Development of Preferential Concentration Index (PCI) along the length of the diffuser

section, and all fibers, regardless of their inertia and reinjection kinematics, converge to the same PCI value of 1.3×10^4.

Figure 4.11 provides a comparison of the development of the mass fraction ϕ_2 of floc species F_2 along the length of the diffuser between the present fully resolved LES simulations and RANS simulations using a standard $k - \omega$ turbulence model and a particle dispersion model, as reported in by Andrić et al. (55). The reinjection plane is here located at $x/H = -5$, as in the work by Andrić et al. In all these simulations, the fibers are reinjected aligned with the x-direction, while the fiber density is varied to alter the inertia. The results in Figure 4.11 demonstrate that flocculation begins before the diffuser in all LES cases, while only small amounts of flocs are formed in the RANS cases. This observation can be attributed to the fact that in highly resolved LES the fibers continuously experience accelerating and decelerating flow that may induce ballistic deflection already in the inflow channel $-5 < x/H < 0$. An increase in the flocculation rate can be observed at $x/H \approx 5$ for all instances of fiber inertia in both RANS and LES simulations. However, the intensity of flocculation is higher in the RANS cases, with the highest intensity observed for the case with reference inertia. In all RANS and LES instances, it can be seen that as inertia increases, the degree of flocculation also increases.

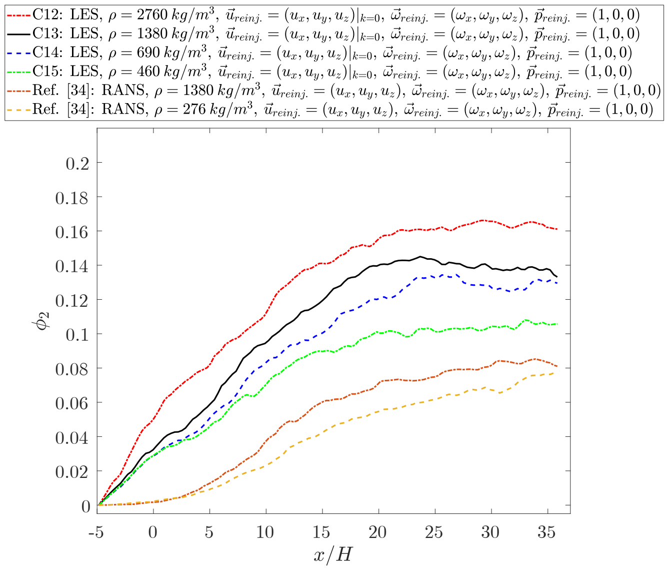

FIGURE 4.11: Influence of dispersion in fully resolved LES versus RANS dispersion model on the mass fraction ϕ_2

4.5 Conclusions

The present chapter examined the flocculation behavior of rigid fibers suspended in the flow inside a diffuser, focusing on the impact of fiber reinjection kinematics and fiber inertia. The motion of the fibers was simulated numerically using the rod-chain model for rigid fibers as adopted by Lindström and Uesaka (46) and Andrić *et al.* (56). Large Eddy Simulation (LES) was used to directly resolve the details of the flow and the fiber-flow interaction. Additionally, short-range attractive forces were considered between fibers which cause them to form flocs.

The analysis of the mass fraction of flocs with two fibers, denoted as ϕ_2, provided insights into the flocculation behavior and revealed the presence of four distinct flocculation regimes, each exhibiting different flocculation rates. A sharp increase in the fiber slip velocity was observed in the initial section of the diffuser which in combination with the oriented hydrodynamic resistance tensor, generates significant ballistic deflection of fibers. This phenomenon consequently increases the fiber-fiber collisions and thus increases the fiber flocculation, and it should be considered as the main mechanism governing the flocculation in the diffuser.

When fibers are reinjected with random orientations and their linear velocity components are computed from a three-dimensional instantaneous flow field, the highest degree of fiber flocculation is observed in the straight inflow channel. However, if a time-averaged fluid velocity field is considered and the linear velocity of fibers has only the streamwise component, the degree of flocculation decreases. A further decrease in flocculation is observed when the fibers are oriented along the flow direction upon reinjection. These findings highlight the significance of the reinjection approach in determining the behavior of fiber flocculation.

This study also investigated the influence of fiber inertia on flocculation behavior and it was found that fibers with higher density exhibited a greater tendency to form flocs. On the other hand, lighter fibers exhibited a higher degree of alignment with the flow streamlines, demonstrated smaller fiber slip velocities, and consequently experienced less collision with other fibers resulting in a lower floc formation. Furthermore, the impact of the reinjection approach on flocculation behavior was more pronounced for heavier fibers. This suggests that the interplay between fiber properties and the reinjection kinematics of the fibers influences the formation and growth of flocs.

Furthermore, a fiber alignment analysis revealed that the orientation of fibers with respect to the diffuser streamwise direction converged to a common value at the end of the outlet duct, regardless of fiber inertia and reinjection kinematics, highlighting the effect of turbulence that tends to randomize the orientation of the fiber. It was also shown that heavier fibers showed less orientation change compared to lighter fibers, indicating that inertia influenced the time scales of fiber reorientation.

The analysis of fiber alignment in the diffuser revealed some important observations. Firstly, regardless of fiber inertia and reinjection kinematics, the orientation of fibers with respect to the diffuser streamwise direction converged to a common value at the end of the outlet duct. This suggests that the turbulent flow in the diffuser tends to randomize the orientation of the fibers, leading to a relatively consistent average orientation at the end part of the outflow channel. Secondly, it was observed that heavier fibers exhibited less orientation change compared to lighter fibers due to their greater momentum and resistance to changes in motion. This implies that the inertia of the fibers influences the time scales of fiber reorientation.

The comparison between the fiber flocculation behavior of fully resolved LES simulations with previous RANS simulations using a standard $k-\omega$ turbulence model sheds light on the influence of turbulence and dispersion modeling on fiber flocculation. The findings indicate that the LES simulations consistently exhibit a higher degree of flocculation compared to the RANS simulations. Additionally, flocculation is observed to initiate at an earlier stage in the LES cases, even before entering the diffuser, while only a small amount of flocs is formed in the RANS cases. This difference might be attributed to the more accurate representation of flow dynamics in the LES simulations. The fibers in the LES simulations experience the full range of accelerating and decelerating flow phenomena, which may induce ballistic deflection of the fibers even in the inflow channel. This continuous interaction with the fluctuating flow field enhances fiber-fiber collisions and promotes floc formation.

This study has provided some insights into the flocculation of rigid fibers in an asymmetric diffuser. However, it is important to acknowledge its major limitations and the need for further investigations. Specifically, this study assumed a fixed fiber length, which restricts our understanding of the influence of varying fiber lengths on flocculation behavior. Additionally, the analysis focused primarily on attractive forces, overlooking the contributions of other forces such as friction and repulsive forces. Moreover, the study only considered dilute suspensions, neglecting the behavior of semi-dilute suspensions. Addressing these limitations will lead to a more comprehensive understanding of fiber flocculation dynamics and enable the development of improved strategies for controlling and manipulating fiber suspensions in practical applications.

Appendix A

Fiber model breakdown

The following appendix presents in-depth details of the general form of the fiber's equations of motion, hydrodynamic forces and torques, discretized equations of motion, and the numerical algorithms used to solve the equations. These details are primarily drawn from the work of Andrić et al. (56) for the flexible fiber model, and Andrić et al. (53) for the rigid fiber model. For a more comprehensive understanding, readers should refer to these references.

A.1 Flexible fiber model

A.1.1 Equations of motion

The equations governing the motion of each fiber segment i are derived from Euler's first and second laws, as presented in the references (46) and (45). The forces exerted on a fiber segment denoted as i with mass m_i, length l_i, and diameter D, include hydrodynamic forces ($\vec{F}_i^h$), the sum of body force ($\vec{F}_i^b$), and the connectivity forces ($\vec{X}_i$) that act between neighboring fiber segments and maintains the integrity of the fiber and ensures its length remains constant. The force balance yields:

$$m_i \ddot{\vec{r}}_i = \vec{F}_i^h + \vec{F}_i^b + \vec{X}_{i+1} - \vec{X}_i \tag{A.1}$$

The torque balance on fiber segment i involves analogous components, as well as the restorative torque:

$$\frac{\partial}{\partial t}\left(\bar{\bar{I}}_i \cdot \vec{\omega}\right) = \vec{T}_i^h + \vec{Y}_{i+1} - \vec{Y}_i + \left(\frac{l}{2}\vec{p}_i\right) \times \left(\vec{X}_{i+1}\right) + \left(\frac{-l}{2}\vec{p}_i\right) \times \left(-\vec{X}_i\right) \tag{A.2}$$

Here, $\bar{\bar{I}}_i$ represents the inertia tensor of segment i relative to the global coordinate system, $\vec{\omega}_i$ signifies the angular velocity, $\vec{T}_i^h$ denotes the hydrodynamic torque, and $\vec{Y}_i$ encompasses the sum of bending and twisting torques applied to segment $i-1$ by segment i. In Equations (A.1) and (A.2), for the end segments, $\vec{X}_1 = \vec{X}_{N_{seg}+1} = \vec{0}$, as well as $\vec{Y}_1 = \vec{Y}_{N_{seg}+1} = \vec{0}$.

The constraint that keeps a fiber at a constant length requires that the endpoints of adjacent fiber segments coincide, (*i.e.*,

$$\vec{r}_i + \frac{l}{2}\vec{p}_i - \left(\vec{r}_{i+1} - \frac{l}{2}\vec{p}_{i+1}\right) = \vec{0} \tag{A.3}$$

And taking the time derivative leads to:

$$\dot{\vec{r}}_i - \dot{\vec{r}}_{i+1} = \frac{l}{2}\vec{\omega}_i \times \vec{p}_i + \frac{l}{2}\vec{\omega}_{i+1} \times (-\vec{p}_{i+1}) \tag{A.4}$$

A.1.2 Hydrodynamic forces and torques

The hydrodynamic forces and torques are developed due to the velocity difference between the fiber segment and the surrounding fluid medium. According to Lindström and Uesaka (46), the hydrodynamic force ($\vec{F}_i^h$) and hydrodynamic torque ($\vec{T}_i^h$) can be approximated as a sum of the viscous ($Re \ll 1$) and the dynamic drag ($Re \gg 1$) contributions, *i.e.*

$$\vec{F}_i = \vec{F}_i^V + \vec{F}_i^I, \tag{A.5}$$

$$\vec{T}_i = \vec{T}_i^V + \vec{T}_i^I. \tag{A.6}$$

Here the viscous drag force $\vec{F}_i^V$ and torque $\vec{T}_i^V$ on each cylindrical segment are approximated as those acting on an isolated equivalent prolate spheroid of aspect ratio $r_e = 1.24 r_f \big/ \sqrt{\ln r_f}$ through

$$\vec{F}_i^V = \bar{\bar{A}}_i^V \cdot \left(\vec{v}_i^\infty - \dot{\vec{r}}_i\right) \tag{A.7}$$

$$\vec{T}_i^V = \bar{\bar{C}}_i^V \cdot \left(\vec{\Omega}_i^\infty - \vec{\omega}_i\right) + \bar{\bar{\bar{H}}}_i^V : \bar{\bar{E}}_i^\infty \tag{A.8}$$

Here $\vec{v}_i^\infty$, $\vec{\Omega}_i^\infty = \frac{1}{2}\left(\nabla \times \vec{v}_i^\infty\right)$, $\bar{\bar{E}}^\infty = \frac{1}{2}\left(\nabla\vec{v}_i^\infty + \left(\nabla\vec{v}_i^\infty\right)^t\right)$ are the translational fluid velocity, the angular fluid velocity and the rate of the strain tensor, respectively, all evaluated at the center of mass of segment i. Moreover, $\bar{\bar{A}}_i^V$, $\bar{\bar{C}}_i^V$, and $\bar{\bar{H}}_i^V$ are the resistance tensors that are approximated by the corresponding resistance tensors of a prolate spheroid with an equivalent aspect ratio proposed by Kim and Karrila (128) as

$$\bar{\bar{A}}_i^V = 3\pi\eta l_i \left[Y_i^A \bar{\bar{\delta}} + \left(X_i^A - Y_i^A \right) \vec{p}_i \vec{p}_i \right] \tag{A.9}$$

$$\bar{\bar{C}}_i^V = \pi\eta l_i^3 \left[Y_i^C \bar{\bar{\delta}} + \left(X_i^C - Y_i^C \right) \vec{p}_i \vec{p}_i \right] \tag{A.10}$$

$$\bar{\bar{H}}_i^V = -\pi\eta l_i^3 Y_i^H \left(\bar{\bar{\epsilon}} \cdot \vec{p}_i \right) \vec{p}_i \tag{A.11}$$

where $\bar{\bar{\delta}}$ and $\bar{\bar{\epsilon}}$ represent the unit and permutation tensor, respectively. The parameters X_i^A, Y_i^A, X_i^C, Y_i^C, and Y_i^H are hydrodynamic coefficients that rely on the eccentricity denoted as $e_i = (1 - b_i^2/a_i^2)^{1/2}$, and are defined as (128):

$$\begin{aligned}
L(e_i) &= \ln \frac{1+e_i}{1-e_i} \\
X_i^A(e_i) &= \frac{8}{3} e_i^3 \left[-2e_i + \left(1+e_i^2\right) L(e_i) \right]^{-1} \\
Y_i^A(e_i) &= \frac{16}{3} e_i^3 \left[2e_i + \left(3e_i^2 - 1\right) L(e_i) \right]^{-1} \\
X_i^C(e_i) &= \frac{4}{3} e_i^3 \left(1-e_i^2\right) \left[2e_i - \left(1-e_i^2\right) L(e_i) \right]^{-1} \\
Y_i^C(e_i) &= \frac{4}{3} e_i^3 \left(2-e_i^2\right) \left[-2e_i - \left(1+e_i^2\right) L(e_i) \right]^{-1} \\
Y_i^H(e_i) &= \frac{4}{3} e_i^5 \left[-2e_i + \left(1+e_i^2\right) L(e_i) \right]^{-1}.
\end{aligned} \tag{A.12}$$

For the segment Reynolds number in the range of $10^2 \leq \mathrm{Re}_s \leq 3 \times 10^5$, the drag force exerted by the cross-flow on a cylinder dominates over the viscous drag in the axial direction, and only the flow components in the plane perpendicular to $\vec{p}_i$ need to be considered. According to Tritton (136), The drag coefficient for cross flow over a circular cylinder is $C_D^I = 1$ for $10^2 \leq \mathrm{Re}_s \leq 3 \times 10^5$. Integration over infinitesimal cylinder slices is employed to determine the total drag force and torque on a cylindrical fiber segment. Subsequently, the resulting dynamic drag force and torque are as (46):

$$\vec{F}_i^I = \bar{\bar{A}}_i^I \cdot \left(\vec{v}_i^\infty - \dot{\vec{r}}_i \right) \tag{A.13}$$

$$\vec{T}_i^I = \bar{\bar{C}}_i^I \cdot \left(\vec{\Omega}_i^\infty - \vec{\omega}_i \right) + \bar{\bar{H}}_i^I : \bar{\bar{E}}_i^\infty \tag{A.14}$$

Here, the dynamic drag resistance tensors of $\bar{\bar{A}}_i^I$, $\bar{\bar{C}}_i^I$, $\bar{\bar{H}}_i^I$ are determined as:

$$\begin{aligned}
\bar{\bar{A}}_i^I &= \frac{1}{2} C_D^I \rho D_i l_i v_{\perp,i} \left[\bar{\bar{\delta}} - \vec{p}_i \vec{p}_i\right] \\
\bar{\bar{C}}_i^I &= \frac{1}{24} C_D^I \rho D_i l_i^3 v_{\perp,i} \left[\bar{\bar{\delta}} - \vec{p}_i \vec{p}_i\right] \\
\bar{\bar{H}}_i^I &= \frac{1}{24} C_D^I \rho D_i l_i^3 v_{\perp,i} \left[\left(\bar{\bar{\epsilon}} \cdot \vec{p}_i\right) \vec{p}_i\right]
\end{aligned} \tag{A.15}$$

where $v_{\perp,i} = \left| \left(\bar{\bar{\delta}} - \vec{p}_i \vec{p}_i\right) \cdot \left(\vec{v}_i^{\infty} - \dot{\vec{r}}_i\right) \right|$ denotes the cross-flow velocity of the fluid relative to the fiber segment (46).

A.1.3 Discretized fiber equations of motion

The governing equations of motion of the fiber are discretized in time using a time step represented by Δt. Subscripts $n-1$ and n correspond to the previous and current time steps, respectively. To ensure improved numerical stability, an implicit numerical approach is applied to calculate the segment velocity and angular velocity. In this section, the connectivity forces $\vec{X}_i$ and $\vec{X}_{i+1}$ are treated as unknown variables. Equation A.1 can be discretized as follows (56):

$$\frac{m}{\Delta t}\left(\dot{\vec{r}}_{i,n} - \dot{\vec{r}}_{i,n-1}\right) = \left(\bar{\bar{A}}_{i,n-1}^V + \bar{\bar{A}}_{i,n-1}^I\right) \cdot \left(\vec{v}_{i,n-1}^{\infty} - \dot{\vec{r}}_{i,n}\right) + \vec{X}_{i+1,n} - \vec{X}_{i,n} \tag{A.16}$$

In Equation A.2, the time differential term can be discretized as (56)

$$\frac{\partial}{\partial t}\left(\bar{\bar{I}}_{i,n-1} \cdot \vec{\omega}_{i,n}\right) \approx \dot{\bar{\bar{I}}}_{i,n-1} \cdot \vec{\omega}_{i,n} + \frac{1}{\Delta t} \bar{\bar{I}}_{i,n-1} \cdot \left(\vec{\omega}_{i,n} - \vec{\omega}_{i,n-1}\right) \tag{A.17}$$

Hence, Equation A.2 can be discretized as

$$\begin{aligned}
&\dot{\bar{\bar{I}}}_{i,n-1} \cdot \vec{\omega}_{i,n} + \frac{1}{\Delta t} \bar{\bar{I}}_{i,n-1} \cdot \left(\vec{\omega}_{i,n} - \vec{\omega}_{i,n-1}\right) = \left(\bar{\bar{C}}_{i,n-1}^V + \bar{\bar{C}}_{i,n-1}^I\right) \cdot \\
&\left(\vec{\Omega}_{i,n-1}^{\infty} - \vec{\omega}_{i,n}\right) + \left(\bar{\bar{H}}_{i,n-1}^V + \bar{\bar{H}}_{i,n-1}^I\right) : \bar{\bar{E}}_i^{\infty} \\
&+ \frac{l_i}{2} \vec{p}_{i,n-1} \times \left(\vec{X}_{i+1,n} - \vec{X}_{i,n}\right)
\end{aligned} \tag{A.18}$$

The connectivity constraint, Equation A.34, can be discretized as follows

$$\dot{\vec{r}}_{i+1,n} - \dot{\vec{r}}_{i,n} = \frac{l_i}{2} \vec{\omega}_{i,n} \times \vec{p}_{i,n-1} + \frac{l_{i+1}}{2} \vec{\omega}_{i+1,n} \times \vec{p}_{i+1,n-1} \tag{A.19}$$

The system of equations, including the linear momentum equation (A.16), the angular momentum equation (A.18), and the connectivity equation (A.19), can be solved to compute the unknown connectivity forces, velocities, and angular velocities at time n. Due to the diverse physical units associated with these variables, the coefficients within the linear system exhibit significant variations in magnitude, rendering the system ill-conditioned. Therefore, a system of dimensionless equations is considered (56).

The system of dimensionless equations for the unknown connectivity forces (* denotes dimensionless quantities) can be expressed as follows

$$\bar{\bar{Q}}^*_{i,n-1} \cdot \vec{X}^*_{i,n} + \bar{\bar{S}}^*_{i,n-1} \cdot \vec{X}^*_{i+1,n} + \bar{\bar{T}}^*_{i,n-1} \cdot \vec{X}^*_{i+2,n} = \vec{V}^*_{i,n-1} \tag{A.20}$$

Through the application of Tikhonov regularization, the system can be effectively solved to determine the unknown dimensionless connectivity forces $\vec{X}_{i+1,n}$, where $2 \leq i \leq N_{seg}$ while ensuring that $\vec{X}^*_{1,n} = \vec{X}^*_{N_{seg}+1,n} = \vec{0}$. As an example, in case that fiber consists of $N_{seg} = 7$ segments, the system of equations takes the following form (56):

$$\begin{bmatrix} \bar{\bar{S}}^*_{1,n-1} & \bar{\bar{T}}^*_{1,n-1} & \bar{\bar{0}} & \bar{\bar{0}} & \bar{\bar{0}} & \bar{\bar{0}} \\ \bar{\bar{Q}}^*_{2,n-1} & \bar{\bar{S}}^*_{2,n-1} & \bar{\bar{T}}^*_{2,n-1} & \bar{\bar{0}} & \bar{\bar{0}} & \bar{\bar{0}} \\ \bar{\bar{Q}}^*_{3,n-1} & \bar{\bar{S}}^*_{3,n-1} & \bar{\bar{T}}^*_{3,n-1} & \bar{\bar{0}} & \bar{\bar{0}} & \bar{\bar{0}} \\ \bar{\bar{0}} & \bar{\bar{Q}}^*_{4,n-1} & \bar{\bar{S}}^*_{4,n-1} & \bar{\bar{T}}^*_{4,n-1} & \bar{\bar{0}} & \bar{\bar{0}} \\ \bar{\bar{0}} & \bar{\bar{0}} & \bar{\bar{Q}}^*_{5,n-1} & \bar{\bar{S}}^*_{5,n-1} & \bar{\bar{T}}^*_{5,n-1} & \bar{\bar{0}} \\ \bar{\bar{0}} & \bar{\bar{0}} & \bar{\bar{0}} & \bar{\bar{Q}}^*_{6,n-1} & \bar{\bar{S}}^*_{6,n-1} & \bar{\bar{T}}^*_{6,n-1} \end{bmatrix} \cdot \begin{bmatrix} \vec{X}^*_{2,n} \\ \vec{X}^*_{3,n} \\ \vec{X}^*_{4,n} \\ \vec{X}^*_{5,n} \\ \vec{X}^*_{6,n} \\ \vec{X}^*_{7,n} \end{bmatrix} = \begin{bmatrix} \vec{V}^*_{1,n-1} \\ \vec{V}^*_{2,n-1} \\ \vec{V}^*_{3,n-1} \\ \vec{V}^*_{4,n-1} \\ \vec{V}^*_{5,n-1} \\ \vec{V}^*_{6,n-1} \end{bmatrix} \tag{A.21}$$

The dimensionless tensors emerging from the linear system of connectivity forces are expressed as:

$$\bar{\bar{Q}}^*_{i,n-1} = -\left(\frac{m^*}{\Delta t^*}\bar{\bar{\delta}} + \bar{\bar{A}}^{V*}_{i,n-1} + \bar{\bar{A}}^{I}_{i,n-1}\right)^{-1} + \frac{3}{4r_p}\bar{\bar{C}}^*_{\vec{p}_{i,n-1}}$$

$$\bar{\bar{S}}^*_{i,n-1} = \left(\frac{m^*}{\Delta t^*}\bar{\bar{\delta}} + \bar{\bar{A}}^{V}_{i,n-1} + \bar{\bar{A}}^{I}_{i,n-1}\right)^{-1} + \left(\frac{m^*}{\Delta t^*}\bar{\bar{\delta}} + \bar{\bar{A}}^{V}_{i,n-1} + \bar{\bar{A}}^{I}_{i,n-1}\right)^{-1} + \frac{3}{4r_p}\bar{\bar{C}}^*_{\vec{p}_{i,n-1}} + \frac{3}{4r_p}\bar{\bar{C}}^*_{\vec{p}_{i+1,n-1}}$$

$$\bar{\bar{T}}^*_{i,n-1} = -\left(\frac{m^*}{\Delta t^*}\bar{\bar{\delta}} + \bar{\bar{A}}^{V}_{i,n-1} + \bar{\bar{A}}^{I}_{i,n-1}\right)^{-1} + \frac{3}{4r_p}\bar{\bar{C}}^*_{\vec{p}_{i+1,n-1}}$$

$$
\begin{aligned}
\vec{V}^*_{i,n-1} &= -\left(\vec{s}^*_{i,n-1} - \vec{s}^*_{i,n-1} + r_p\left(\vec{b}^*_{i,n-1} - \vec{b}^*_{i,n-1}\right)\right)\\
\vec{s}^*_{i,n-1} &= \left(\frac{m^*}{\Delta t^*}\bar{\bar{\delta}} + \bar{\bar{A}}^V_{i,n-1} + \bar{\bar{A}}^I_{i,n-1}\right)^{-1}\cdot\left(\left(\frac{m^*}{\Delta t^*}\dot{\vec{r}}_{i,n-1} + \bar{\bar{A}}^V_{i,n-1} + \bar{\bar{A}}^I_{i,n-1}\right)\cdot\vec{v}^*_{i,n-1}\right.\\
\vec{b}^*_{i,n-1} &= \left(\left(\bar{\bar{I}}^*_{i,n-1} + \frac{1}{\Delta t^*}\bar{\bar{I}}^*_{i,n-1} + \bar{\bar{C}}^{V*}_{i,n-1} + \bar{\bar{C}}^{I*}_{i,n-1}\right)^{-1}\cdot\left(\frac{1}{\Delta t^*}\bar{\bar{I}}^*_{i,n-1}\cdot\vec{\omega}^*_{i,n-1} + \right.\right.\\
&\left.\left.\left(\bar{\bar{C}}^{V*}_{i,n-1} + \bar{\bar{C}}^{I*}_{i,n-1}\right)\cdot\vec{\Omega}^*_{i,n-1} + \left(\bar{\bar{H}}^{V*}_{i,n-1} + \bar{\bar{H}}^{I*}_{i,n-1}\right) : \bar{\bar{E}}^{I*}_{i,n-1}\right)\right)\times\vec{p}_{i,n-1}
\end{aligned}
$$

where $\bar{\bar{C}}^*_{\vec{p}_{i,n-1}}$ is a second-order tensor and its components are

$$
\begin{aligned}
C^*_{\vec{p}_i,n-1,11} &= C_{I^*_{\vec{p}_{i,n-1,22}}}\vec{p}^2_{i,n-1,3} - C_{I^*_{\vec{p}_{i,n-1,23}}}\vec{p}_{i,n-1,2}\vec{p}_{i,n-1,3} - C_{I^*_{\vec{p}_{i,n-1,32}}}\vec{p}_{i,n-1,3}\vec{p}_{i,n-1,2} +\\
&\quad C_{I^*_{\vec{p}_{i,n-1,33}}}\vec{p}^2_{i,n-1,2}\\
C^*_{\vec{p}_i,n-1,12} &= -C_{I^*_{\vec{p}_{i,n-1,21}}}\vec{p}^2_{i,n-1,3} + C_{I^*_{\vec{p}_{i,n-1,23}}}\vec{p}_{i,n-1,1}\vec{p}_{i,n-1,3} + C_{I^*_{\vec{p}_{i,n-1,31}}}\vec{p}_{i,n-1,2}\vec{p}_{i,n-1,3} -\\
&\quad C_{I^*_{\vec{p}_{i,n-1,33}}}\vec{p}_{i,n-1,1}\vec{p}_{i,n-1,2}\\
C^*_{\vec{p}_i,n-1,13} &= C_{I^*_{\vec{p}_{i,n-1,21}}}\vec{p}_{i,n-1,2}\vec{p}_{i,n-1,3} - C_{I^*_{\vec{p}_{i,n-1,22}}}\vec{p}_{i,n-1,1}\vec{p}_{i,n-1,3} - C_{I^*_{\vec{p}_{i,n-1,31}}}\vec{p}^2_{i,n-1,2} +\\
&\quad C_{I^*_{\vec{p}_{i,n-1,32}}}\vec{p}_{i,n-1,1}\vec{p}_{i,n-1,2}\\
C^*_{\vec{p}_i,n-1,21} &= C_{I^*_{\vec{p}_{i,n-1,32}}}\vec{p}_{i,n-1,3}\vec{p}_{i,n-1,1} - C_{I^*_{\vec{p}_{i,n-1,33}}}\vec{p}_{i,n-1,1}\vec{p}_{i,n-1,2} - C_{I^*_{\vec{p}_{i,n-1,12}}}\vec{p}^2_{i,n-1,3} +\\
&\quad C_{I^*_{\vec{p}_{i,n-1,13}}}\vec{p}_{i,n-1,2}\vec{p}_{i,n-1,3}\\
C^*_{\vec{p}_i,n-1,22} &= -C_{I^*_{\vec{p}_{i,n-1,31}}}\vec{p}_{i,n-1,1}\vec{p}_{i,n-1,3} + C_{I^*_{\vec{p}_{i,n-1,33}}}\vec{p}^2_{i,n-1,1} + C_{I^*_{\vec{p}_{i,n-1,1}}}\vec{p}^2_{i,n-1,3} -\\
&\quad C_{I^*_{\vec{p}_{i,n-1,13}}}\vec{p}_{i,n-1,1}\vec{p}_{i,n-1,3}\\
C^*_{\vec{p}_i,n-1,23} &= C_{I^*_{\vec{p}_{i,n-1,31}}}\vec{p}_{i,n-1,1}\vec{p}_{i,n-1,2} - C_{I^*_{\vec{p}_{i,n-1,32}}}\vec{p}^2_{i,n-1,1} + C_{I^*_{\vec{p}_{i,n-1,11}}}\vec{p}_{i,n-1,2}\vec{p}_{i,n-1,3} +\\
&\quad C_{I^*_{\vec{p}_{i,n-1,12}}}\vec{p}_{i,n-1,1}\vec{p}_{i,n-1,3}\\
C^*_{\vec{p}_i,n-1,31} &= C_{I^*_{\vec{p}_{i,n-1,12}}}\vec{p}_{i,n-1,2}\vec{p}_{i,n-1,3} - C_{I^*_{\vec{p}_{i,n-1,13}}}\vec{p}^2_{i,n-1,2} + C_{I^*_{\vec{p}_{i,n-1,22}}}\vec{p}_{i,n-1,1}\vec{p}_{i,n-1,3} +\\
&\quad C_{I^*_{\vec{p}_{i,n-1,23}}}\vec{p}_{i,n-1,2}\vec{p}_{i,n-1,1}\\
C^*_{\vec{p}_i,n-1,32} &= -C_{I^*_{\vec{p}_{i,n-1,11}}}\vec{p}_{i,n-1,2}\vec{p}_{i,n-1,3} + C_{I^*_{\vec{p}_{i,n-1,13}}}\vec{p}_{i,n-1,1}\vec{p}_{i,n-1,3} + C_{I^*_{\vec{p}_{i,n-1,21}}}\vec{p}_{i,n-1,3}\vec{p}_{i,n-1,1} -\\
&\quad C_{I^*_{\vec{p}_{i,n-1,23}}}\vec{p}^2_{i,n-1,1}\\
C^*_{\vec{p}_i,n-1,33} &= C_{I^*_{\vec{p}_{i,n-1,11}}}\vec{p}_{i,n-1,2}\vec{p}_{i,n-1,3} - C_{I^*_{\vec{p}_{i,n-1,12}}}\vec{p}_{i,n-1,1}\vec{p}_{i,n-1,2} - C_{I^*_{\vec{p}_{i,n-1,21}}}\vec{p}_{i,n-1,2}\vec{p}_{i,n-1,1} +\\
&\quad C_{I^*_{\vec{p}_{i,n-1,22}}}\vec{p}^2_{i,n-1,1}
\end{aligned}
\tag{A.22}
$$

where $\bar{\bar{C}}^*_{\vec{p}_i,n-1}$ is a function of $\left(\bar{\bar{I}}^*_{i,n-1} + \frac{1}{\Delta t^*}\bar{\bar{I}}^*_{i,n-1} + \bar{\bar{C}}^{V*}_{i,n-1} + \bar{\bar{C}}^{I*}_{i,n-1}\right)^{-1}$ and the orientation $\vec{p}_{i,n-1}$.

After computing the dimensionless velocities and rescaling them to their original dimensional form, new segment positions and orientations can be calculated:

$$\vec{r}_{i,n-1} = \vec{r}_{i,n-1} + \Delta t \, \dot{\vec{r}}_{i,n} \tag{A.23}$$

$$\vec{p}_{i,n-1} = \vec{p}_{i,n-1} + \Delta t \left(\dot{\vec{\omega}}_{i,n} \times \vec{p}_{i,n-1} \right) \tag{A.24}$$

To prevent the accumulation of errors, a necessary step should be taken involving the adjustment of the segment positions at each time step. The central fiber segment remains fixed in space, while all other segments are translated to ensure the preservation of the original fiber length.

A.2 Rigid fiber model

A.2.1 Fiber Equations of Motion

The linear and angular motion equations are established with respect to the center of mass of the fiber, denoted as $\vec{r}_G = \frac{1}{N_{seg}} \sum_{i=1}^{N_{seg}} \vec{r}_i$. Hydrodynamic effects are aggregated across the individual segments of the fiber. The linear and angular momentum equations are as follows:

$$m\ddot{\vec{r}}_G = \sum_{i=1}^{N_{Seg}} \vec{F}_i^h \tag{A.25}$$

$$\frac{\partial}{\partial t} \left(\bar{\bar{I}}_G \cdot \vec{\omega} \right) = \bar{\bar{I}}_G \cdot \dot{\vec{\omega}} + \vec{\omega} \times \left(\bar{\bar{I}}_G \cdot \vec{\omega} \right) = \sum_{i=1}^{N_{seg}} \vec{T}_i^h + \sum_{i=1}^{N_{seg}} \left(\vec{r}_i - \vec{r}_G \right) \times \vec{F}_i^h. \tag{A.26}$$

Here $m = \sum_{i=1}^{n} m_i$ is the fiber mass, and $\bar{\bar{I}}_G$ is the inertia tensor of the fiber with respect to its center of mass, $\vec{F}_i^h$ and $\vec{T}_i^h$ are the hydrodynamic drag force and torque exerted by the fluid on segment i, $\vec{\omega}$ represents the angular velocity of the fiber, $\bar{\bar{I}}_G$ stands for the inertia tensor of the fiber in relation to both its center of mass and the inertial reference frame. Assuming a circular cylinder approximation for the fiber segment, the inertia tensor of segment i with respect to $\vec{r}_G$ is given by:

$$\bar{\bar{I}}_i = \frac{1}{8} m_i D_i^2 \vec{p}_i \vec{p}_i^{\mathrm{T}} + \left[\frac{1}{16} m_i D_i^2 + \frac{1}{12} m_i l_i^2 \right] \left(\bar{\bar{\delta}} - \vec{p}_i \vec{p}_i^{\mathrm{T}} \right) \tag{A.27}$$

Here $\bar{\bar{\delta}}$ as the unit tensor. Defining $\vec{r}_{G_i} = (\vec{r}_i - \vec{r}_G)$, the inertia tensor for segment i with respect to the center of mass of the fiber is derived through the application of the parallel axis theorem as follows:

$$\bar{\bar{I}}_{G_i} = \bar{\bar{I}}_i + +m_i \left[\left(\vec{r}_{G_i} \cdot \vec{r}_{G_i} \right) \bar{\bar{\delta}} - \vec{r}_{G_i} \vec{r}_{G_i}^{\mathrm{T}} \right] \tag{A.28}$$

The overall inertia tensor of the entire fiber with respect to its center of mass is expressed as follows:

$$\bar{\bar{I}}_G = \sum_{i=1}^{N_{seg}} \bar{\bar{I}}_{G_i} \tag{A.29}$$

A.2.2 Hydrodynamic forces and torques

The Hydrodynamic forces and torques on each fiber segment are treated in the same way as discussed for the flexible fibers, and are not repeated here for brevity. For a more comprehensive understanding, readers should refer to Section A.1.2.

A.2.3 Discretization of the equations of motion

The linear momentum equation is discretized as:

$$\frac{m}{\Delta t} \left(\vec{r}_{G,n} - \vec{r}_{G,n-1} \right) = \sum_{i=1}^{N_{seg}} \left(\bar{\bar{A}}_{i,n-1}^{V} + \bar{\bar{A}}_{i,n-1}^{I} \right) \cdot \left[\vec{v}_{i,n-1}^{\infty} - \dot{\vec{r}}_{i,n} \right] \tag{A.30}$$

where

$$\vec{r}_{i,n} = \vec{r}_{G,n} + \vec{\omega}_n \times \vec{r}_{G,n-1} \tag{A.31}$$

The time step is denoted by Δt, and subscripts $n-1$ and n denote the previous and current time steps, respectively. Utilizing the current time step results in an implicit treatment that enhances numerical stability. In addition, the angular momentum equation is discretized as:

$$\begin{aligned}
&\bar{\bar{I}}_{G,n-1} \cdot \left[\vec{\omega}_{i,n} - \vec{\omega}_{i,n-1}\Delta t + \vec{\omega}_{i,n} \times \left(\bar{\bar{I}}_{G,n-1} \cdot \vec{\omega}_{i,n-1}\right)\right] \\
&= \sum_{i=1}^{N_{seg}} \left(\bar{\bar{C}}^{V}_{i,n-1} + \bar{\bar{C}}^{I}_{i,n-1}\right) \cdot \left[\vec{\Omega}^{\infty}_{i,n-1} - \dot{\vec{\omega}}_{n}\right] \\
&\quad + \left(\bar{\bar{H}}^{V}_{i,n-1} + \bar{\bar{H}}^{I}_{i,n-1}\right) : \bar{\bar{E}}^{\infty}_{i,n-1} + \\
&\vec{r}_{G_{i,n-1}} \times \left(\bar{\bar{A}}^{V}_{i,n-1} + \bar{\bar{A}}^{I}_{i,n-1}\right) \cdot \left[\vec{v}^{\infty}_{i,n-1} - \dot{\vec{r}}_{i,n}\right]
\end{aligned} \tag{A.32}$$

These equations are resolved to determine the linear and angular velocity of the fiber, $\vec{r}_{G_n}$ and $\vec{\omega}_n$, respectively. The updated positions and orientations of the segments are defined as:

$$\vec{r}_{i,n} = \vec{r}_{i,n-1} + \Delta t\, \dot{\vec{r}}_{i,n} \tag{A.33}$$

$$\vec{p}_{i,n} = \frac{\vec{p}_{i,n-1} + \Delta t \left(\vec{\omega}_{i,n} \times \vec{p}_{i,n-1}\right)}{|\vec{p}_{i,n-1} + \Delta t \left(\vec{\omega}_{i,n} \times \vec{p}_{i,n-1}\right)|} \tag{A.34}$$

At each time step, segment positions are adjusted to prevent the accumulation of numerical errors. This adjustment involves fixing the central fiber segment in place, while translating all other segments to maintain the original length of the fiber. This approach aligns with the method proposed by Lindstr"om and Uesaka (46).

The time step Δt is subject to two specific constraints. One of these constraints pertains to the relaxation time of the fiber-fluid system and is defined as follows:

$$\Delta t \ll \frac{m}{\eta N_{seg} l} \tag{A.35}$$

To account for the rotation of the fiber induced by the strain rate, it is imperative that:

$$\Delta t \ll \frac{1}{\dot{\gamma}} \tag{A.36}$$

In this context, the characteristic strain rate $\dot{\gamma}$ is defined as the maximum absolute eigenvalue of the strain rate tensor $\bar{\bar{E}}^{\infty}_{\vec{r}_G}$.

References

(*1*) Crowson, R., Folkes, M., and Bright, P. (1980). Rheology of short glass fiber-reinforced thermoplastics and its application to injection molding I. Fiber motion and viscosity measurement. *Polymer Engineering & Science 20*, 925–933.

(*2*) Dong, S, Feng, X, Salcudean, M, and Gartshore, I (2003). Concentration of pulp fibers in 3D turbulent channel flow. *International Journal of Multiphase Flow 29*, 1–21.

(*3*) Lundell, F., Söderberg, L. D., and Alfredsson, P. H. (2011). Fluid mechanics of papermaking. *Annual Review of Fluid Mechanics 43*, 195–217.

(*4*) De Lillo, F., Cencini, M., Durham, W. M., Barry, M., Stocker, R., Climent, E., and Boffetta, G. (2014). Turbulent fluid acceleration generates clusters of gyrotactic microorganisms. *Physical review letters 112*, 044502.

(*5*) Gustavsson, K, Jucha, J, Naso, A, Lévêque, E, Pumir, A, and Mehlig, B (2017). Statistical model for the orientation of nonspherical particles settling in turbulence. *Physical review letters 119*, 254501.

(*6*) Ardekani, M. N., Sardina, G., Brandt, L., Karp-Boss, L., Bearon, R., and Variano, E. (2017). Sedimentation of inertia-less prolate spheroids in homogenous isotropic turbulence with application to non-motile phytoplankton. *Journal of Fluid Mechanics 831*, 655–674.

(*7*) Fan, F.-G., and Ahmadi, G. (1995). A sublayer model for wall deposition of ellipsoidal particles in turbulent streams. *Journal of Aerosol Science 26*, 813–840.

(*8*) Jeffery, G. B. (1922). The motion of ellipsoidal particles immersed in a viscous fluid. *Proceedings of the Royal Society of London. Series A, Containing papers of a mathematical and physical character 102*, 161–179.

(*9*) Burgers, J. (1938). Second report on viscosity and plasticity. Prepared by the Committee for the Study of Viscosity of the Academy of Sciences at Amsterdam. *Kon. Ned. Akad. Wet. Verhand 16*, 1–287.

(*10*) Bretherton, F. P. (1962). The motion of rigid particles in a shear flow at low Reynolds number. *Journal of Fluid Mechanics 14*, 284–304.

(*11*) Cox, R. (1971). The motion of long slender bodies in a viscous fluid. Part 2. Shear flow. *Journal of Fluid Mechanics 45*, 625–657.

(*12*) Batchelor, G., and Green, J.-T. (1972). The hydrodynamic interaction of two small freely-moving spheres in a linear flow field. *Journal of Fluid Mechanics 56*, 375–400.

(*13*) Keller, J. B., and Rubinow, S. I. (1976). Slender-body theory for slow viscous flow. *Journal of Fluid Mechanics 75*, 705–714.

(*14*) Johnson, R. E. (1980). An improved slender-body theory for Stokes flow. *Journal of Fluid Mechanics 99*, 411–431.

(*15*) Kunhappan, D. Numerical modeling of long flexible fibers in inertial flows. Ph.D. Thesis, Université Grenoble Alpes, 2018.

(*16*) Ganani, E., and Powell, R. (1985). Suspensions of rodlike particles: Literature review and data correlations. *Journal of composite materials 19*, 194–215.

(*17*) Powell, R. L. (1991). Rheology of suspensions of rodlike particles. *Journal of statistical physics 62*, 1073–1094.

(*18*) Batchelor, G. (1971). The stress generated in a non-dilute suspension of elongated particles by pure straining motion. *Journal of Fluid Mechanics 46*, 813–829.

(*19*) Yamane, Y., Kaneda, Y., and Dio, M. (1994). Numerical simulation of semi-dilute suspensions of rodlike particles in shear flow. *Journal of non-newtonian fluid mechanics 54*, 405–421.

(*20*) Rahnama, M., Koch, D. L., Iso, Y., and Cohen, C. (1993). Hydrodynamic, translational diffusion in fiber suspensions subject to simple shear flow. *Physics of Fluids A: Fluid Dynamics 5*, 849–862.

(*21*) Leal, L., and Hinch, E. (1971). The effect of weak Brownian rotations on particles in shear flow. *Journal of Fluid Mechanics 46*, 685–703.

(*22*) Stover, C. A., Koch, D. L., and Cohen, C. (1992). Observations of fibre orientation in simple shear flow of semi-dilute suspensions. *Journal of Fluid Mechanics 238*, 277–296.

(*23*) Anczurowski, E, and Mason, S. (1967). The kinetics of flowing dispersions: III. Equilibrium orientations of rods and discs (experimental). *Journal of Colloid and Interface Science 23*, 533–546.

(*24*) Forgacs, O., and Mason, S. (1959). Particle motions in sheared suspensions: IX. Spin and deformation of threadlike particles. *Journal of colloid science 14*, 457–472.

(*25*) Bibbo, M. A., Dinh, S. M., and Armstrong, R. C. (1985). Shear flow properties of semiconcentrated fiber suspensions. *Journal of Rheology 29*, 905–929.

(*26*) Bibbó, M. A. Rheology of semiconcentrated fiber suspensions, Ph.D. Thesis, Massachusetts Institute of Technology, 1987.

(*27*) Shaqfeh, E. S., and Fredrickson, G. H. (1990). The hydrodynamic stress in a suspension of rods. *Physics of Fluids A: Fluid Dynamics 2*, 7–24.

(*28*) Pettersson, A. J., Wikström, T., and Rasmuson, A. (2006). Near wall studies of pulp suspension flow using LDA. *The Canadian Journal of Chemical Engineering 84*, 422–430.

(*29*) Melander, O., and Rasmuson, A. (2004). PIV measurements of velocities and concentrations of wood fibres in pneumatic transport. *Experiments in fluids 37*, 293–300.

(*30*) Du Roure, O., Lindner, A., Nazockdast, E. N., and Shelley, M. J. (2019). Dynamics of flexible fibers in viscous flows and fluids. *Annual Review of Fluid Mechanics 51*, 539–572.

(*31*) Lindström, S. B., and Uesaka, T. (2009). A numerical investigation of the rheology of sheared fiber suspensions. *Physics of fluids 21*.

(*32*) Andric, J., *Numerical modeling of air-fiber flows*; Chalmers Tekniska Hogskola (Sweden): 2014.

(*33*) Crowe, C. T., Schwarzkopf, J. D., Sommerfeld, M., and Tsuji, Y., *Multiphase flows with droplets and particles*; CRC press: 2011.

(*34*) Ljus, C, and Almstedt, A. (1999). Eulerian modelling of pulp-fibre transport in airflow two-phase flow modelling and experimentation. *Pisa: Edizioni ETS*.

(*35*) Hämäläinen, J, Lindström, S. B., Hämäläinen, T, and Niskanen, H (2011). Papermaking fibre-suspension flow simulations at multiple scales. *Journal of Engineering Mathematics 71*, 55–79.

(*36*) Olson, J. A., Frigaard, I., Chan, C., and Hämäläinen, J. P. (2004). Modeling a turbulent fibre suspension flowing in a planar contraction: The one-dimensional headbox. *International Journal of Multiphase Flow 30*, 51–66.

(*37*) Krochak, P. J., Olson, J. A., and Martinez, D. M. (2009). Fiber suspension flow in a tapered channel: The effect of flow/fiber coupling. *International journal of multiphase flow 35*, 676–688.

(*38*) Tornberg, A.-K., and Shelley, M. J. (2004). Simulating the dynamics and interactions of flexible fibers in Stokes flows. *Journal of Computational Physics 196*, 8–40.

(*39*) Li, L., Manikantan, H., Saintillan, D., and Spagnolie, S. E. (2013). The sedimentation of flexible filaments. *Journal of Fluid Mechanics 735*, 705–736.

(*40*) Lindner, A., and Shelley, M. (2015). Elastic fibers in flows. *Fluid-Structure Interactions in Low-Reynolds-Number Flows 168*.

(*41*) Svenning, E., Mark, A., Edelvik, F., Glatt, E., Rief, S., Wiegmann, A., Martinsson, L., Lai, R., Fredlund, M., and Nyman, U. (2012). Multiphase simulation of fiber suspension flows using immersed boundary methods. *Nordic Pulp & Paper Research Journal 27*, 184–191.

(*42*) Wu, J., and Aidun, C. K. (2010). A numerical study of the effect of fibre stiffness on the rheology of sheared flexible fibre suspensions. *Journal of fluid mechanics 662*, 123–133.

(*43*) Wu, J., and Aidun, C. K. (2010). A method for direct simulation of flexible fiber suspensions using lattice Boltzmann equation with external boundary force. *International Journal of Multiphase Flow 36*, 202–209.

(*44*) Xu, H. J., and Aidun, C. K. (2005). Characteristics of fiber suspension flow in a rectangular channel. *International journal of multiphase Flow 31*, 318–336.

(*45*) Schmid, C. F., Switzer, L. H., and Klingenberg, D. J. (2000). Simulations of fiber flocculation: Effects of fiber properties and interfiber friction. *Journal of Rheology 44*, 781–809.

(*46*) Lindström, S. B., and Uesaka, T. (2007). Simulation of the motion of flexible fibers in viscous fluid flow. *Physics of fluids 19*.

(*47*) Switzer III, L. H., and Klingenberg, D. J. (2003). Rheology of sheared flexible fiber suspensions via fiber-level simulations. *Journal of Rheology 47*, 759–778.

(*48*) Yamamoto, S., and Matsuoka, T. (1993). A method for dynamic simulation of rigid and flexible fibers in a flow field. *The Journal of chemical physics 98*, 644–650.

(*49*) Forgacs, O., and Mason, S. (1959). Particle motions in sheared suspensions: X. Orbits of flexible threadlike particles. *Journal of Colloid Science 14*, 473–491.

(*50*) Ross, R. F., and Klingenberg, D. J. (1997). Dynamic simulation of flexible fibers composed of linked rigid bodies. *The Journal of chemical physics 106*, 2949–2960.

(*51*) Zhang, C. Modeling of flexible fiber motion and prediction of material properties. Ph.D. Thesis, 2011.

(*52*) Lindström, S. B., and Uesaka, T. (2008). Simulation of semidilute suspensions of non-Brownian fibers in shear flow. *The Journal of chemical physics 128*.

(*53*) Andrić, J, Lindström, S., Sasic, S, and Nilsson, H (2016). Ballistic deflection of fibres in decelerating flow. *International Journal of Multiphase Flow 85*, 57–66.

(*54*) Andrić, J, Lindström, S. B., Sasic, S., and Nilsson, H. (2014). Rheological properties of dilute suspensions of rigid and flexible fibers. *Journal of non-Newtonian fluid mechanics 212*, 36–46.

(*55*) Andric, J. S., Lindström, S. B., Sasic, S. M., and Nilsson, H. In *Thermal Science*, 2017; Vol. 21, S573–S583.

(*56*) Andrić, J., Fredriksson, S. T., Lindström, S. B., Sasic, S., and Nilsson, H. (2013). A study of a flexible fiber model and its behavior in DNS of turbulent channel flow. *Acta Mechanica 224*, 2359–2374.

(*57*) Wandersman, E., Quennouz, N., Fermigier, M., Lindner, A., and Du Roure, O (2010). Buckled in translation. *Soft matter 6*, 5715–5719.

(*58*) Martínez, M., Vernet, A., and Pallares, J. (2020). Collisions and caustics frequencies of long flexible fibers in two-dimensional flow fields. *Acta Mechanica 231*, 2979–2987.

(*59*) Dotto, D., and Marchioli, C. (2019). Orientation, distribution, and deformation of inertial flexible fibers in turbulent channel flow. *Acta Mechanica 230*, 597–621.

(*60*) Sulaiman, M., Climent, E., Delmotte, B., Fede, P., Plouraboué, F., and Verhille, G. (2019). Numerical modelling of long flexible fibers in homogeneous isotropic turbulence. *The European Physical Journal E 42*, 1–11.

(*61*) Nazockdast, E., Rahimian, A., Needleman, D., and Shelley, M. (2017). Cytoplasmic flows as signatures for the mechanics of mitotic positioning. *Molecular biology of the cell 28*, 3261–3270.

(*62*) Lauga, E., and Powers, T. R. (2009). The hydrodynamics of swimming microorganisms. *Reports on Progress in Physics 72*, 096601.

(*63*) Quennouz, N, Shelley, M., Du Roure, O, and Lindner, A (2015). Transport and buckling dynamics of an elastic fibre in a viscous cellular flow. *Journal of Fluid Mechanics 769*, 387–402.

(*64*) Jack, D. A., and Smith, D. E. (2008). Elastic properties of short-fiber polymer composites, derivation and demonstration of analytical forms for expectation and variance from orientation tensors. *Journal of Composite Materials 42*, 277–308.

(*65*) Martinez, M., Vernet, A., and Pallares, J. (2017). Clustering of long flexible fibers in two-dimensional flow fields for different Stokes numbers. *International Journal of Heat and Mass Transfer 111*, 532–539.

(*66*) Harasim, M., Wunderlich, B., Peleg, O., Kröger, M., and Bausch, A. R. (2013). Direct observation of the dynamics of semiflexible polymers in shear flow. *Physical review letters 110*, 108302.

(*67*) Kantsler, V., and Goldstein, R. E. (2012). Fluctuations, dynamics, and the stretch-coil transition of single actin filaments in extensional flows. *Physical review letters 108*, 038103.

(*68*) Liu, Y., Chakrabarti, B., Saintillan, D., Lindner, A., and Du Roure, O. (2018). Morphological transitions of elastic filaments in shear flow. *Proceedings of the National Academy of Sciences 115*, 9438–9443.

(*69*) Peskin, C. S., and McQueen, D. M. (1989). A three-dimensional computational method for blood flow in the heart I. Immersed elastic fibers in a viscous incompressible fluid. *Journal of Computational Physics 81*, 372–405.

(*70*) Stockie, J. M., and Green, S. I. (1998). Simulating the motion of flexible pulp fibres using the immersed boundary method. *Journal of Computational Physics 147*, 147–165.

(*71*) Kunhappan, D., Harthong, B., Chareyre, B., Balarac, G., and Dumont, P. J. (2017). Numerical modeling of high aspect ratio flexible fibers in inertial flows. *Physics of Fluids 29*, 093302.

(*72*) Witten, T. A., and Diamant, H. (2020). A review of shaped colloidal particles in fluids: anisotropy and chirality. *Reports on Progress in Physics 83*, 116601.

(*73*) Manikantan, H., and Saintillan, D. (2015). Buckling transition of a semiflexible filament in extensional flow. *Physical Review E 92*, 041002.

(*74*) Nguyen, H., and Fauci, L. (2014). Hydrodynamics of diatom chains and semiflexible fibres. *Journal of The Royal Society Interface 11*, 20140314.

(*75*) Słowicka, A. M., Wajnryb, E., and Ekiel-Jeżewska, M. L. (2015). Dynamics of flexible fibers in shear flow. *The Journal of chemical physics 143*, 124904.

(*76*) LaGrone, J., Cortez, R., Yan, W., and Fauci, L. (2019). Complex dynamics of long, flexible fibers in shear. *Journal of Non-Newtonian Fluid Mechanics 269*, 73–81.

(*77*) Kuei, S., Słowicka, A. M., Ekiel-Jeżewska, M. L., Wajnryb, E., and Stone, H. A. (2015). Dynamics and topology of a flexible chain: knots in steady shear flow. *New Journal of Physics 17*, 053009.

(*78*) Kondora, G., and Asendrych, D. (2013). Modelling the dynamics of flexible and rigid fibres. *Chemical and Process Engineering*, 87–100.

(*79*) Chakrabarti, B., Liu, Y., LaGrone, J., Cortez, R., Fauci, L., Du Roure, O., Saintillan, D., and Lindner, A. (2020). Flexible filaments buckle into helicoidal shapes in strong compressional flows. *Nature Physics 16*, 689–694.

(*80*) Voth, G. A., and Soldati, A. (2017). Anisotropic particles in turbulence. *Annual Review of Fluid Mechanics 49*, 249–276.

(*81*) Marchioli, C., and Soldati, A. (2013). Rotation statistics of fibers in wall shear turbulence. *Acta Mechanica 224*, 2311–2329.

(*82*) Zhao, L., and Andersson, H. I. (2016). Why spheroids orient preferentially in near-wall turbulence. *Journal of Fluid Mechanics 807*, 221–234.

(*83*) Zhao, L., Challabotla, N. R., Andersson, H. I., and Variano, E. A. (2019). Mapping spheroid rotation modes in turbulent channel flow: effects of shear, turbulence and particle inertia. *Journal of Fluid Mechanics 876*, 19–54.

(*84*) Ni, R., Ouellette, N. T., and Voth, G. A. (2014). Alignment of vorticity and rods with Lagrangian fluid stretching in turbulence. *Journal of Fluid Mechanics 743*.

(*85*) Marchioli, C., Fantoni, M., and Soldati, A. (2010). Orientation, distribution, and deposition of elongated, inertial fibers in turbulent channel flow. *Physics of fluids 22*, 033301.

(*86*) Dotto, D, Soldati, A, and Marchioli, C (2020). Deformation of flexible fibers in turbulent channel flow. *Meccanica 55*, 343–356.

(*87*) Brouzet, C., Verhille, G., and Le Gal, P. (2014). Flexible fiber in a turbulent flow: A macroscopic polymer. *Physical review letters 112*, 074501.

(*88*) Gay, A, Favier, B, and Verhille, G (2018). Characterisation of flexible fibre deformations in turbulence. *EPL (Europhysics Letters) 123*, 24001.

(*89*) Niskanen, H, Eloranta, H., Tuomela, J, and Hämäläinen, J (2011). On the orientation probability distribution of flexible fibres in a contracting channel flow. *International Journal of Multiphase Flow 37*, 336–345.

(*90*) Rosti, M. E., Banaei, A. A., Brandt, L., and Mazzino, A. (2018). Flexible fiber reveals the two-point statistical properties of turbulence. *Physical review letters 121*, 044501.

(*91*) Rosti, M. E., Olivieri, S., Banaei, A. A., Brandt, L., and Mazzino, A. (2020). Flowing fibers as a proxy of turbulence statistics. *Meccanica 55*, 357–370.

(*92*) Manikantan, H., and Saintillan, D. (2013). Subdiffusive transport of fluctuating elastic filaments in cellular flows. *Physics of Fluids 25*, 073603.

(*93*) Hess, H., Clemmens, J., Brunner, C., Doot, R., Luna, S., Ernst, K.-H., and Vogel, V. (2005). Molecular self-assembly of "nanowires" and "nanospools" using active transport. *Nano letters 5*, 629–633.

(*94*) Van den Heuvel, M. G., De Graaff, M. P., and Dekker, C. (2006). Molecular sorting by electrical steering of microtubules in kinesin-coated channels. *Science 312*, 910–914.

(*95*) Yokokawa, R., Takeuchi, S., Kon, T., Nishiura, M., Sutoh, K., and Fujita, H. (2004). Unidirectional transport of kinesin-coated beads on microtubules oriented in a microfluidic device. *Nano Letters 4*, 2265–2270.

(*96*) Bouzarth, E. L., Layton, A. T., and Young, Y.-N. (2011). Modeling a semiflexible filament in cellular Stokes flow using regularized Stokeslets. *International Journal for Numerical Methods in Biomedical Engineering 27*, 2021–2034.

(*97*) Kim, S, and Karilla, S. (1991). Microhydrodynamics: Principles and Selected Applications. Butterworth-Heinemann.

(*98*) Herrera, B., and Pallares, J. (2013). Identification of vortex cores of three-dimensional large-vortical structures. *Archive of Applied Mechanics 83*, 1383–1391.

(*99*) Salinas, A, and Pittman, J. (1981). Bending and breaking fibers in sheared suspensions. *Polymer Engineering & Science 21*, 23–31.

(*100*) Sherwood, S. C., Phillips, V. T., and Wettlaufer, J. (2006). Small ice crystals and the climatology of lightning. *Geophysical Research Letters 33*.

(*101*) Saintillan, D., and Shelley, M. J. (2007). Orientational order and instabilities in suspensions of self-locomoting rods. *Physical review letters 99*, 058102.

(*102*) Locsei, J., and Pedley, T. (2009). Run and tumble chemotaxis in a shear flow: the effect of temporal comparisons, persistence, rotational diffusion, and cell shape. *Bulletin of mathematical biology 71*, 1089–1116.

(*103*) Parsa, S., Calzavarini, E., Toschi, F., and Voth, G. A. (2012). Rotation rate of rods in turbulent fluid flow. *Physical review letters 109*, 134501.

(*104*) Norouzi, M., Andric, J., Vernet, A., and Pallares, J. (2022). Shape evolution of long flexible fibers in viscous flows. *Acta Mechanica 233*, 2077–2091.

(*105*) Toschi, F., and Bodenschatz, E. (2009). Lagrangian properties of particles in turbulence. *Annual review of fluid mechanics 41*, 375–404.

(*106*) Hinch, E., and Leal, L. (1979). Rotation of small non-axisymmetric particles in a simple shear flow. *Journal of Fluid Mechanics 92*, 591–607.

(*107*) Lovecchio, S., Zonta, F., Marchioli, C., and Soldati, A. (2017). Thermal stratification hinders gyrotactic micro-organism rising in free-surface turbulence. *Physics of Fluids 29*.

(*108*) Lovecchio, S., Marchioli, C., and Soldati, A. (2013). Time persistence of floating-particle clusters in free-surface turbulence. *Physical Review E 88*, 033003.

(*109*) Zhao, L., Marchioli, C., and Andersson, H. I. (2014). Slip velocity of rigid fibers in turbulent channel flow. *Physics of Fluids 26*.

(*110*) Challabotla, N. R., Zhao, L., and Andersson, H. I. (2015). Orientation and rotation of inertial disk particles in wall turbulence. *Journal of Fluid Mechanics 766*, R2.

(*111*) Zhao, L, Gustavsson, K, Ni, R, Kramel, S, Voth, G., Andersson, H., and Mehlig, B (2019). Passive directors in turbulence. *Physical Review Fluids 4*, 054602.

(*112*) Zhao, F, George, W., and van Wachem, B. G. (2015). Four-way coupled simulations of small particles in turbulent channel flow: The effects of particle shape and Stokes number. *Physics of Fluids 27*.

(*113*) Lopez, D., and Guazzelli, E. (2017). Inertial effects on fibers settling in a vortical flow. *Physical Review Fluids 2*, 024306.

(*114*) Zhao, L., and Andersson, H. I. (2020). Why spheroids orient preferentially in near-wall turbulence–CORRIGENDUM. *Journal of Fluid Mechanics 887*, E1.

(*115*) Ardekani, M. N., and Brandt, L. (2019). Turbulence modulation in channel flow of finite-size spheroidal particles. *Journal of Fluid Mechanics 859*, 887–901.

(*116*) Njobuenwu, D. O., and Fairweather, M. (2016). Simulation of inertial fibre orientation in turbulent flow. *Physics of Fluids 28*.

(*117*) Kerekes, R. J., and Schell, C. J. (1995). Effects of fiber length and coarseness on pulp flocculation. *Tappi journal.–(USA)*.

(*118*) Meyer, C. R., Byron, M. L., and Variano, E. A. (2013). Rotational diffusion of particles in turbulence. *Limnology and Oceanography: Fluids and Environments 3*, 89–102.

(*119*) Koch, D. L., and Shaqfeh, E. S. (1989). The instability of a dispersion of sedimenting spheroids. *Journal of Fluid Mechanics 209*, 521–542.

(*120*) Jafari, A., Zamankhan, P., Mousavi, S. M., and Henttinen, K. (2006). Multiscale modeling of fluid turbulence and flocculation in fiber suspensions. *Journal of applied physics 100*.

(*121*) Kajishima, T., and Nomachi, T. (2006). One-equation subgrid scale model using dynamic procedure for the energy production.

(*122*) Yoshizawa, A., and Horiuti, K. (1985). A statistically-derived subgrid-scale kinetic energy model for the large-eddy simulation of turbulent flows. *Journal of the Physical Society of Japan 54*, 2834–2839.

(*123*) Horiuti, K. (1985). Large eddy simulation of turbulent channel flow by one-equation modeling. *Journal of the Physical Society of Japan 54*, 2855–2865.

(*124*) Okamoto, M., and Shima, N. (1999). Investigation for the One-Eaquation-Type Subgrid Model with Eddy-Viscosity Expression Including the Shear-Damping Effect. *JSME International Journal Series B Fluids and Thermal Engineering 42*, 154–161.

(*125*) Lilly, D. K. (1992). A proposed modification of the Germano subgrid-scale closure method. *Physics of Fluids A: Fluid Dynamics 4*, 633–635.

(*126*) Tang, H., Lei, Y., Li, X., and Fu, Y. (2019). Large-eddy simulation of an asymmetric plane diffuser: Comparison of different subgrid scale models. *Symmetry 11*, 1337.

(*127*) Germano, M., Piomelli, U., Moin, P., and Cabot, W. H. (1991). A dynamic subgrid-scale eddy viscosity model. *Physics of Fluids A: Fluid Dynamics 3*, 1760–1765.

(*128*) Kim, S., and Karrila, S. J., *Microhydrodynamics: principles and selected applications*; Courier Corporation: 2013.

(*129*) Vega, C., and Lago, S. (1994). A fast algorithm to evaluate the shortest distance between rods. *Computers & chemistry 18*, 55–59.

(*130*) Obi, S., Aoki, K, and Masuda, S In *Ninth symposium on turbulent shear flows*, 1993; Vol. 305, pp 305–312.

(*131*) Buice, C. U., and Eaton, J. K. (2000). Experimental Investigation of Flow Through an Asymmetric Plane Diffuser: (Data Bank Contribution)1. *Journal of Fluids Engineering 122*, 433–435.

(*132*) Weller, H. G., Tabor, G., Jasak, H., and Fureby, C. (1998). A tensorial approach to computational continuum mechanics using object-oriented techniques. *Computers in physics 12*, 620–631.

(*133*) Jasak, H. (1996). Error analysis and estimation for the finite volume method with applications to fluid flows.

(*134*) Greenshields, C., *OpenFOAM v11 User Guide*; The OpenFOAM Foundation: London, UK, 2023.

(*135*) Kaltenbach, H.-J., Fatica, M, Mittal, R, Lund, T., and Moin, P (1999). Study of flow in a planar asymmetric diffuser using large-eddy simulation. *Journal of Fluid Mechanics 390*, 151–185.

(*136*) Tritton, D. Physical fluid dynamics, 2nd edn. Clarendon, 1988.